Gain Flattening Coatings for Improved Performance of Asymmetric Multiple Quantum Well Laser

GAIN FLATTENING COATINGS FOR IMPROVED PERFORMANCE OFASYMMETRIC MULTIPLE QUANTUM WELL LASER

By

XIAONAN TAN, M.A.Sc.

A Thesis

Submitted to the Department of Engineering Physics

and the School of Graduate Studies

in Partial Fulfillment of the Requirements

for the Degree

Doctor of Philosophy.

McMaster University

DOCTOR OF PHILOSOPHY (2009) McMaster University

(Engineering Physics) Hamilton, Ontario

TITLE: Gain Flattening Coatings for Improved Performance of Asymmetric Multiple Quantum Well Laser

AUTHOR: Xiaonan Tan

M.A.Sc., McMaster University, Canada

SUPERVISOR: Peter Mascher, Professor

CO-SUPERVISOR: Daniel T. Cassidy, Professor

NUMBER OF PAGES: xiv, 122

Dedications

To my parents,

my wife

Abstract

Compositionally asymmetric multiple quantum well (AMQW) lasers are used for the demonstration of the gain flattening coating functionality. The gain spectra of the lasers are extracted using a non-linear least square fitting method. An optimum facet reflectance spectrum is calculated for a chosen current. For manufacturability, a modified reflectance spectrum of the gain flattening coating is proposed, in order to achieve operation over a wider spectral range without the 'difficult' gap which was a region where lasing was difficult or impossible to achieve due to insufficient gains at these wavelengths.

Silicon oxides films with high, medium, and low refractive indices fabricated in an inductively coupled plasma (ICP) enhanced chemical vapor deposition (CVD) system are chosen as the building blocks of the gain flattening coating. An 18-layer coating is designed by the insertion of needle-like refractive index variation with a few optimization methods applied to minimize the merit function. A laser bar holder is custom designed and fabricated. Experiments and modification on the laser bar holder are carried out for better performance. The 18-layer gain flattening coating is then fabricated in the ICP-CVD system with an in-situ spectroscopic ellipsometric measurement. It is observed that the non-lasing gap has disappeared after the coating is applied. Without external feedback, the coated laser shows tuning over 85 nm with the central wavelength of 1593 nm, while

the uncoated laser has a non-lasing gap of about 25 nm in the central region of the tuning range of 70 nm.

Finally, the coherence length of a low coherent source synthesized from the gain flattening coated AMQW laser is measured by using Michelson interferometer. The highest depth resolution that can be achieved is measured as 40 μm. The power intensity of the synthesized low coherence light source from the gain flattening coated AMQW laser is rendered from the interferogram using fast Fourier transform (FFT).

Acknowledgements

I am deeply indebted to my supervisor Prof. Peter Mascher and co-supervisor Prof. Daniel Cassidy for the encouragement and valuable guidance. I would like to thank Dr. Jacek Wojcik and Mr. Haiqiang Zhang for maintaining the perfect condition of the CVD system which allowed us to perform numerous experiments. I really appreciate that Dr. Jingcong Wang helped on setting up the optical coherence length measurement. I would also like to give thanks to all my colleagues and staff members who have contributed greatly to provide a supportive and exciting research atmosphere.

This work was supported by the Ontario Research and Development Challenge Fund (ORDCF) under the auspices of the Ontario Photonics Consortium (OPC), as well as the Centres for Photonics and Materials and Manufacturing of Ontario Centres of Excellence (OCE) Inc.

I am very grateful to my wife for her patient love and support, which enables me to complete this work. Last but not least, I would like to thank my parents, who have been supporting me going through all the rough times in my life.

Contents

List of Figures

List of Tables

Chapter 1

Introduction

In 1962, coherent light emission from a semiconductor diode was first demonstrated at liquid nitrogen temperature by Robert Hall and his team at the General Electric research center [1]. In 1970, Zhores Alferov et al. [2] from the Ioffe Institute in the former Soviet Union and Izuo Hayashi et al. [3] of Bell Telephone Laboratories independently developed laser diodes continuously operating at room temperature using heterojunction structures. Since then, diode lasers have been intensely studied and developed for research and commercial purposes. Various material systems, modified structures, and specifically designed configurations have allowed diode lasers to be specialized for different properties such as high output power, high modulation speed, narrow spectral linewidth, or full operating wavelengths, and therefore a large number of applications are seen.

Among all the efforts to optimize diode lasers, scientists have been treating the facets of diode lasers with coatings, especially dielectric interference coatings, to improve performance.

Gradual long-term degradation during continuous wave (CW) operation is known to occur in double-heterojunction (DH) lasers. It has been shown that long-term

degradation is associated with facet erosion whose progress rate is a function of output power density. Facet passivation with dielectric films is effective in reducing the long-term degradation of diode lasers and providing long-lived lasers [4-7].

For most III-V compounds, the natural reflectance due to the refractive index discontinuity at the semiconductor-air interface is 25-35%. The application of a high reflection (HR) coating to one of the facets of a diode laser lowers the lasing threshold current and increases the external differential quantum efficiency and output power of lasers [8-10]. The conventional approach for HR facet coating is to deposit a dielectric layer followed by a highly reflecting metal layer (Al or Au) onto the non-emitting facet. The dielectric layer prevents the metal from shorting the *p-n* junction. However, there are problems associated with the metal layer including dissolution during the solder mounting and shorting due to pinholes in the dielectric layer. A stack of dielectric films deposited on the facet can have a reflection coefficient significantly better than that of metals, prevent shorting due to the nature of dielectric materials, and be impervious to the common solder fluxes as well as any acids that may be used during cleaning.

Anti-reflection (AR) coated semiconductor lasers are of great interest for applications such as external cavity lasers and optical amplifiers. In both cases it is desirable to reduce the modal reflectance as much as possible. In the former case an antireflection coating is used to further increase the relative feedback strength, and lasers with very strong external feedback can operate stably in these extended cavities, with concomitantly narrowed linewidths [11]. In the latter case the low reflectance is desired to achieve a higher saturated gain with a low gain ripple due to cavity effects, as well as low

levels of the amplified reflection [12-13]. Conventional AR coatings are based upon a single-layer quarter-wavelength film with a refractive index equal to the square root of that of the substrate. For the refractive index of the semiconductor laser facet, it is not always easy to find a manufacturable material with the exact refractive index. Although a facet reflectivity of 10^{-4} or less can be reproducibly obtained using a single layer of silicon nitride film for InGaAsP lasers [14] or a layer of silicon oxide film with controlled oxygen content [15], the use of multilayer coatings is inevitable because the bandwidth of the single-layer system is inherently too narrow. Various multilayer AR coatings have been reported: double-layer coatings [16-18], triple-layer coatings [19-20] and stepwise-graded-index multilayer coatings using Herpin's principle [21].

There was an attempt to optimize output of an external cavity laser by depositing a stack of thin films onto one of the laser facets based on the calculated gain spectrum [22]. In the paper, the authors set the external cavity laser (ECL) in the so called Littrow configuration, where an AR coating is deposited onto one of the laser facets allowing the light to be coupled into an external resonator, which contains an angle-tuned grating. The grating provides frequency-selective optical feedback to the diode laser via its AR-coated output facet, which allows the laser to achieve narrow linewidth and tunability. It is known that at both ends of the tuning curve, the gain cannot compensate for the cavity losses and the laser will stop oscillating. Application of a higher reflectivity at the ends of the tuning curve would reduce the cavity losses so that the laser could still oscillate at these wavelengths, and therefore, the tuning range could be increased. For maximum output power performance and widest tuning range, a wavelength dependent output

coupler is required which has low reflectivity at the center of the tuning curve and increasing reflectivity toward the edges. The optimum output coupler reflectivity displayed in Figure 1.1 was calculated from the laser gain spectrum using the method [23] which was initially used to optimize the output power from various types of single-wavelength lasers, such as gas lasers. The authors [22] extended the optimum output-coupler reflectivity concept to tunable lasers.

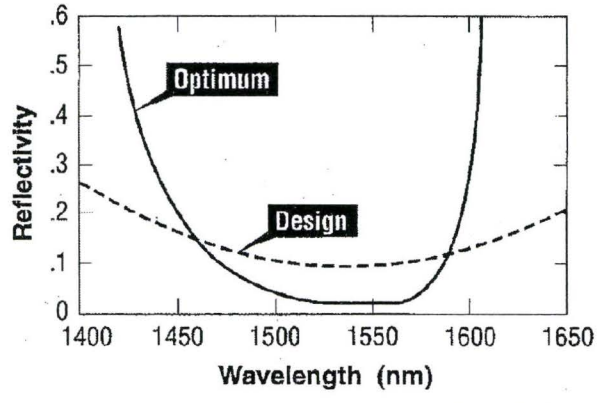

Figure 1.1 Calculated optimal reflectivity versus wavelength for a diode laser gain medium. A three-layer Fabry-Perot stack mirror design is used. This design matches the calculated target reasonably well over a wide wavelength range near the center, but exhibits reflectivities far too low at the edges of the tuning curve. [22]

A three-layer coating was designed to roughly match the optimum reflectivity, displayed in Figure 1.1. Even though the designed reflectivity (the obtained reflectivity was not given by the paper) is off from the target by roughly 10 percentage points, the external cavity laser showed simultaneous improvement in output power and tuning range. This paper happens to be the only publication found in the literature as to custom design and fabrication of a coating from a calculated gain spectrum of a semiconductor laser to improve the performance of a laser diode.

The present thesis project was initiated by the idea of coating laser facets for better performance of tunability. Asymmetric multiple quantum well (AMQW) lasers designed by Dr. Cassidy's team at McMaster University display a rather flat gain spectrum at a certain current, however, there can be a region in the middle of the tuning range where lasing is difficult or impossible to achieve due to insufficient gains at these wavelengths. The goal was to coat the laser facet to achieve operation over a wider spectral range without the 'difficult' gap. This kind of coating is termed a gain flattening coating since its function is to flatten the gain over the entire lasing range.

Many applications of diode lasers would benefit from these improvements. Laser spectroscopy, coherent optical communications, sensing, and precision measurements are the major applications where the tuning range of the diode laser is the most crucial parameter, and as always: the wider the tuning range, the better. Also, in an optical coherence tomography (OCT) system, a wavelength-scanning laser source is required and the depth resolution is controlled by the scanning range [24-25]. Especially in synthesized OCT (SOCT), by rapidly tuning the laser wavelength over a broad spectral region and by appropriate averaging, the time-averaged optical coherence function determines the depth resolution in an imaging system [25-26]. As one of the approaches of achieving tunable lasers, external cavities offer the ability to tune the wavelength of emission of diode lasers over a broad range with a collimating lens and grating [27], or a diffractive optical element (DOE) [28]. Compared to OCT using super-luminescent diodes (SLD) as a source, the SOCT approach has the advantage of a controlled depth resolution, higher power in a

small spectral interval and higher brightness, which enables an easier coupling to an optical fiber.

In this work, asymmetric multiple quantum well lasers were used for the demonstration of the coating functionality. First, the gain spectra were calculated from high resolution power spectra of the laser diodes using a non-linear least square fitting method. Secondly, a method to achieve the desired facet reflectance to ensure tuning over an extended range was developed, and then, multi-layer coatings to achieve the desired facet reflection were designed, using the insertion of a needle-like refractive index variation layer with a few optimization cycles applied to minimize the merit function. The coating materials were silicon oxides with various refractive indices fabricated in an inductively coupled plasma (ICP) enhanced chemical vapor deposition (CVD) system.

In order to implement the deposition of coatings onto the tiny laser facets, a laser bar holder was designed, which could accommodate up to three laser bars and a witness sample for the in-situ spectroscopic ellipsometry monitoring. During the experiment, it was found that the height of the screws which fix the clamping metal piece holding the laser bar had a substantial impact on the thickness uniformity of the layer deposited on the laser bar and there was a linear correlation between the thickness of the film grown on the bar and the witness sample. The laser bar holder was optimized and calibrated before application.

Gain flattening coatings were deposited onto laser facets. During the deposition, the in-situ spectroscopic ellipsometer was used to monitor the growing layer, with the refractive index and thickness of the film fitted from time to time and compared to the

design, while online re-optimization of the rest of the layers was used to decrease the possibility of manufacture failure.

After the deposition, the power spectrum of the coated laser was compared to that of an uncoated laser. It was observed that the non-lasing gap had disappeared after the gain flattening coating was applied. Without external feedback, the coated laser showed tuning over 85 nm with the central wavelength of 1593 nm, while the uncoated laser had a non-lasing gap of about 25 nm in the central region of the tuning range of 70 nm. The reflectance-gain (*RG*) product curve of the coated laser showed that as the current was increased little by little, the flat top of the *RG* curve shifted continuously from the longer wavelength to the shorter wavelength, meaning continuous tunability over the entire range. The reflectance of the coated facet was calculated and compared to the designed reflectance.

Finally, the depth resolution for SOCT using the gain flattening coated AMQW laser was measured by using a Michelson interferometer. The coherence length of 40 μm was obtained when the current applied to the laser was modulated with a triangle waveform at a frequency of 100 kHz between 100 mA and 300 mA. Therefore the highest depth resolution that could be achieved with this gain flattened laser was 40 μm. The power spectral intensity of the synthesized low coherence light source from the gain flattening coated AMQW laser was rendered from the interferogram using fast Fourier transform (FFT).

Following this Introduction of Chapter 1, the thesis is divided into five chapters. In Chapter 2, a brief description of the uncoated asymmetric multiple quantum well laser

is given, including structure, power spectrum, and gain spectrum. A non-linear least square fitting method to extract the *RG* product is explained in some detail. The facet reflectance for the laser is calculated from the extracted *RG* product and modified for better performance. Synthesis of a coating structure with the needle method and a few optimization methods are discussed in Chapter 3. As well, the design strategy, the criteria for choosing coating materials, and the thickness limitations for manufacturability are also presented. Chapter 4 discusses the fabrication of coatings. The ICP-CVD system and the spectroscopic ellipsometry monitoring are explained. The laser bar holder is optimized and calibrated for the best performance. Also, the deposition of multilayer coatings with in-situ spectroscopic ellipsometry and real time correction are presented. The characterization of a coated laser is given in Chapter 5. The power and gain spectrum with increasing currents are included. The reflectance of the coated facet calculated from the *RG* product is compared to the design and a discussion of the deviation is given. As one of the applications of the gain flattening coated AMQW laser, SOCT technology is summarized. The measurement of the optical coherence length of the laser is presented including analysis of an interferogram. Chapter 6 is a conclusion and suggestions for future work.

Chapter 2

AMQW lasers and gain spectra

2.1 AMQW lasers

Quantum well (QW) lasers were first demonstrated in 1975 [29]. Since then, they have been well studied and developed as light sources for telecommunication, data storage, spectroscopy and other applications. There are single quantum well (SQW) and multiple quantum well (MQW) lasers. Compared to SQW lasers, MQW lasers have larger volumes of the active region to better overlap with the optical mode and therefore, fully utilize the QW advantage of a high gain coefficient, especially for the long wavelength InGaAsP/InP based lasers [30]. Conventional MQW lasers are composed of multiple identical quantum wells. Since the first asymmetric multiple quantum well (AMQW) lasers were demonstrated in 1989 [31], they have been intensely researched and considered promising for broad gain spectra and large tuning ranges [32-34].

AMQW laser structures could be either dimensionally or compositionally asymmetric. Figure 2.1 shows a dimensionally AMQW laser, which has identical quantum well compositions but different thicknesses of the wells. Figure 2.2 shows a compositionally AMQW laser, which has varying compositions of the quantum well

materials but fixed thickness of the wells. Both offer the opportunities of achieving much broader gain spectra than conventional MQW laser, when the structure of the AMQW is carefully designed.

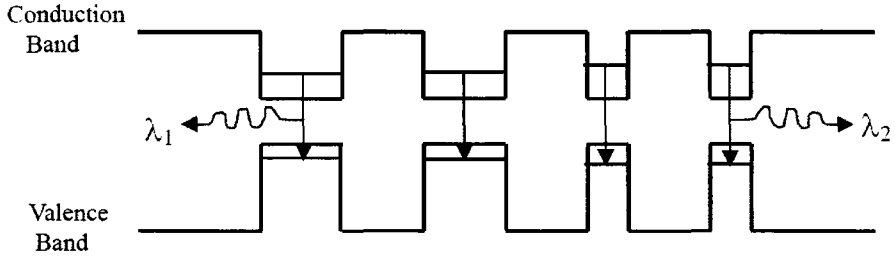

Figure 2.1 Energy band diagram of a dimensionally AMQW laser structure. The quantum well material is identical but the thicknesses are different, and light of λ_1 and λ_2 ($\lambda_2<\lambda_1$) is emitted accordingly.

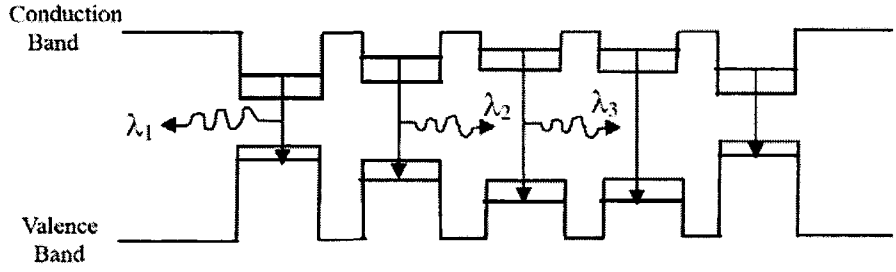

Figure 2.2 Energy band diagram of a compositionally AMQW laser structure. The quantum well materials are different while identical thickness of the wells is maintained, and light of λ_1, λ_2 and λ_3 ($\lambda_3<\lambda_2<\lambda_1$) is emitted accordingly.

Over the years, efforts [33-36] have been put into the theoretical development and experimental practice to achieve broader and broader gain spectra, however, the gain spectra cannot be broadened without limit. They are affected by factors such as the separation of the short and long transition wavelengths, the number of long wavelength wells, the location of the different quantum wells, the barrier thickness and so forth. In this project, we are coating the AMQW lasers according to their gain spectra to flatten

and further broaden them. Compositionally AMQW lasers are used because they have several advantages compared to dimensionally AMQW structures [25]. The optical gain is a function of the magnitude of the overlap of the quantum well with the optical mode. Dimensionally AMQW devices thus have optical gains that vary, owing to the optical confinement factor due to the waveguide profile, with the wavelength of emission of the well. Since the quantum wells in a dimensionally AMQW device that are designed to emit at short wavelengths will be thin, these short wavelength wells will exhibit lower modal gain than the long wavelength wells. Additional short wavelength wells can be added to compensate for the loss of modal gain owing to the confinement factor decrease, but this makes strain balancing more difficult. In addition, any carrier processes that are a function of the thickness of the well, such as carrier capture, will also need to be compensated. Compositionally AMQW structures have wells of the same thickness and thus do not require these compensations.

The material structure of the laser [25] is displayed in Table 2.1. To make a laser device, the laser material structure is etched down 1.5 μm to form a ridge waveguide with widths of 3 to 6 μm. Metal contacts are deposited at the top and bottom for current injection and heat dissipation. The lasers are then cleaved with a cavity length of 950 μm. The power spectra of the lasers are obtained by coupling the laser light from one laser facet to a tapered single-mode fiber which is connected to an ANDO AQ6317B optical spectrum analyzer (OSA). Figure 2.3 shows a typical power spectrum of a laser without any coatings on either facet at various currents.

Layer	Type	Thickness (Å)	Doping (cm^{-3})	Material	x	y
21	Cladding	2000	4.0×10^{19}	p-InP	/	/
20	Cladding	15000	4.0×10^{18}	p-InP	/	/
19	Cladding	2000	4.0×10^{17}	p-InP	/	/
18	Cladding	30	4.0×10^{17}	p-$In_{1-x}Ga_xAs_yP_{1-y}$	0.280	0.610
17	Cladding	1000	4.0×10^{17}	p-InP	/	/
16	SCH*	1500	/	$In_{1-x}Ga_xAs_yP_{1-y}$	0.042	0.092
15	SCH*	700	/	$In_{1-x}Ga_xAs_yP_{1-y}$	0.109	0.238
14	Barrier	218	/	$In_{1-x}Ga_xAs_yP_{1-y}$	0.225	0.305
13	Well	100	/	$In_{1-x}Ga_xAs_yP_{1-y}$	0.225	0.800
12	Barrier	50	/	$In_{1-x}Ga_xAs_yP_{1-y}$	0.225	0.305
11	Well	100	/	$In_{1-x}Ga_xAs_yP_{1-y}$	0.225	0.710
10	Barrier	50	/	$In_{1-x}Ga_xAs_yP_{1-y}$	0.225	0.305
9	Well	100	/	$In_{1-x}Ga_xAs_yP_{1-y}$	0.225	0.690
8	Barrier	50	/	$In_{1-x}Ga_xAs_yP_{1-y}$	0.225	0.305
7	Well	100	/	$In_{1-x}Ga_xAs_yP_{1-y}$	0.225	0.690
6	Barrier	50	/	$In_{1-x}Ga_xAs_yP_{1-y}$	0.225	0.305
5	Well	100	/	$In_{1-x}Ga_xAs_yP_{1-y}$	0.225	0.800
4	Barrier	218	/	$In_{1-x}Ga_xAs_yP_{1-y}$	0.225	0.305
3	SCH*	700	/	$In_{1-x}Ga_xAs_yP_{1-y}$	0.109	0.238
2	SCH*	1500	/	$In_{1-x}Ga_xAs_yP_{1-y}$	0.042	0.092
1	Cladding	7500	1.0×10^{18}	n-InP	/	/
	Substrate	7500	1.0×10^{18}	n-InP	/	/
*SCH - Separate Confinement Heterostructure						

Table 2.1 Material structure of the AMQW laser device.

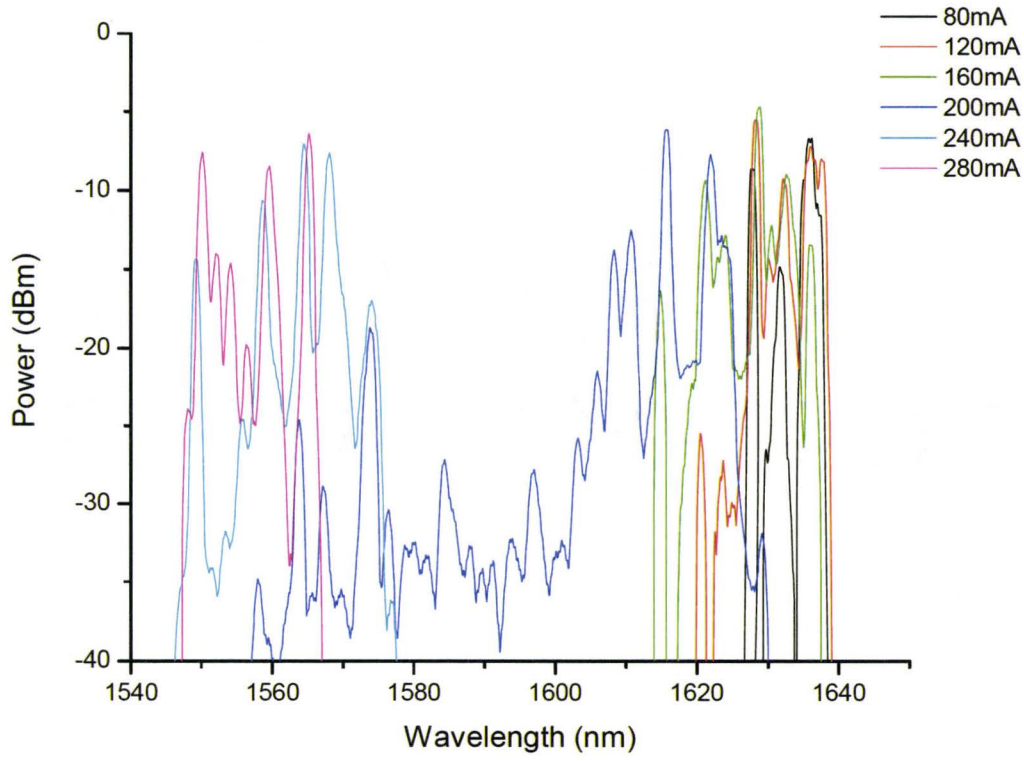

Figure 2.3 Power spectra of an uncoated AMQW laser at various currents at resolution of 0.1 nm.

When the current reaches about 80 mA, the long wavelength wells start lasing since the wells of thinner band gap is easier to be excited than the thicker one. At further increased current, the lasing range becomes a bit wider as the short wavelength wells start to contribute to the total gain. At about 200 mA and beyond, the gain contributed by the short wavelength wells start to exceed that by the long wavelength wells and lasing peaks at the short wavelength appear. As the current is increased even further, the gain at the short wavelength dominates and the long wavelength part is no longer lasing. It is also noticed that at the transition current of 200 mA, the lasing wavelength is not decreasing continuously. There is a non-lasing gap of about 25 nm in the entire wavelength range. In the experiment, smaller increments of the current were applied around 200 mA but the

gap between 1575 and 1600 nm continues to appear, no matter how little the current changes.

2.2 Non-linear fitting of gain spectra

In a laser, "gain" usually refers to the single pass gain. It is an amplification factor and is defined as the ratio of output power and input power [37], if we shine light on one facet and measure the output at the other facet. Such measurement is difficult to achieve since it requires a widely tunable light source, broadband anti-reflection coatings on both facets of the laser and precise estimation of coupling efficiency. Therefore, other indirect methods have been developed over the years to measure the gain.

There exist a few methods that are commonly used: the Hakki-Paoli method [38], the mode sum/min method [39], the Henry method [40], the Fourier transform and the Fourier series expansion methods [41-43], and the nonlinear least-squares fitting method [44] which is used in this work as it is considered to be the least noise-sensitive among the indirect gain measurement techniques, aside from advantages shared with some other methods.

The following gives a brief explanation of the nonlinear fitting method following the work of Wang [44]. Historically, the transmission line matrix formalism describing the transfer properties of microwave networks was found useful to be extended to the electromagnetic fields associated with optical masers. An Airy function which was derived using transmission line formalism was then developed to describe the amplified spontaneous emission power $I(\lambda)$ in a certain wavelength range $d\lambda$ for Fabry-Perot (F-P) semiconductor lasers [45]:

$$I(\lambda)d\lambda = \frac{B(\lambda)d\lambda[1+R(\lambda)G(\lambda)][1-R(\lambda)]}{[1-R(\lambda)G(\lambda)]^2 + 4R(\lambda)G(\lambda)\sin^2\left[\frac{2\pi n(\lambda)L}{\lambda}\right]} \tag{2.1}$$

$$R(\lambda) = \sqrt{R_1(\lambda)R_2(\lambda)} \tag{2.2}$$

where $G(\lambda)$ is the single-pass modal gain; $R_1(\lambda)$ and $R_2(\lambda)$ are the reflectivities of the two laser facets, respectively; L is the laser cavity length; n is the wavelength dependent refractive index of the laser material; and $B(\lambda)d\lambda$ is the total amount of spontaneous emission coupled into a wavelength interval $d\lambda$.

During a measurement, the response function $H(\lambda)$ of the optical spectrum analyzer (OSA) gives a weighted average of the true spectral output of the laser, and thus, the Airy function needs to be convoluted with the instrument response function to simulate the effect of the process of measurement on the spectral output. For each F–P mode of the laser cavity, the parameters that define the Airy function can be expanded around the mode peak and formulated as:

$$I'(\lambda)d\lambda = \frac{C}{(1-RG)^2 + 4RG\sin^2\left[2\pi nL\left(\frac{1}{\lambda}-\frac{1}{\lambda_0}\right)\right]} * H(\lambda) \tag{2.3}$$

$$RG(\lambda) = RG(\lambda_0) + \beta(\lambda-\lambda_0) \tag{2.4}$$

$$C(\lambda) = C(\lambda_0) + \gamma(\lambda-\lambda_0) \tag{2.5}$$

where RG is the product of R and G; λ_0 is the peak wavelength of the individual mode; and $C(\lambda)=B(1+RG)(1-R)d\lambda$ is set as a fitting parameter. Within each mode the RG product and C parameter are linear functions of the wavelength with slopes of β and γ, respectively. The phase refractive index is approximated as a constant in each mode,

since it is a weak function of the wavelength in the wavelength range of interest. To fit for the six parameters, RG, λ_0, n, C, β and γ, the Levenberg-Marquardt method [46] is used as a nonlinear least squares fitting procedure. Results obtained from the Hakki-Paoli method are used as initial values for RG, λ_0, n and C, while β and γ are initiated with values of zero. After every iteration, the prediction of (2.3) is compared to the measured data to test the goodness of fitting through:

$$\chi^2 = \sum_{i=1}^{N} \left[\left(I'(\lambda_i) - Y(\lambda_i) \right) / \sigma_i \right]^2 \tag{2.6}$$

where $Y(\lambda_i)$ is the measured data and σ_i is the weighting factor. When the difference between two consecutive iterations is small enough, e.g., $\frac{\left|\chi_{i+1}^2 - \chi_i^2\right|}{\chi_i^2} < 0.001\%$ in the vicinity of the minimum, the gain parameters are successfully extracted.

As mentioned above, the response function $H(\lambda)$ of the OSA is needed for evaluation of the gain spectra of AMQW lasers and it is dependent on the OSA used (ANDO AQ6317B). A commercial tunable laser source is suitable for the response function measurement, as its line width is much smaller than the smallest resolution bandwidth of the OSA. Displayed in Figure 2.4, the measured response function is fitted by a Gaussian function after normalization with σ equal to 0.0085 nm. Therefore the Gaussian function can be considered as the instrument response function $H(\lambda)$ during the nonlinear fitting process. Figure 2.5 shows the RG product spectra of an AMQW laser at various currents calculated using the nonlinear fitting method.

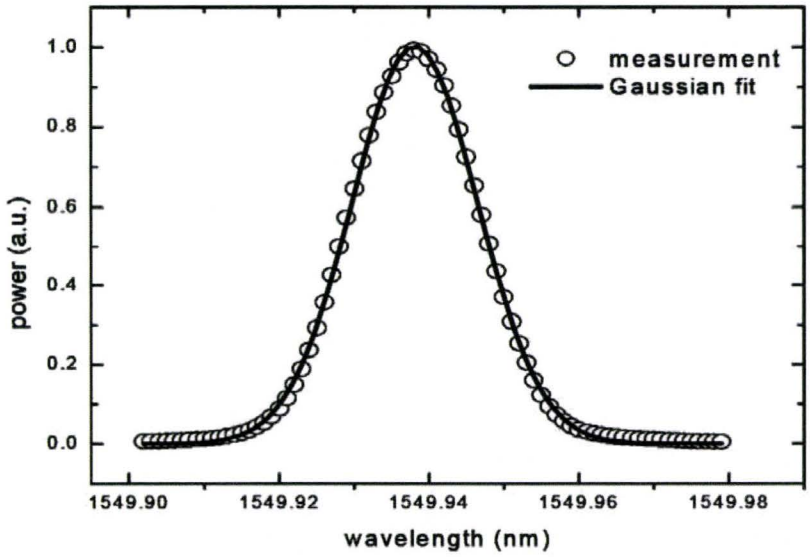

Figure 2.4 Measured response function of ANDO AQ6317B OSA fitted with a Gaussian function (σ=0.0085 nm). [44]

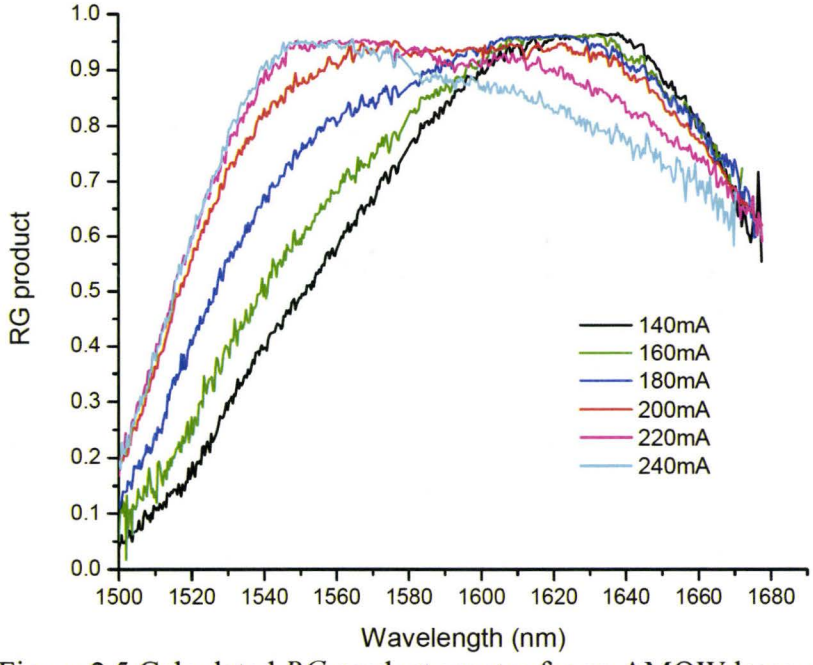

Figure 2.5 Calculated *RG* product spectra for an AMQW laser without coatings at various currents. The short and long wavelengths of the lasing limit are 1545 and 1640 nm, respectively. The non-lasing gap (RG<0.95) ranges from 1575 to 1600 nm.

2.3 Desired reflectance of a gain flattening coating

Aside from the efforts [33-36] to achieve broader and broader gain spectra by changing the separation of the short and long transition wavelengths, the number of long wavelength wells, the location of the different quantum wells, the barrier thicknesses and so forth, a well designed and fabricated coating adds another option to improve the optical properties of the AMQW laser.

In the attempt [22] to optimize the laser output by depositing a coating onto one of the laser facets, the optimum coating to lift the gain around the lasing edges is calculated from the gain spectrum at a certain current. It is defined as:

$$RG = \sqrt{R_1 R_2}\exp(gl) \tag{2.7}$$

where l is the cavity length, g is the gain coefficient, and R_1 and R_2 are the reflectances of the two laser facets. The method of calculating the effective index of the laser structure will be discussed in Chapter 3 and the reflectance of the uncoated facet is calculated via the Fresnel equations. Therefore, with the reflectance of two bare facets estimated, we can calculate the gain coefficient g from the measured RG product.

Based on that the gain coefficient g is fixed for one laser before and after any coating is applied, and with the condition for lasing ($RG \approx 1$) satisfied, we now obtain the optimum reflectance R (i.e., $\sqrt{R_1 R_2}$) for a certain current. Although both R_1 and R_2 can be altered to make up the optimum reflectance R, we will leave one facet reflectance as that of an uncoated facet and make the changes to the other facet. Therefore we can compare the experimental data before and after the fabrication, and evaluate the gain flattening coating with less complication. Note that $RG \approx 1$ is the theoretical condition, while using

different methods of deriving the *RG* product may give slightly different values of the *RG* product. From Figures 2.3 and 2.5 we notice that lasing is achieved when *RG* is equal to 0.95, which will be used throughout the calculation.

The *RG* product spectrum at a current of 200 mA (see Figure 2.5) is used for demonstration. The desired optimum reflectance for one of the laser facets at 200 mA is then calculated and shown in Figure 2.6, as the reflectance of the other facet is kept as that of an uncoated facet, which is ~30%. Note that any expected reflectance over 100% is impossible to materialize and therefore eliminated.

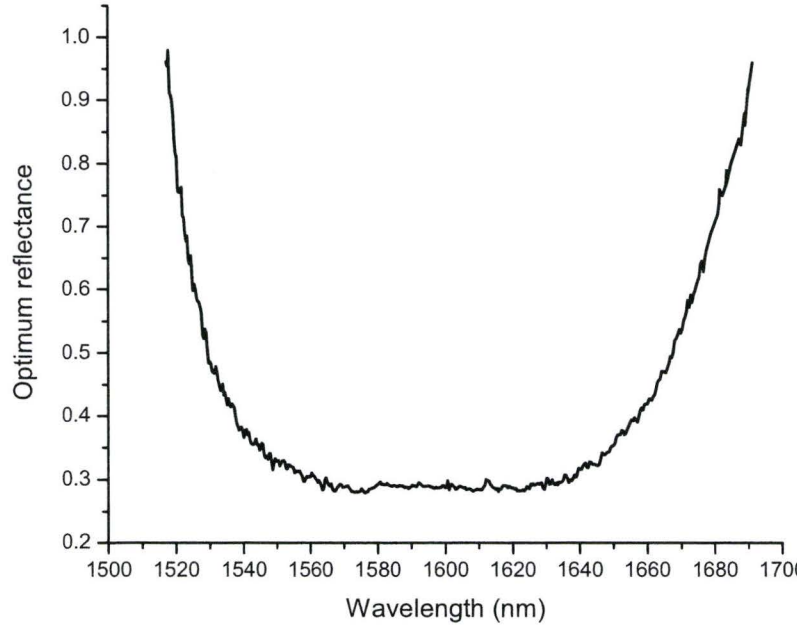

Figure 2.6 Optimum reflectance for the AMQW at a current of 200 mA.

The reflectance as a function of wavelength shown in Figure 2.6 is the target for a design to achieve. A laser with such a coating exactly designed and fabricated will achieve the full range of lasing at the current of 200 mA. There are two shortcomings if

we are limited by this idea. Firstly, the perfect design may not be manufacturable. The perfect design can always be approached by adding more layers, but any coating equipment has limits on thickness of each layer and the total thickness of coatings. Even when a coating equipment is capable of fabricating such coatings, it will be very hard to fabricate a coating giving the exact designed reflection with a minimum margin for errors. In reality, it only takes little deviation from the designed reflection to cause a non-lasing gap when no external feedback is utilized. Second, even if the facet is perfectly coated as designed, this coating is only good for the gain spectrum at one current and at that current the lasing wavelengths would be randomly chosen by the laser itself unless the external feedback is in place for the wavelength selection.

Therefore we propose here a coating that has a reflectance spectrum such that it allows continuous lasing without external feedback as the gain peak shifts with the increasing current. By examining Figures 2.3 and 2.5, it is noticed that after the device starts lasing, the lasing wavelength shifts to shorter wavelengths as the current increases. A non-lasing gap appears in the middle of the lasing range. If a coating is deliberately designed to have higher reflectance at longer wavelength and lower reflectance at shorter wavelength, we could force the wavelength in the non-lasing gap to receive more feedback to exceed that of the shorter wavelength. This will not affect the shorter wavelength that lases eventually, because the increasing current will continuously push the gain up towards the shorter wavelength before saturation is achieved.

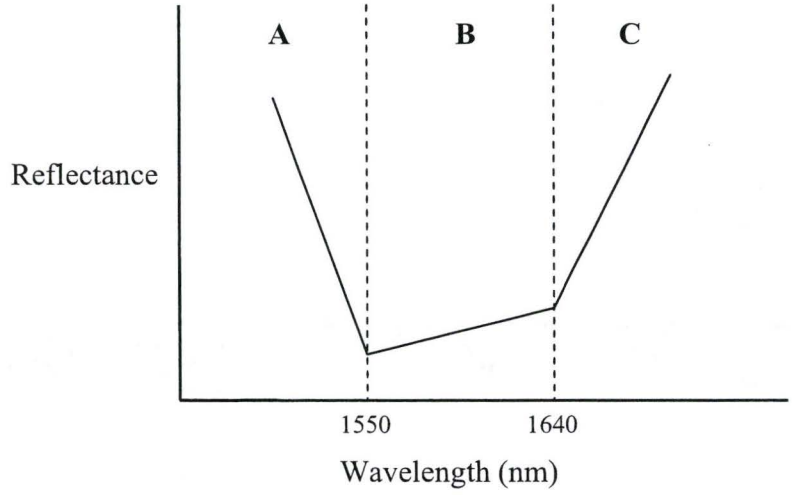

Figure 2.7 Schematic illustration of the reflectance of the gain flattening coating.

For the purpose of easy illustration, the desired reflectance curve is divided into three sections: A, B, and C (see Figure 2.7) with 1550 nm being the wavelength where the laser stops lasing at the saturation current, 1640 nm the wavelength where the laser starts lasing after the threshold current is reached. The non-lasing gap of the uncoated laser is located in the middle section, B. A and C sections are the wavelengths that do not lase in an uncoated laser, as the reflection of the bare facet doesn't contribute enough feedback to the *RG* product. As a part of the coating function, the lasing range is expected to extend. Therefore, reflections in sections A and C need to be increased. Because the laser starts to lase at the longer wavelength around 80 mA, the longer wavelength edge of the calculated optimum reflectance at a current of 80 mA will be used as section C for the reflectance of the eventual gain flattening coating. Similarly, section A is borrowed from the shorter wavelength edge of the calculated optimum reflectance of the laser at around 280 mA, just before saturation. The optimum reflectances for the laser at 80 mA and 280

mA are calculated using the same method to achieve the optimum reflectance for the current of 200 mA. Sections C and A of the gain flattening coating extend the lasing range at the threshold and saturation currents, when the current which drives the laser is modulated between 80 and 280 mA.

The main idea for the middle section of the gain flattening coating is to have the reflection higher at the longer wavelength end and lower at the shorter wavelength. The reason for that is the following: The wavelengths where the *RG* product is larger than 0.95 are lasing; as the gain peak shifts towards shorter wavelength with increasing currents, the sloped reflection curve helps the gain to "pick up" lasing wavelengths gradually moving towards shorter wavelength covering the entire range. This kind of reflection curve has an advantage in fabrication, because the desired reflection curve in section B permits a large tolerance. The laser current is used as a varying parameter to make up the deviation between the fabricated and targeted facet reflection; we can tolerate a little more design and fabrication error which is inevitable in practice. The only criterion for an acceptable reflection in section B is that the wavelengths where the *RG* product is larger than 0.95 must cover the entire range as the current increases. As a matter of fact, the middle section of the optimum reflectance curves at 240 mA is eligible. The final designed reflectance of the gain flattening coating is displayed in Figure 2.8.

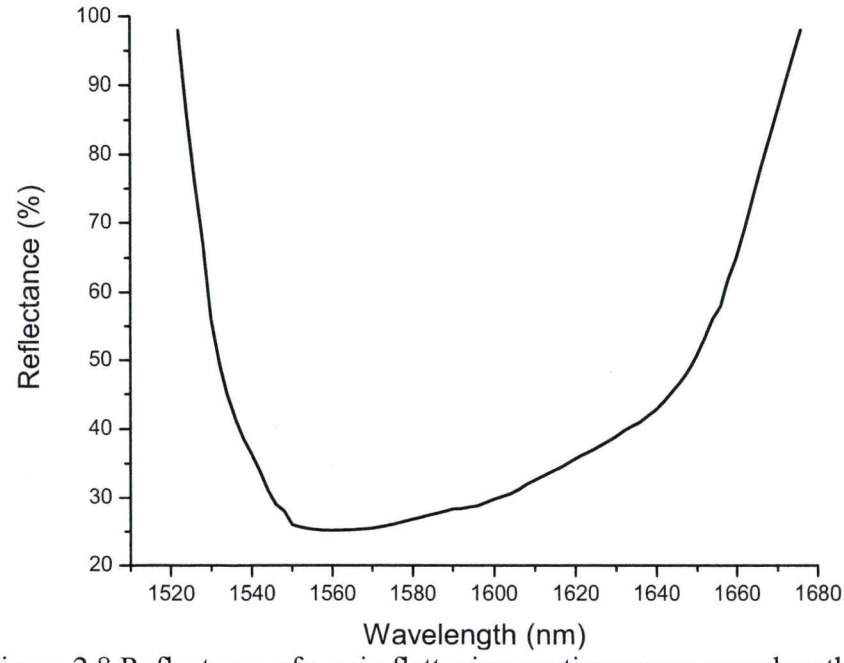

Figure 2.8 Reflectance of a gain flattening coating versus wavelength.

Chapter 3

Design of coatings

Thin film optical interference coatings have been studied intensively in the past. There are numbers of references [47-50] giving detailed analysis and design approaches. A brief description of these most important issues will be given here focusing on the applications involved in the current project. The notation of Ref. [48] will be used.

3.1 Reflectance and transmittance of a layered medium

First, reflectance and transmittance of a layered structure is formalized. Consider a plane electromagnetic (EM) wave incident from the air on the surface of layered optical thin films. Part of the EM wave will be reflected back to the air; part of the EM wave will be transmitted into the layered films. When the air and the layers are non-magnetic, the Maxwell equations will be:

$$\nabla \times \breve{E} = -\frac{1}{c}\frac{\partial \breve{H}}{\partial t}, \quad \nabla \times \breve{H} = \frac{\varepsilon}{c}\frac{\partial \breve{E}}{\partial t} + \frac{4\pi\sigma}{c}\breve{E} \tag{3.1}$$

$\breve{E}$ is the electric vector of the EM wave, $\breve{H}$ is the magnetic vector of the EM wave, ε is the permittivity, σ is the electrical conductivity and c is the velocity of light in vacuum.

The solution of equation (3.1) with specified boundary conditions will describe the reflection and transmission of the EM wave in the media.

Let us consider the incident light as a plane monochromatic ω–frequency wave:

$$\breve{E} = \vec{E}\exp(i\omega t)\ ,\quad \breve{H} = \vec{H}\exp(i\omega t) \tag{3.2}$$

where $\vec{E}$ and $\vec{H}$ are only spatially dependent. Now, equation (3.1) can be rewritten as:

$$\nabla \times \vec{E} = ik\vec{H}\ ,\quad \nabla \times \vec{H} = ik\tilde{\varepsilon}\vec{E} \tag{3.3}$$

where $k = \frac{2\pi}{\lambda}$ is the wave number of the incident wave, and $\tilde{\varepsilon} = \varepsilon - i\frac{4\pi\sigma}{c}$ is the complex permittivity of the medium. To discuss further the detail, we need to decompose the EM field into two components: TE and TM polarization as shown in Figure 3.1. TE or sometimes called S-component, means that the electric vector is perpendicular to the plane of incidence. TM or P-component features the electric vector parallel to the plane of incidence.

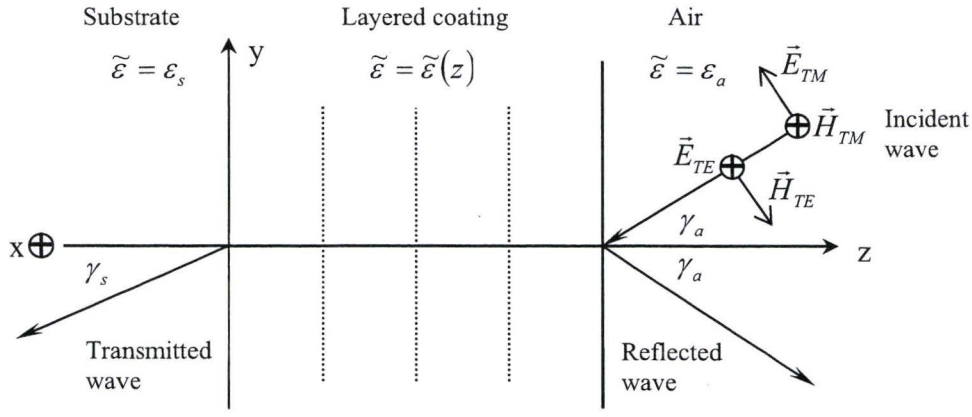

Figure 3.1 Orientation of the electric and magnetic vectors in the TE and TM polarization cases.

In TE polarization, the scalar form of equations (3.3) is:

$$H_x = 0\,;\ \frac{\partial E_x}{\partial z} = -ikH_y\,;\ \frac{\partial E_x}{\partial y} = ikH_z\,;\ \frac{\partial H_z}{\partial y} - \frac{\partial H_y}{\partial z} = ik\tilde{\varepsilon}(z)E_x\,;\ \frac{\partial H_z}{\partial x} = 0\,;\ \frac{\partial H_y}{\partial x} = 0 \text{ (3.4 a-f)}$$

Substituting the second and third equations into the fourth one, we obtain:

$$\frac{\partial^2 E_x}{\partial y^2} + \frac{\partial^2 E_x}{\partial z^2} + k^2\tilde{\varepsilon}(z)E_x = 0 \tag{3.5}$$

To apply the variable separation method, we set $E_x(y,z) = u(z)g(y)$, substitute it into the equation (3.5) and obtain:

$$-\frac{1}{g(y)}\frac{d^2 g}{dy^2} = \frac{1}{u(z)}\left[\frac{d^2 u}{dz^2} + k^2\tilde{\varepsilon}(z)u(z)\right] \tag{3.6}$$

Equation (3.6) can depend neither on y nor on z, and therefore, has to be equal to a certain constant. It is convenient to assume it equal to $k^2\alpha^2$ with α equal to $\sqrt{\varepsilon_a}\sin\gamma_\alpha$, as is shown in Appendix A.

Now we have $g(y) = \exp(ik\alpha y)$ and $E_x(y,z) = u(z)\exp(ik\alpha y)$. From equations (3.4 b) and (3.4 c) we can see that H_y and H_z have a similar type of dependence on y. We could obtain $H_z(y,z) = \alpha u(z)\exp(ik\alpha y)$.

Assuming $H_y = -v(z)\exp(ik\alpha y)$, then the vector functions $\vec{E}$ and $\vec{H}$ can be written as:

$$\vec{E} = \{u(z), 0, 0\}\exp(ik\alpha y)$$

$$\vec{H} = \{0, -v(z), \alpha u(z)\}\exp(ik\alpha y) \tag{3.7}$$

where $u(z)$ and $v(z)$ are the solutions of the following equations:

$$\frac{du}{dz} = ikv\,, \qquad \frac{dv}{dz} = ik\left[\tilde{\varepsilon}(z) - \alpha^2\right]u \tag{3.8}$$

Equations (3.8) are valid for a field at every continuity point of $\tilde{\varepsilon}(z)$. At the discretion points of $\tilde{\varepsilon}(z)$, i.e., at the boundaries of layers, the tangential components of $\vec{E}$ and $\vec{H}$ must be continuous.

The $\vec{E}$ and $\vec{H}$ vectors of TM polarization can be similarly derived:

$$\vec{E} = \left\{0, u(z), -\frac{\alpha}{\tilde{\varepsilon}(z)} v(z)\right\} \exp(ik\alpha y)$$

$$\vec{H} = \{v(z), 0, 0\} \exp(ik\alpha y) \tag{3.9}$$

where $u(z)$ and $v(z)$ are the solutions of the following equations:

$$\frac{du}{dz} = ik\left[1 - \frac{\alpha^2}{\tilde{\varepsilon}(z)}\right] v, \qquad \frac{dv}{dz} = ik\tilde{\varepsilon}(z) u \tag{3.10}$$

To obtain the general expressions for the transmittance and reflectance of a multilayer coating, TE and TM polarizations need to be considered separately. In TE polarization, we use equations (3.8) and let $q = \sqrt{\tilde{\varepsilon} - \alpha^2} = \sqrt{\tilde{\varepsilon}} \cos\gamma$. There being a finite number of homogeneous layers between the substrate and air (Figure 3.2), the equations (3.8) are also valid for the substrate and air, where $q_a = \sqrt{\varepsilon_a - \alpha^2} = \sqrt{\varepsilon_a} \cos\gamma_a$ and $q_s = \sqrt{\tilde{\varepsilon}_s - \alpha^2} = \sqrt{\tilde{\varepsilon}_s} \cos\gamma_s$. In air, equations (3.8) can be written as:

$$\frac{d^2u}{dz^2} + k^2(\varepsilon_a - \alpha^2) u = 0 \tag{3.11}$$

with two linearly independent solutions: $\exp(ikq_a z)$ and $\exp(-ikq_a z)$. Therefore, it follows from the first equation of (3.8) that for the incident wave, $v = q_a u$ and for the reflected wave, $v = -q_a u$. If we denote amplitudes of tangential components of the

electric vector of the incident and reflected waves as E_A and E_R at the boundary of z_a, then, for the incident wave, we have $u(z_a,k)=E_A$ and $v(z_a,k)=q_aE_A$, and for the reflected wave, $u(z_a,k)=E_R$ and $v(z_a,k)=-q_aE_R$. Note that u and v depend not only on z, but also on the wavenumber k. Similarly, at the boundary of the substrate we have $u(0,k)=E_T$ and $v(0,k)=-q_sE_T$.

By definition, the transmissivity and reflectivity are defined as $t=E_T/E_A$ and $r=E_R/E_A$. For simplicity, E_T could be set equal to 1, and E_A and E_R be normalized accordingly. Now, with the initial condition:

$$u(0,k)=1\ ,\quad v(0,k)=-q_s \tag{3.12}$$

We have $u(z_a,k)=E_R+E_A$ and $v(z_a,k)=q_a(E_A-E_R)$ at the outer space boundary. Then the transmissivity and reflectivity can be expressed as:

$$t(k)=\frac{2q_a}{q_au(z_a,k)+v(z_a,k)}\ ,\quad r(k)=\frac{q_au(z_a,k)-v(z_a,k)}{q_au(z_a,k)+v(z_a,k)} \tag{3.13}$$

Now we focus on the layer structure (Figure 3.2) and see how $u(z_a,k)$ and $v(z_a,k)$ are determined by the layer thickness d_j and the refractive index $\tilde{n}_j=\sqrt{\tilde{\varepsilon}_j}$. The *j-th* layer of equations (3.8) is written as follows:

$$\frac{du}{dz}=ikv\ ,\qquad \frac{dv}{dz}=ik\left(\tilde{n}_j^2-\alpha^2\right)u \tag{3.14}$$

And the second order differential equation for u is:

$$\frac{d^2u}{dz^2}+k^2\left(\tilde{n}_j^2-\alpha^2\right)u=0 \tag{3.15}$$

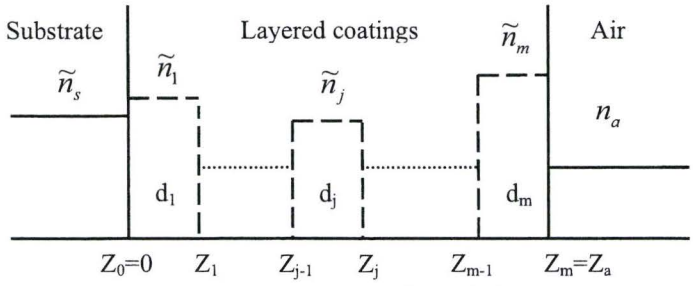

Figure 3.2 Coatings with m layers between air and the substrate. $\tilde{n}_j$ is the complex refractive index and d_j is the thickness of the *j-th* layer. $\tilde{n}_s$ and n_a are the refractive index of the substrate and air.

Since $\alpha = n_a \sin\gamma_a = \tilde{n}_s \sin\gamma_s = \tilde{n}_j \sin\gamma_j$ (Appendix A), equation (3.15) can be written as:

$$\frac{d^2u}{dz^2} + \left(k\tilde{n}_j \cos\gamma_j\right)^2 u = 0 \tag{3.16}$$

The general solution of (3.16) is the combination of two linear independent solutions:

$$u(z) = c_1 \cos\left(k\tilde{n}_j \cos\gamma_j \left(z - z_{j-1}\right)\right) + c_2 \sin\left(k\tilde{n}_j \cos\gamma_j \left(z - z_{j-1}\right)\right) \tag{3.17}$$

By assuming $z = z_{j-1}$ we have $c_1 = u\left(z_{j-1}\right)$. Differentiating with respect to z and assuming $z = z_{j-1}$ again, we obtain $c_2 = iv\left(z_{j-1}\right)/\tilde{n}_j \cos\gamma_j$. With the designation of $q_j = \tilde{n}_j \cos\gamma_j$ and an angular phase thickness $\varphi_j = k\tilde{n}_j \cos\gamma_j d_j$ ($d_j = z_j - z_{j-1}$), at $z = z_j$, we have:

$$u\left(z_j\right) = u\left(z_{j-1}\right)\cos\varphi_j + \left(i/q_j\right)v\left(z_{j-1}\right)\sin\varphi_j \tag{3.18}$$

Differentiating $u(z)$ and substituting it into the first equation of (3.14), at $z = z_j$, we obtain:

$$v\left(z_j\right) = iq_j u\left(z_{j-1}\right)\sin\varphi_j + v\left(z_{j-1}\right)\cos\varphi_j \tag{3.19}$$

The equations (3.18) and (3.19) can be written in a matrix format as follows:

$$\begin{pmatrix} u \\ v \end{pmatrix}_{z=z_j} = M_j \begin{pmatrix} u \\ v \end{pmatrix}_{z=z_{j-1}}, \text{ where } M_j = \begin{pmatrix} \cos\varphi_j & (i/q_j)\sin\varphi_j \\ iq_j \sin\varphi_j & \cos\varphi_j \end{pmatrix} \tag{3.20}$$

M_j is the characteristic matrix of the *j-th* layer. Since the u and v functions are continuous at the boundaries of all the layers, we could multiply the recurrent item to obatin:

$$\begin{pmatrix} u \\ v \end{pmatrix}_{z=z_a} = M \begin{pmatrix} u \\ v \end{pmatrix}_{z=0}, \text{ where } M = M_m M_{m-1} \cdots\cdots M_1 = \begin{pmatrix} m_{11} & m_{12} \\ m_{21} & m_{12} \end{pmatrix} \tag{3.21}$$

M, the product of the characteristic matrices of all layers, is known as the characteristic matrix of the multilayer coating. Substituting the initial condition (3.12) into equation (3.21), we obtain:

$$u(z_a, k) = m_{11} + m_{12} q_s, \qquad v(z_a, k) = m_{21} + m_{22} q_s \tag{3.22}$$

Substituting equations (3.22) into equations (3.13), we obtain the expression for the transmissivity and reflectivity:

$$t(k) = \frac{2q_a}{q_a m_{11} + q_s m_{22} + q_a q_s m_{12} + m_{21}}$$

$$r(k) = \frac{q_a m_{11} - q_s m_{22} + q_a q_s m_{12} - m_{21}}{q_a m_{11} + q_s m_{22} + q_a q_s m_{12} + m_{21}} \tag{3.23}$$

The derivation for the TM polarization is similar and the equivalent equations could be obtained with a different definition of q, where $q_a = n_a / \cos\gamma_a$, $q_s = \tilde{n}_s / \cos\gamma_s$ and $q_j = \tilde{n}_j / \cos\gamma_j$. The transmittance and reflectance are therefore obtained through:

$$T = \frac{q_a}{q_s}|t|^2 = \frac{q_a}{q_s} t \cdot t^*, \quad R = |r|^2 = r \cdot r^* \tag{3.24}$$

In the case of non-polarized incident light, the total transmittance and reflectance are the average of transmittance and reflectance contributed by TE and TM polarizations:

$$T = \frac{1}{2}(T_{TE} + T_{TM}), \qquad R = \frac{1}{2}(R_{TE} + R_{TM}) \tag{3.25}$$

3.2 Synthesis of a coating with the needle method

When designing a routine optical interference coating such as an AR coating, HR coating, edge filter, band pass filter, etc., one usually starts with certain designs [47-50] developed over the years, followed by practical refinements according to the material availability and manufacturability. These designs usually feature a stack of quarter-wave thick materials with high and low refractive indices. Then certain layers are added to broaden/narrow/shift the high or low reflection area of the reflectance spectrum to meet the requirement. However, when designing a coating such as that with the reflectance spectrum displayed in Figure 2.8, one often resorts to the optimization of a merit function.

For one specific design of an optical coating, the merit function is defined as:

$$F(X) = \sum_{l=1}^{L} W_l [R(X, \lambda_l) - R_T(\lambda_l)]^2 \tag{3.26}$$

where $X = \{d_1, d_2, \ldots, d_m\}$ are the physical thicknesses of all the layers, if the refractive indices and their alternation order are set. $R(X, \lambda_l)$ is the calculated reflectance spectrum and $R_T(\lambda_l)$ is the targeted reflectance spectrum. W_l is the weight function which allows the designer to choose and emphasize specific areas. λ_l is a set of wavelength values where the reflectance of the designed coating is compared with the target reflectance. L is the total number of comparison points.

The merit function indicates how close the designed reflectance is to the target reflectance. The optimization procedure is to search for the global minimum of the merit function. Even if the global minimum for a given number of layers were found, however, it does not guarantee that the design is good enough and therefore, more layers may need to be added. As the number of layers grows, for example, from 6 to 10, the local minima of the merit function become hundreds and thousands, which already makes the direct search for the global minimum practically impossible. Virtually all non-local design techniques use local optimization in at least one step of the design procedure, however, the so called needle optimization technique is a non-local design approach [51]. The synthesis method based on the needle-like variation of the refractive index was first mentioned in 1982 [52] and fully demonstrated [53] later on. In the following, we give a brief description of this technique.

In the previous section, the tangential components of electric and magnetic vectors $u(z,k)$ and $v(z,k)$ were introduced. Admittance A is defined as $A(z,k)=v(z,k)/u(z,k)$. Admittance at point z_a, i.e., the boundary between the coating and air is known as the input admittance. The second equation in (3.13) can be expressed through the input admittance as:

$$r(k)=\frac{q_a-A(z_a,k)}{q_a+A(z_a,k)} \quad \text{or} \quad r(\lambda)=\frac{q_a-A(z_a,\lambda)}{q_a+A(z_a,\lambda)} \tag{3.27}$$

Based on the fact that in the project we are only concerned about normal incidence and non-absorbing thin films, q now becomes n. $A(z_a,\lambda)$ can be calculated from equations (3.8), which can be rewritten as:

$$\frac{dA}{dz} = i\frac{2\pi}{\lambda}\left[n^2(z) - A^2(z,\lambda)\right] \tag{3.28}$$

with the initial condition: $A(0,k) = n_s$. $n(z)$ is a piecewise continuous function, which contains all the information about the coating layers, including the refractive index and thickness. The merit function now is written as:

$$F[n(z)] = \sum_{l=1}^{L} W_l \left[R(n(z),\lambda_l) - R_T(\lambda_l)\right]^2 \tag{3.29}$$

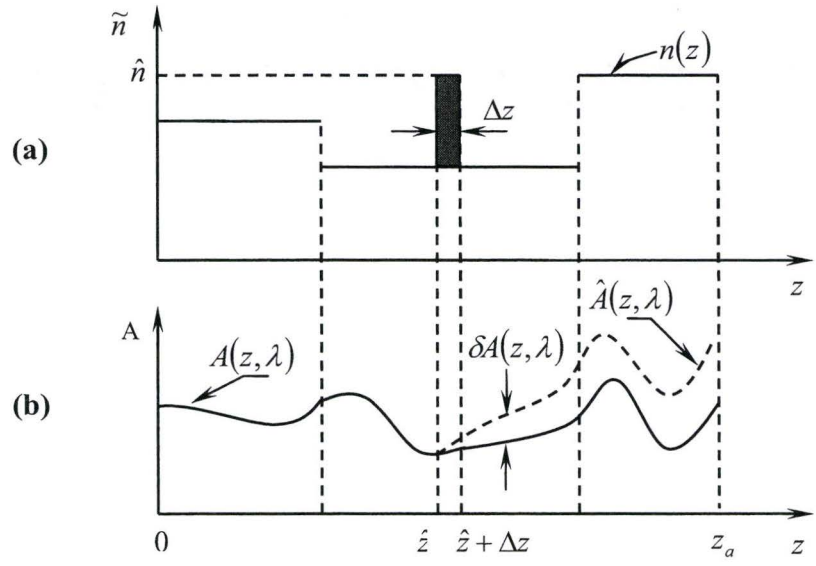

Figure 3.3 Needle variation of the refractive index and corresponding changes of the admittance.

The principal idea of the needle method is to find where to insert a thin optical layer in order to decrease the merit function most effectively. Illustrated in Figure 3.3, after a thin layer with thickness Δz and refractive index $\hat{n}$ is inserted at $\hat{z}$, the admittance A changes to $\hat{A}$.

The term "needle method" comes from the shape of that refractive index variation with small Δz. Let us name the new refractive index profile as $n'(z)$. $\hat{A}(z,\lambda)$ is the admittance after the insertion of the needle layer and the solution of:

$$\frac{d\hat{A}}{dz} = i\frac{2\pi}{\lambda}\left[n'^2(z) - \hat{A}^2(z,\lambda)\right] \tag{3.30}$$

with the same initial condition as before: $\hat{A}(0,\lambda) = n_s$.

Assuming $\hat{A}(z,\lambda) = A(z,\lambda) + \delta A(z,\lambda)$, subtracting equation (3.28) from (3.30), taking into account that $n'(z)$ and $n(z)$ are identical on $[\hat{z} + \Delta z, z_a]$, and neglecting the square of $\delta A(z,\lambda)$, we have:

$$\frac{d\delta A}{dz} = -i\frac{4\pi}{\lambda}A(z,\lambda)\delta A(z,\lambda) \tag{3.31}$$

The initial condition for the solution is obtained from equation (3.28) at $\hat{z}$:

$$\delta A(\hat{z},\lambda) = i\frac{2\pi}{\lambda}\left[\hat{n}^2 - n^2(z)\right]\Delta z \tag{3.32}$$

From equation (3.27), we know that with the change of the input admittance by the value of $\delta A(z_a,\lambda)$, the reflectivity increases by:

$$\delta r(\lambda) = -\frac{[1 + r(\lambda)]^2}{2n_a}\delta A(z_a,\lambda) \tag{3.33}$$

With the help of the second equation of equations (3.24), the reflectance increases by:

$$\delta R(\lambda) = 2\,\mathrm{Re}\{r^*(\lambda)\delta r(\lambda)\} = -\frac{1}{n_a}\mathrm{Re}\left\{r^*(\lambda)[1 + r(\lambda)]^2\,\delta A(z_a,\lambda)\right\} \tag{3.35}$$

and the merit function changes by:

$$\delta F = 2\sum_{l=1}^{L} W_l [R(\lambda_l) - R_T(\lambda_l)]\delta R(\lambda_l)$$
$$= -\frac{2}{n_a}\sum_{l=1}^{L} W_l [R(\lambda_l) - R_T(\lambda_l)] \cdot \mathrm{Re}\left\{r^*(\lambda_l)[1+r(\lambda_l)]^2 \delta A(z_a, \lambda_l)\right\} \tag{3.36}$$

To make equation (3.36) more convenient for calculation, a conjugate equation is introduced:

$$\frac{d\psi}{dz} = i\frac{4\pi}{\lambda} A(z,\lambda)\psi(z,\lambda) \tag{3.37}$$

It is a linear differential equation with respect to function ψ, and the solution of equation (3.28) for admittance is its coefficient. Because we are comparing the calculated reflection with the design target at L points, the boundary condition at point z_a for equation (3.37) also needs to be set for L times:

$$\psi(z_a, \lambda_l) = \frac{2}{n_a} W_l [R(\lambda_l) - R_T(\lambda_l)] r^*(\lambda_l)[1+r(\lambda_l)]^2 \tag{3.38}$$

So, equation (3.36) can be rewritten as:

$$\delta F = -\sum_{l=1}^{L} \mathrm{Re}\{\psi(z_a, \lambda_l)\delta A(z_a, \lambda_l)\} \tag{3.39}$$

At any z in the segment of $[\hat{z}, z_a]$, differentiating the product of $\psi(z,\lambda)$ and $\delta A(z,\lambda)$, with the help of equations (3.31) and (3.37), we have $\frac{d[\psi(z,\lambda)\delta A(z,\lambda)]}{dz} = 0$, which means that the product of $\psi(z,\lambda)$ and $\delta A(z,\lambda)$ is independent of z, i.e.,

$$\psi(z_a, \lambda)\delta A(z_a, \lambda) = \psi(\hat{z}, \lambda)\delta A(\hat{z}, \lambda) \tag{3.40}$$

Substituting equation (3.40) into (3.39) and taking into account the initial condition equation (3.32), we obtain:

$$\delta F = 2\pi \sum_{l=1}^{L} \frac{1}{\lambda_l} \mathrm{Im}\{\psi(\hat{z}, \lambda_l)\} \left[\hat{n}^2 - n^2(\hat{z})\right] \Delta z \tag{3.41}$$

We define the P function as:

$$P(z) = 2\pi \sum_{l=1}^{L} \frac{1}{\lambda_l} \mathrm{Im}\{\psi(\hat{z}, \lambda_l)\} \tag{3.42}$$

Equation (3.41) can be then written as:

$$\delta F = P \cdot \left[\hat{n}^2 - n^2(\hat{z})\right] \cdot \Delta z \tag{3.43}$$

This is the final expression for the value of the merit function change. An important property of the P function is that it is independent of the needle-like variation of the refractive index and only depends on the refractive index profile $n(z)$. When calculating the P function, it is necessary to provide the numerical solution of equation (3.28) for L different wavelengths and then to integrate in the reverse direction the conjugate equation (3.37) with the initial condition (3.38).

Let consider this method in a real design, for instance, to synthesize a coating from two materials with refractive indices, n_H and n_L. Corresponding to a three layer structure in Figure 3.4 (a), the P function is calculated and displayed in Figure 3.4 (b). At sufficiently small Δz, the decrease of the merit function is guaranteed, if either $n(\hat{z}) = n_L$ and $P(\hat{z}) < 0$, or $n(\hat{z}) = n_H$ and $P(\hat{z}) > 0$ are satisfied simultaneously. The sufficient smallness of Δz is mentioned because the accuracy of equation (3.43) increases as Δz decreases. In this case, the insertion of a thin layer of high refractive index material at $\hat{z}$ can ensure the greatest decrease of the merit function. The needle-like refractive index variation can be applied to one place or at several places simultaneously, however, the

layer inserted may be too thin to be practically manufactured. An optimization process is thus necessary to the newly altered refractive index profile $n(z)$.

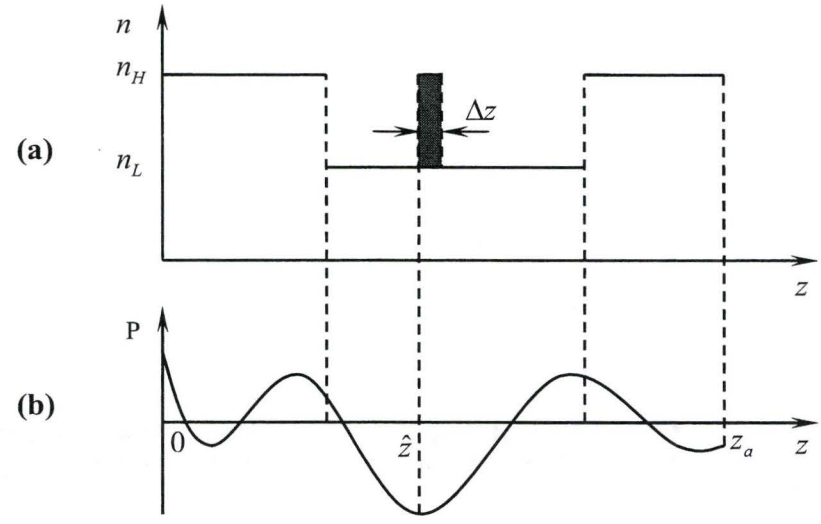

Figure 3.4 (a) Needle-like variation of the refractive index at $\hat{z}$.
(b) P function for the three layer structure in (a).

3.3 Optimization methods

Many optimization algorithms have been developed over the years. The most widely used optimization methods for coating designs are the simplex method [54], the gradient method [55] (sometimes called steepest descent method), the damped least squares method [56], the Monte Carlo method [57], and others. The gradient method will be explained briefly here, since it is efficient and used in most of my designs.

As defined before, $X = \{d_1, d_2, \ldots, d_m\}$ represents the physical thickness of all the layers. We can write the merit function gradient:

$$\nabla F(X) = \left\{ \frac{\partial F}{\partial d_1}, \frac{\partial F}{\partial d_2}, \ldots, \frac{\partial F}{\partial d_m} \right\} \tag{3.44}$$

Numerically, the derivatives of the merit function can be approximately calculated by:

$$\frac{\partial F}{\partial d_k} \approx \frac{F(d_1, \ldots, d_k + \Delta d_k, \ldots, d_m) - F(d_1, \ldots, d_k, \ldots, d_m)}{\Delta d_k} \tag{3.45}$$

Let us designate X^0 as the starting design. Vector $-\nabla F$, opposite in its direction to the merit function gradient, is known as the anti-gradient. It shows the direction of fastest decrease of the merit function.

In the steepest descent method, the descent occurs from the starting point X^0 in the direction of $-\nabla F(X^0)$. It is analogous to seeking the minimum of a single variable function $\eta(\rho) = F[X^0 - \rho \nabla F(X^0)]$ along the straight line of $X^0 - \rho \nabla F(X^0)$ in the parameter space. There are many ways to find the minimum value of $\eta(\rho)$. The simplest one, called one-dimensional minimization, is to set a certain step value h along the anti-gradient direction and then let the sequential motion proceed in the parameter space, which is expressed as: $-h\nabla F$. After taking the p-th step, we have $X^0 - ph\nabla F(X^0)$. At every step it is verified if the η function is decreasing, i.e., is $\eta(ph) < \eta[(p-1)h]$? Once the η function is found to no longer decrease, one step backward is taken and that point is considered as the minimum coordinate along the set anti-gradient direction. The one-dimensional minimization can be replaced by higher precision methods such as parabolic interpolation using the last three points and determining the minimum point on the obtained parabola. No matter what, the step size h needs to be adjusted by trial and error, since small h values cause calculation time to be wasted and large h values may result in an increase of the merit function already in the first step.

Once the minimum point (named as X^1) is obtained, $F(X^1)$ is calculated at X^1 and a descent along a new anti-gradient can be found. As a result of a series of similar descents, we have a sequence of points:

$$X^0, X^1, \ldots, X^k, \ldots$$

Where the merit function decreases monotonously:

$$F(X^0) > F(X^1) > \ldots > F(X^k) > \ldots$$

The steepest method is interrupted when certain criteria are met. For example, a relatively small number ζ can be set. Whenever $\frac{F(X^{k-1}) - F(X^k)}{F(X^{k-1})} < \zeta$ becomes valid, the process will be terminated.

The steepest descent method usually gives a fast decrease of the merit function along the first few directions of the minimization. Then the speed of the decreases slows down radically as the number of the merit function variables, i.e., the number of the layers, increases. The conjugate gradient method [58] is utilized to deal with this kind of situation. Instead of choosing the anti-gradient direction in the steepest descent method, an adjusted direction depending on the previous descent direction is taken. Let X^k be a point after the *k*-th process of the steepest descent method and we have $\nabla F(X^k)$ as the merit function gradient value at that point. Then the conjugate gradient method is introduced and we designate p_{k+1} as the vector direction of the *k+1*-th minimization. p_{k+1} is determined by the following equation:

$$p_{k+1} = -\nabla F(X^k) + \beta_k p_k \tag{3.46}$$

Where β_k is the factor adjusting the anti-gradient direction towards the previous direction of descent and is decided by:

$$\beta_k = \frac{\nabla F(X^k) \cdot [\nabla F(X^k) - \nabla F(X^{k-1})]}{|\nabla F(X^k)|^2} \tag{3.47}$$

Then the steepest descent is called in again for a few times of minimization before another conjugate gradient is applied. The combination of the steepest descent and conjugate gradient methods in such a fashion can reduce the merit function efficiently.

3.4 Practical design issues

3.4.1 Design strategy

When designing a coating using the needle optimization method, we use the following procedure (see Figure 3.5). First, a starting design is chosen. The merit function will be calculated and optimized using methods mentioned in the previous section. Then the calculation of the P function indicates where to insert the thin layers. The optimization of the merit function will be applied to the newly modified layer structure. This cycle of needle optimizations will be repeated until the expected reflection spectrum is achieved. Two issues need to be considered before the optimization takes place:

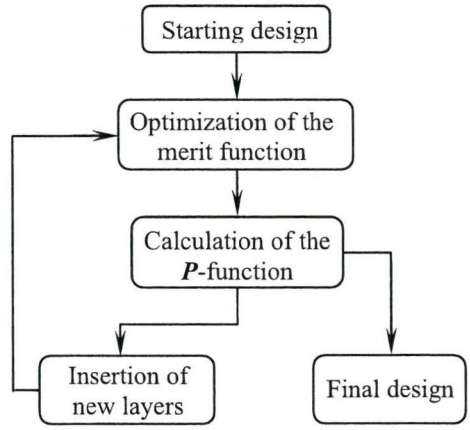

Figure 3.5 Flowchart of the needle optimization procedure.

1. Starting design. Although the starting design is not very critical to achieving a good final design, choosing the starting design from a known design having a reflectance similar to the target is helpful. When designing a coating involving a high reflectance at some wavelength, a stack of films with quarter-wavelength optical thickness (i.e., the product of physical thickness and its refractive index) of high and low refractive index materials is a good starting point.
2. Target selection. In general, using fewer points reduces calculation time, but too sparse a wavelength grid may slow down the convergence routines dramatically. An accurate specification of target spectral characteristics requires dense wavelength grids, however, too many wavelength points require too much calculation time. The spacing between the wavelength points is not necessarily uniform. It is recommended to assign dense wavelength grids to the areas of abrupt spectral characteristic, while the areas featuring flat spectral characteristics could have fewer points. Also W_l in

equation 3.26 can be specified to give priority to certain spectral areas where the target needs to be achieved more precisely.

Most of the time, the final design is still not satisfactory even when calculation of the *P*-function has shown that insertion of any layer will no longer decrease the merit function. To overcome that problem, we can synthesize a coating by gradual evolution. Figure 3.6 shows the synthesis by gradual evolution based on the needle optimization technique.

Whenever the *P*-function can no longer be improved by insertion of additional layer, the total optical thickness of the coating will be forced to increase. It can be achieved by either increasing every layer in proportion or randomly increasing one layer, as long as the total optical thickness is increased. Then a new round of the needle optimization cycle will begin. The procedure is repeated until a satisfactory solution is achieved. The synthesis by gradual evolution is a non-monotonic optimization procedure, in which the merit function value is typically increased after each intentional increase of the design total optical thickness but is decreased again after each new cycle of the needle optimization procedure.

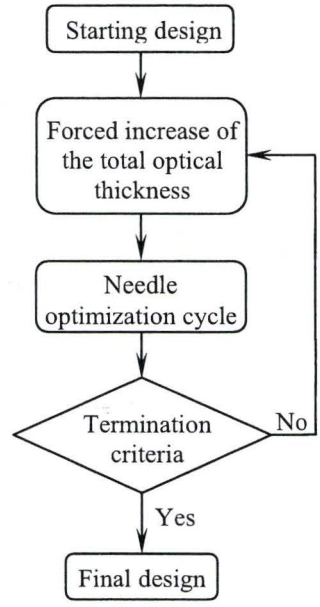

Figure 3.6 Flowchart of the synthesis by gradual evolution based on the needle optimization technique.

It has been found that a certain minimum overall optical thickness is required for a solution to a given problem, no matter what design method is employed [59]. A systematic study of the role of the design total optical thickness shows that it is possible to achieve low merit function values only at the expense of increasing the design total optical thickness [60]. Therefore, it is entirely up to the designer when to stop the gradual evolution. Since the design is hardly perfect, it is only sensible to talk about practically optimal solutions. Such "optimal solutions" are different for different designers and eventually depend on the growth system, as the designer has to balance wisely between the optimal design and manufacturability. The common criteria for termination of the gradual evolution are the required merit function value, the maximum allowed total optical thickness and the maximum allowed total number of design layers.

In the ICP-CVD system, we have grown stacks of silicon oxide films on laser facets with total thicknesses of up to 4 μm without cracking after cooling down to room temperature or other optical deterioration during the laser operation. The total number of layers is decided by the following facts. During the deposition of films, the thickness and refractive index of the layers are monitored by the in-situ spectroscopic ellipsometer. The extraction of the film thickness and refractive index from ellipsometry involves data collection, and model fitting. In the experiment, it is discovered that in our particular spectroscopic ellipsometer (Woollam M-44) the model fitting for thickness and refractive index is good for up to 6 layers, after which there are too many parameters for reliable results to fit. Also, the laser facet is too small for the in-situ spectroscopic ellipsometric measurement and a witness sample has to be used. In a real process, we replace the witness sample after deposition of 6 layers. Therefore, the total number of layers is set as multiples of 6. It is preferred to have layers no thinner than 40 nm, the reasons for which are discussed later.

The needle optimization technique is based on insertions of new thin layers in the design. Although the initially thin layers usually become much thicker in the course of the needle optimization procedure, it is still likely to have very thin layers, and therefore, it is important to have a program to remove those thin layers. When removing thin layers, they are substituted by thin layers with the same optical thickness but alternative refractive index, which is schematically illustrated in Figure 3.7. After removal of thin layers, the design is optimized again. Usually thin layers with physical thickness less than

10 nm can be removed from the final design without noticeable degradation of the merit function value.

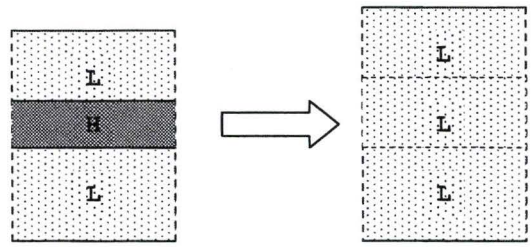

Figure 3.7 Schematic illustration of the removal of a thin layer from a coating design. H and L are the materials with high and low refractive index.

Reduction of the total number of design layers is also practically useful. In order for this to work, we need to stop the gradual evolution process when better than actually required approximation of design targets is achieved. Therefore, we can allow some increase of the merit function caused by a design simplification. The same operations as for the thin film layer removal are used to reduce the total number of design layers at the expense of the allowed merit function increase. The reduction process is organized so as to first remove those layers whose removal causes the least degradation of the merit function (not necessarily thin layers). Usually an allowed merit function increase of 5-20% is tolerated to reduce the total number of design layers.

3.4.2 Coating materials and refractive index of the laser diode

Usually the refractive index of the coating material is fixed due to the material availability, however the refractive indices of silicon oxides with different oxygen contents grown in the ICP-CVD system can vary in a certain range. Theoretically, guidelines for choosing the refractive indices of the coating materials are provided by the

maximum principle [61-62] in thin film optics. The maximum principle shows that when we design a coating to match the target reflectance, the best approximation of a target is provided by a design with two alternating refractive indices, i.e., a design comprising only two materials. If more than two materials are available, the best results are achieved with the pair of materials having the lowest and the highest refractive indices. In practice, we choose materials also based on manufacturability and reproducibility.

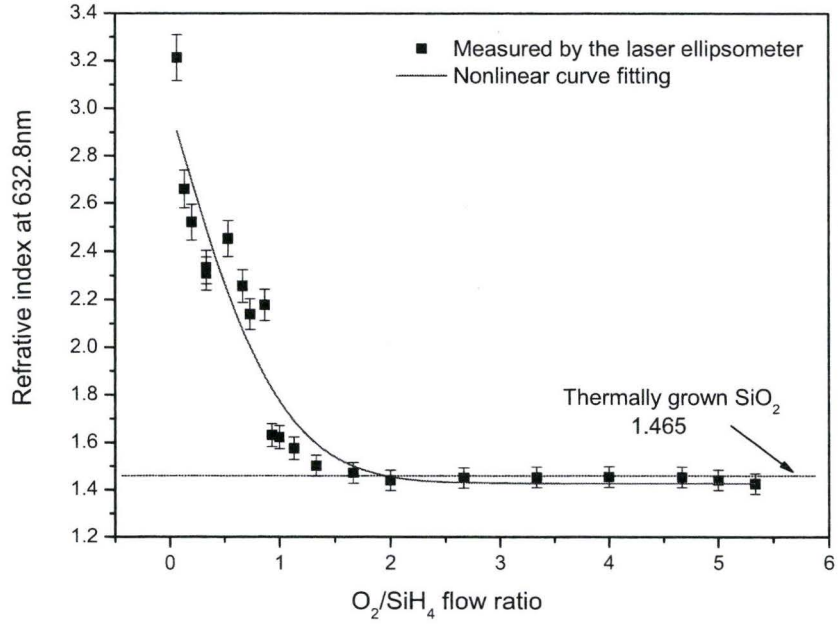

Figure 3.8 Refractive index of films fabricated in the ICP-CVD system measured at 632.8nm as a function of the oxygen to silane flow ratio.

The most significant factor determining the refractive index of thin films fabricated in the ICP-CVD system is the oxygen to silane gas flow ratio. Figure 3.8 shows the refractive index of the grown films as a function of the oxygen to silane flow ratio. These samples are grown with the silicon precursor, i.e., a mixture of 30% SiH_4 in argon, kept at a constant flow rate of 15.0 sccm, and the flow of mixture of 10% O_2 in

argon varied from 1.0 to 80.0 sccm. The mixture of 10% oxygen in argon is used for a fine control of the oxygen flow rate by possibly 0.1 sccm, which is critical when growing a silicon oxide with little oxygen for the higher refractive indices. From Figure 3.8, we can see that when the O_2/SiH_4 ratio is beyond 2, the refractive index remains almost constant at 1.45. This value is a little lower than the 1.465 of thermally grown SiO_2 due to hydrogen incorporated during deposition, which is common in thin films produced by CVD systems, especially at low temperatures. As the O_2/SiH_4 flow ratio decreases from 2, the refractive index increases as the silicon content is getting richer than that in the stoichiometric film, and it will eventually become an amorphous silicon film, as the O_2/SiH_4 flow ratio goes to zero.

In order to obtain a film with a larger refractive index, we need to use smaller O_2/SiH_4 flow ratios, while the oxygen needs to be maintained at a controllable and stable flow. The low refractive index material can be one of the films grown with an O_2/SiH_4 ratio >2. Although only two materials with high and low refractive index are needed to design a coating, a material with a medium refractive index will give some manufacture flexibility.

As mentioned earlier, removal of thin layers with physical thickness less than 10 nm will not cause noticeable degradation of the merit function value, while removal of a relatively thick layer will greatly degrade the merit function value. In a design which contains a layer not thick enough for monitored fabrication under the in-situ ellipsometry but not thin enough for a safe removal, we can replace that layer with a lower refractive index material, illustrated in Figure 3.9, and it will not cause a noticeable degradation of

the merit function value. The threshold thickness for a precise in-situ spectroscopic ellipsometric measurement will be discussed later.

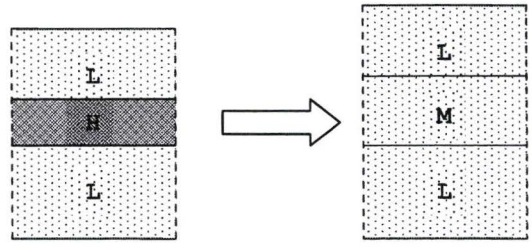

Figure 3.9 Replacing a high refractive index layer with a medium refractive index layer having the same optical thickness. H, M and L are the materials with high, medium and low refractive index.

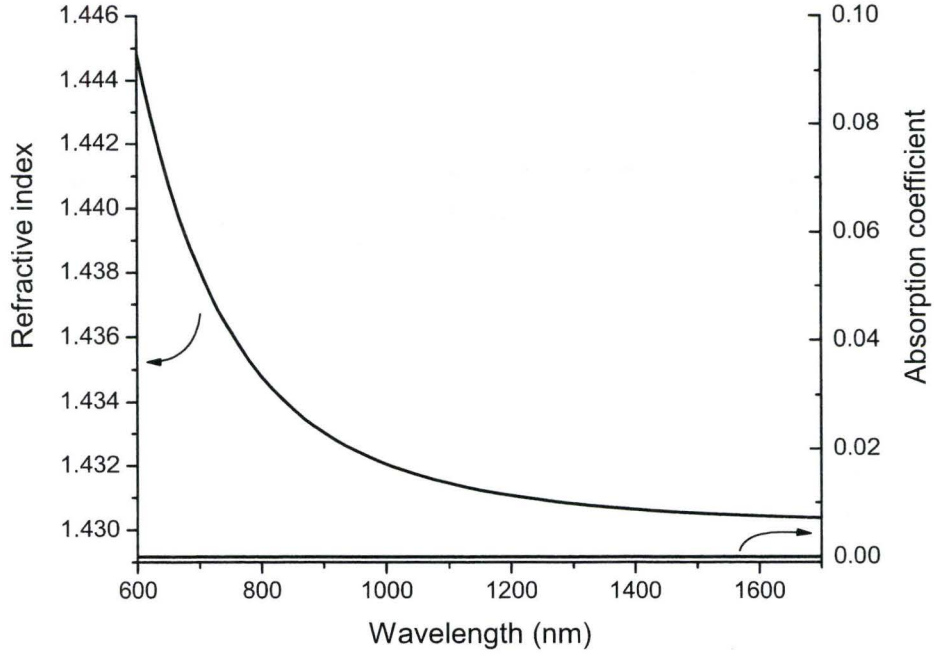

Figure 3.10 Refractive index and absorption coefficient of SiO_x_140 versus wavelength. The absorption coefficient remains zero in the wavelength range of interest.

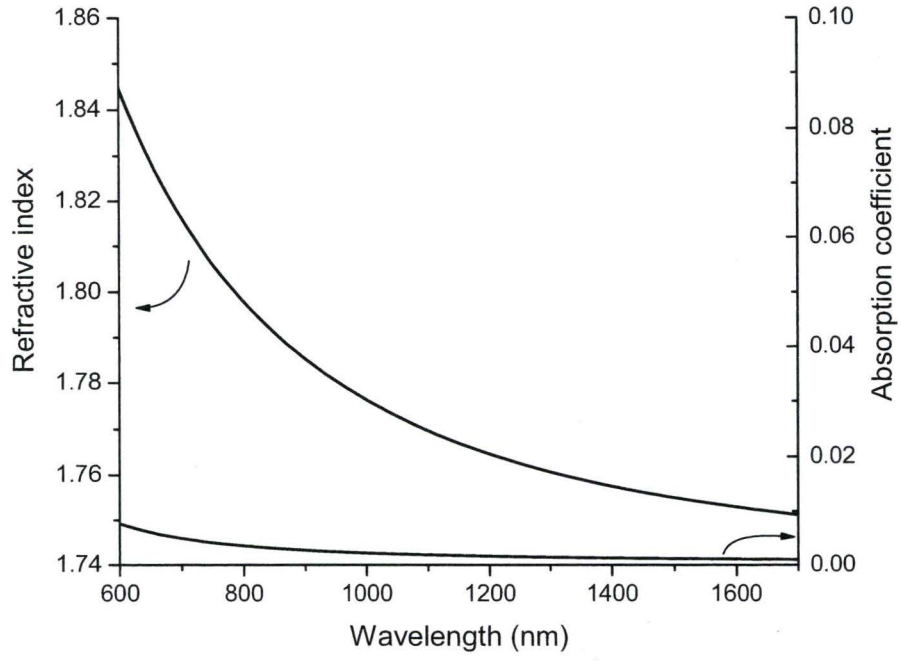

Figure 3.11 Refractive index and absorption coefficient of SiO_x_180 versus wavelength.

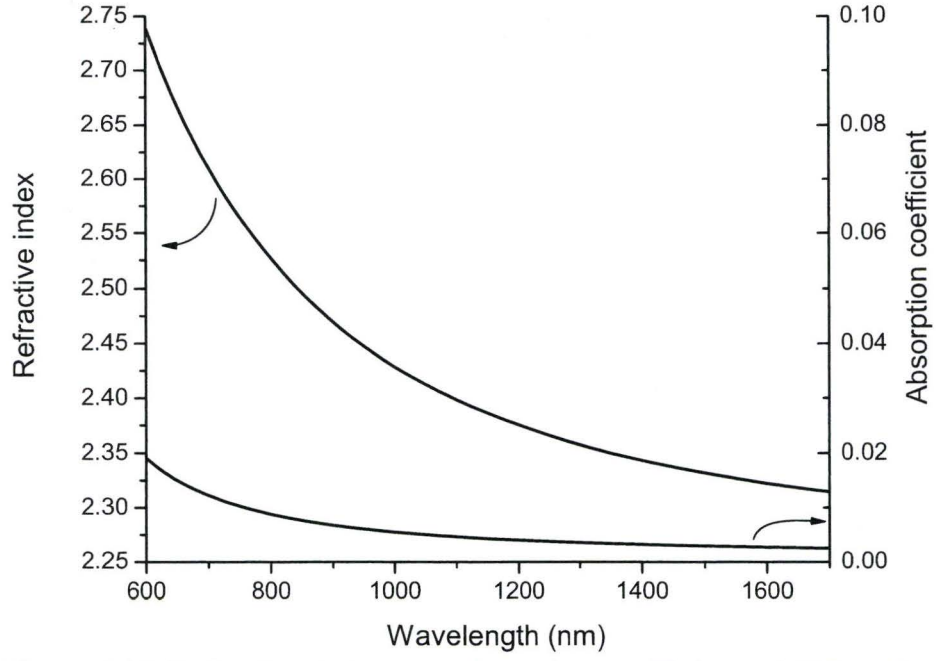

Figure 3.12 Refractive index and absorption coefficient of SiO_x_240 versus wavelength.

Three silicon oxides with low, medium and high refractive indices were chosen, labeled as SiO_x_140, SiO_x_180 and SiO_x_240 since their refractive indices at the wavelength of 1550 nm are close to 1.4, 1.8 and 2.4. Figures 3.10, 3.11 and 3.12 show the refractive index and absorption coefficient of these three materials as a function of wavelength, measured by a Woollam M-2000 spectroscopic ellipsometer with an uncertainty of 5%.

Although dielectric interference coatings are usually designed for and deposited on a large surface to function as optical filters, they can be also applied to a waveguide type surface, e.g. a laser facet. The material structure of the AMQW lasers was displayed in Table 2.1. To make a laser device, some processing is applied to the laser material structure such as etching to form a ridge waveguide to guide and confine the light, making metal contacts at the top and bottom for current injection and heat dissipation, cleaving the laser at specified cavity length, etc.. The schematic diagram of a ridge waveguide AMQW laser device is displayed in Figure 3.13.

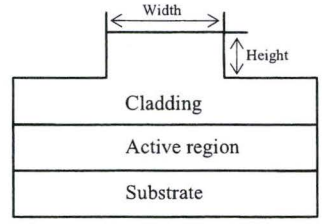

Figure 3.13 Schematic diagram of a ridge waveguide AMQW laser device.

The height of the ridge is designed for 1.5 μm and the width varies from 3 to 6 μm for different confinement effects. The active region includes the entire quantum well and barrier layers. The cladding and substrate have a lower refractive index than the active

region to confine the light. Each of the cladding, active region and substrate includes a few layers of InP and/or $In_{1-x}Ga_xAs_yP_{1-y}$ with different concentrations of gallium and arsenic. The refractive index of each $In_{1-x}Ga_xAs_yP_{1-y}$ is calculated according to its composition by the method discussed in Ref. [63]. The effective indices of the active region and cladding are calculated separately through the slab waveguide analysis [64].

It is very difficult to achieve the exact solution of electric and magnetic fields for light propagating through a 3-D waveguide. One of the common approaches, known as the effective index method, has been applied to the analysis of diode lasers [65-66] and is used to find the propagation constant of the ridge waveguide of the AMQW laser. The method proceeds in three steps (Figure 3.14):

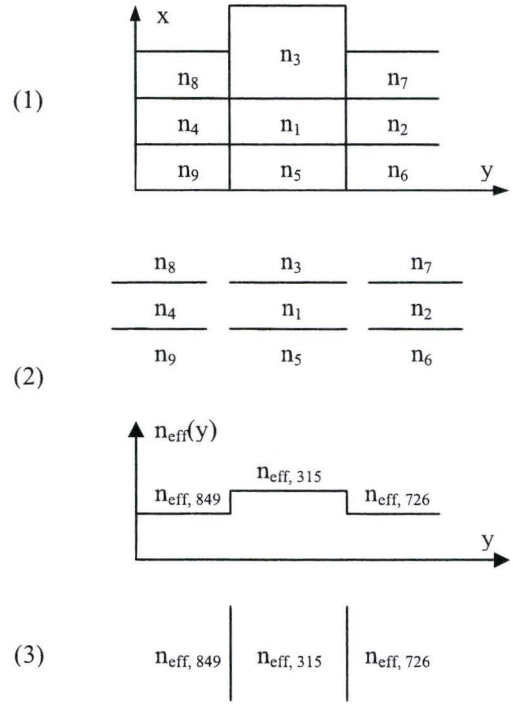

Figure 3.14 Schematic illustration of the effective index method.

1. The ridge waveguide is divided into 9 segments. n_1 to n_9 are the refractive indices of the materials of the segments. 4, 1 and 2 are the active region; 8, 3 and 7 are the cladding; 9, 5 and 6 are the substrate.
2. The slab waveguide problem is solved at each fixed y to obtain an effective index profile $n_{eff}(y)$. $n_{eff,\,849}$ is calculated from n_8, n_4 and n_9; $n_{eff,\,315}$ is calculated from n_3, n_1 and n_5 ; $n_{eff,\,726}$ is calculated from n_7, n_2 and n_6.
3. The slab waveguide problem is solved again using the effective index $n_{eff,\,849}$, $n_{eff,\,315}$ and $n_{eff,\,726}$. Thereby the effective index of the ridge waveguide is obtained which is then used as the refractive index of the substrate when designing the coating.

3.4.3 Gain flattening coatings for the AMQW laser

The gain flattening coating was designed with the help of a program written by myself for inserting the needle variation layer and with the commercial design software TFCalc. Since the total thickness of layers required by the complexity of the target reflectance (Figure 2.8) are beyond manufacturability by the ICP-CVD system, some high reflectance around the edges is sacrificed for an obtainable design.

After depositing 6 layers, the laser bar holder will have to be taken out of the chamber for replacing the witness sample. The coating of 18 layers is found sophisticated enough to have the designed reflectance close to the target reflection with less than 5% average deviation. For a multi-layer structure as the one shown in Table 3.1, the reflectance is calculated and displayed in Figure 3.15 along with the target reflectance curve. The total thickness of the multi-layer structure is 2952 nm and the numbering of

the layers is in the order of deposition, i.e., layer 1 is deposited directly onto the laser facet.

Layer #	Thickness (nm) (±1%)	Material
1	191	SiO_x_140
2	111	SiO_x_240
3	222	SiO_x_140
4	106	SiO_x_240
5	171	SiO_x_140
6	101	SiO_x_240
7	228	SiO_x_140
8	128	SiO_x_240
9	249	SiO_x_140
10	131	SiO_x_240
11	247	SiO_x_140
12	125	SiO_x_240
13	222	SiO_x_140
14	106	SiO_x_240
15	201	SiO_x_140
16	110	SiO_x_240
17	201	SiO_x_140
18	94	SiO_x_240

Table 3.1 Designed multi-layer structure for the gain flattening coating.

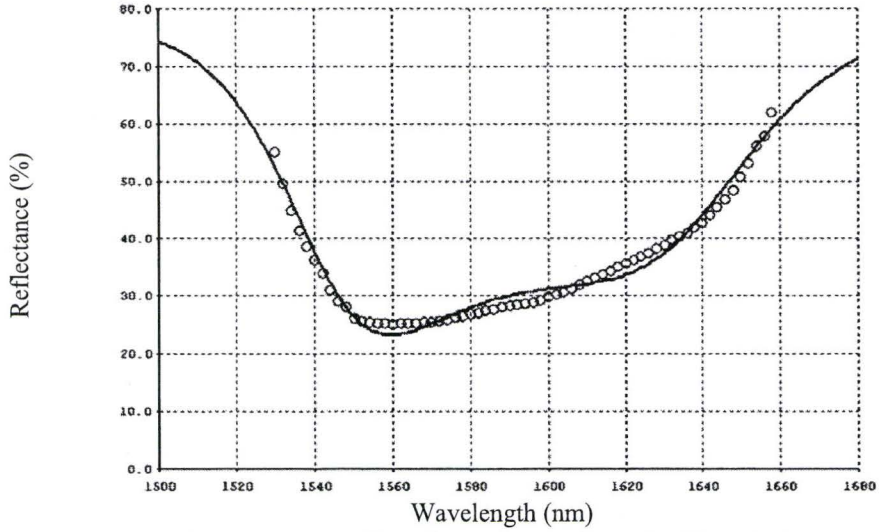

Figure 3.15 Reflectance as a function of wavelength. The circle represents the target and the solid line is the calculated reflectance of the multi-layer structure in Table 3.1.

Chapter 4

Fabrication of the gain flattening coatings

4.1 ICP-CVD system

All the coatings were fabricated in the inductively coupled plasma (ICP) enhanced chemical vapor deposition (CVD) system at McMaster University. The schematic diagram of the system is shown in Figure 4.1.

The main component of the ICP-CVD system is a stainless steel ultra high vacuum (UHV) chamber where the deposition takes place. The vacuum in the main chamber is maintained by a diffusion pump and an cold trap cooled by liquid nitrogen to prevent the back streaming of pump oil. The main chamber is pumped down to a very low pressure ($\sim 10^{-8}$ Torr) at least an hour prior to deposition in order to minimize the contamination by other residual gas particles of the deposited coatings. Since the reactive species can lose energies by multiple collisions with gas atoms or other reactive species, a constant low pressure (a few mTorrs) is kept during the deposition to control the density of gas atoms and reactive species in order to maintain a certain amount of reactive species energy.

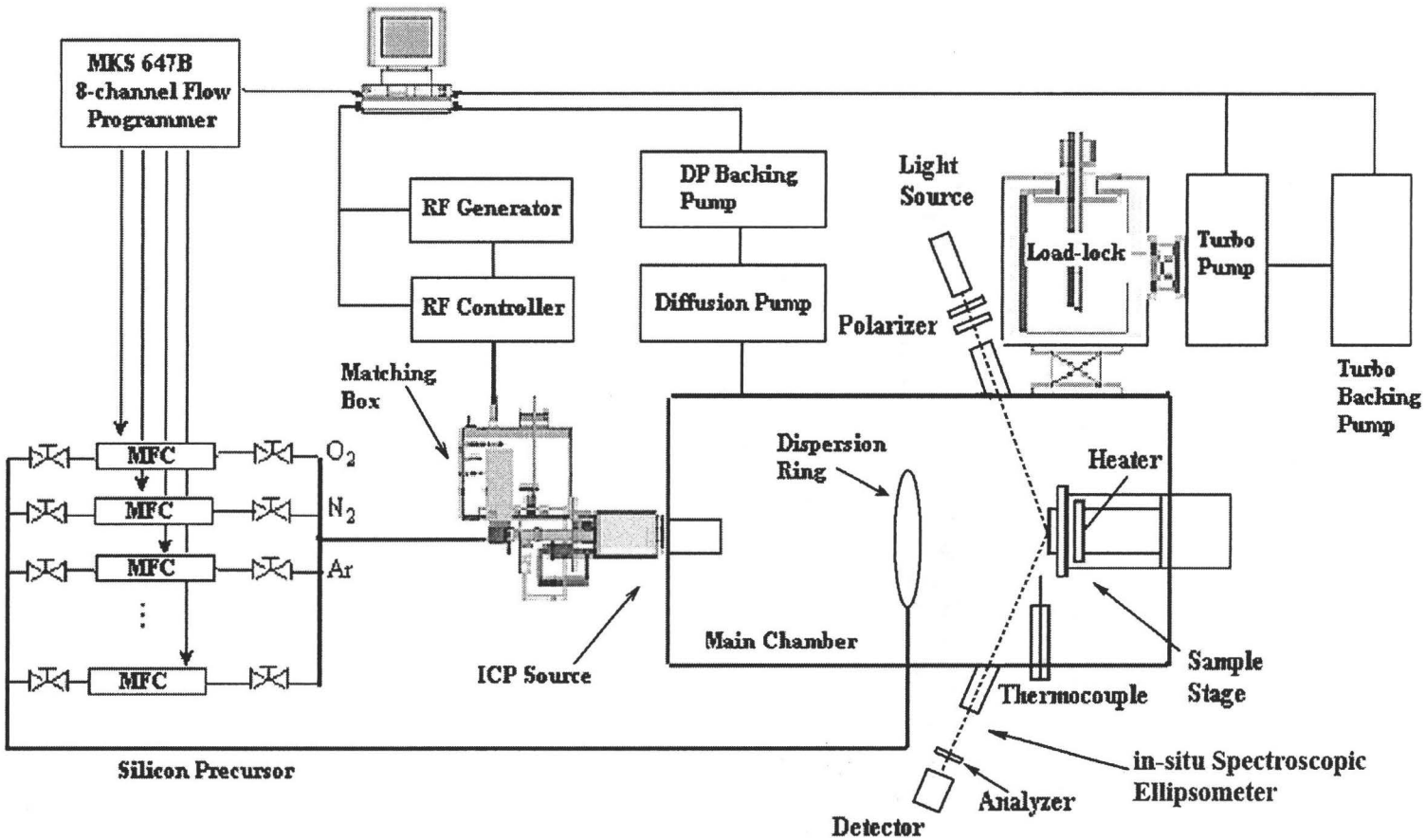

Figure 4.1 Schematic diagram of the ICP-CVD system.

Inserted from the right side into the main chamber is a sample stage which could travel up to 40 mm towards the left from the base position, i.e., close to the ICP source. A sample holder is clasped onto the top of the sample stage which is connected to a planar-coil resistive heater and can be heated up to 800 °C. The fact that the sample is standing vertically during deposition prevents the film from possible contamination by particles falling off the wall. The sample stage can be rotated with a constant speed (21 rpm) during deposition for good film uniformity. A retractable thermocouple installed on the side can be pushed forth to measure the substrate temperature. Also a shutter in front of the sample stage can be placed or displaced to stop or start deposition right away.

On top of the main chamber, a load lock is connected for loading and unloading samples and it is backed by a turbo pump. A single-axis manipulator with 20-inch stroke is mounted on top of the load-lock to allow the sample to travel from the load-lock to the main chamber. When loading samples to the load lock, the valve between the load lock and the main chamber is closed. Then the load lock is sealed and pumped down. When the pressures on both sides equalize, the valve is opened and the sample is lowered to the main chamber from the load-lock. The procedure reverses for unloading the samples. In this way, the sample transfer time is greatly shortened and chamber contamination is reduced to minimum after each transfer.

The ICP source is sitting on the left side of the main chamber. A power supply generates a 13.56 MHz radio frequency (RF) with the power range of 0~3000 W inside a shield which protects the surrounding equipment from the high RF field. A spiral RF coil wraps around a tube called the plasma chamber where the plasma is excited. The driving

current I_{RF} in the coil generates a magnetic field B_{RF} parallel to the plasma chamber axis (see Figure 4.2).

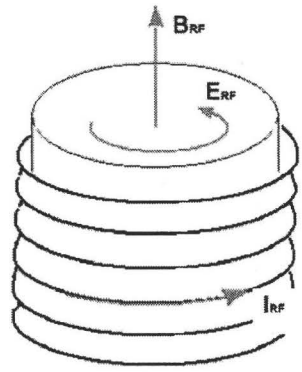

Figure 4.2 Schematic of the RF magnetic field and the induced electric field in an ICP source.

When the plasma gases, i.e., O_2, N_2 or Ar, are introduced respectively or simultaneously to the plasma chamber, a plasma is achieved after the applied RF power exceeds the ignition threshold. There is a ceramic lid covering the plasma chamber. The small apertures on that ceramic lid allow the plasma to flow into the main chamber. By exchanging the ceramic lid with different aperture patterns, we can define the plasma flux and more importantly focus the plasma beam to a certain position for optimum uniformity of thin film deposition. The matching box on the rear end of the ICP source houses a rotatory capacitor which tunes the reflected power to a minimum either manually or automatically.

Inside the main chamber, a circular dispersion ring is placed between the ICP source and the sample stage (see Figure 4.1). The precursor gas, silane, is introduced through the holes on the dispersion ring. When the reactive species with high energies in

the plasma meet the silane molecules, a series of elastic and inelastic collisions takes place, which gives rise to reactions and depositions on the substrate surface. The dispersion ring is placed 3.5 inches away from the plasma source and the holes on the dispersion ring are 1.75 inches away from the sample stage. This arrangement ensures that the deposition stays far enough away from the plasma region for a deposition with minimum plasma damage to the substrate.

The gas delivery system makes up the rest of the ICP-CVD system. An O_2 mixture (10% O_2 in Ar), N_2 mixture (10% N_2 in Ar), silane mixture (30% SiH_4 in Ar), pure Ar (99.999%), pure O_2 (99.99%), and pure N_2 (99.999%) are used for the deposition of amorphous silicon, silicon nitride, silicon oxide, and silicon oxynitride. The mass flow controller consisting of a shutoff valve and sensor measures and controls the mass flow rate of the gas with an accuracy of $\pm 1\%$ of the full scale reading. While the rest of the gases are converged and introduced to the plasma chamber, the silane is fed separately to the dispersion ring. Since silane is an extremely flammable and toxic gas, special precautionary measures have been taken in handling and transferring. An auto-purge dual source controller automatically controls feeding and cutting of the silane gas with the necessary purging process enforced every time the silane gas line is accessed.

Mounted on either side of the main chamber are the polarized light source and the detector-analyzer assembly of the Woollam M-44 in-situ spectroscopic ellipsometer. It provides real-time monitoring of the thickness and refractive index of deposited films and will be discussed later.

4.2 Deposition mechanism

In the ICP-CVD system, energy from the RF source is coupled into the plasma gases to generate a number of reactive species. Collisions among these species give rise to reactions and eventually cause the depositions on substrates. In a plasma, there are electrons and various types of ions, neutral atoms and molecules. These particles usually have two types of energy: kinetic energy due to the motion and internal or potential energy which may be in the form of electronic excitation or ionization. Collisions among all possible pair permutations could happen, which are mainly divided into elastic and inelastic types. In the elastic collisions, only minimal kinetic energy transfer occurs. For plasma processing, the elastic collisions play a less important role in reactant dissociation [67]. All other types of collisions are inelastic including collisions involving electrons, ion-neutral collisions, and metastable collisions.

The detailed reactions occurring during the plasma enhanced deposition are complex, and have been discussed by various researchers [68-71]. When the plasma is first ignited, the RF electric field is coupled into the reactant gases by the kinetic energy of a few free electrons. These electrons gain energy rapidly from the electric field and lose energy slowly through elastic collisions. The high energy electrons are capable of inelastic collisions which cause the reactant gas molecules to dissociate and/or ionize, producing secondary electrons by various electron-impact reactions until the steady-state plasma is sustained. When the flux of these reactive species reaches the substrate surface by diffusion, various chemical reactions can take place. The reactions on the substrate

surface include two aspects: the incorporation of deposition precursors, and the re-emission back to the gas phase of the reactive species deposited on the substrate.

To deposit a silicon oxide film, O_2/Ar and SiH_4 are used. Various gas flow ratios of O_2/Ar to SiH_4 produce silicon oxides with different oxygen contents, which lead to a range of refractive indices of the deposited films (see Figure 3.8). The O_2/Ar mixture excited by the inductively coupled plasma is decomposed into active species, which include oxygen atoms, excited Ar atoms (Ar^*), electrons, and some oxygen and argon ions (O_2^+, O^+, Ar^+). The dominant ions that exist in the mixture of Ar/O_2 in the plasma zone are O_2^+, which is produced primarily by electron impact and secondarily by Penning ionization by Ar^* [72]. O^+ and Ar^+ are produced in approximately the same density, with the former primarily being produced by charge exchange from Ar^+ to O_2. Possible processes are suggested as below [69,72]:

$$Ar^* + O_2 \rightarrow O_2^+ + Ar + e$$

$$Ar^+ + O_2 \rightarrow O_2^+ + Ar \rightarrow O^+ + O + Ar$$

Then, these excited species diffuse from the plasma chamber through the patterned aperture into the main chamber where the various species are mixed with the silane gas introduced through the dispersion ring. The mixing leads to the formation of gas phase precursors that contain the structral building blocks of the deposited film. Reactions of oxygen atoms with SiH_4 proceed by a series of H abstraction or elimination [71].

$$O + SiH_4 \rightarrow SiH_3 + OH$$

$$O + SiH_3 \rightarrow SiH_2O + H$$

$$OH + SiH_3 \rightarrow SiH_2O + H_2$$

$$O + SiH_2O \rightarrow HSiO + OH$$

$$O + HSiO \rightarrow SiO + OH$$

$$SiO + O \rightarrow SiO_2 + O$$

The careful combination of the RF power and the deposition pressure is essential to the deposition of silicon oxides. The flux of SiH_4 to the substrate decreases with increasing power density as it is depleted by reactions with the larger density of oxygen atoms. Species whose production require many oxidation steps, such as $HSiO_2$, SiO_2, and SiO, increase exponentially with power, however the deposition rate saturates with increasing power [73]. The diffusion rates of species are much faster and the gas-phase reaction rates are lower in plasmas of low deposition pressure (a few mTorrs) than at high deposition pressures (tens to hundreds of mTorrs) [74]. Therefore, under low deposition pressures, ion-induced chemical reactions make a higher contribution to the deposition. It is believed that ions impinging on the film surface play major roles in the film deposition. They enhance adsorption and desorption rates of neutral radical species through bond breaking and forming in the top atomic layers of the film. They also act as a source of silicon and oxygen, directly contributing to the deposition of silicon oxides.

4.3 Ellipsometric measurements

A successful optical interference coating requires a precise control of thickness and refractive index of each layer during deposition. In the ICP-CVD system, a Woollam

M-44 in-situ spectroscopic ellipsometer operating at wavelengths from 600 nm to 1100 nm provides real-time monitoring of the thickness and refractive index of the deposited films. A Philips PZ2000 laser ellipsometer at 632.8 nm at McMaster and a Woollam M-2000 spectroscopic ellipsometer with the working range of 245 nm to 1700 nm at the Ecole Polytechnique at Montréal were used for ex-situ measurement and calibration.

Ellipsometry is a versatile optical technique which has been used for over a hundred years to derive information about thin film properties, such as optical constants (n, k), layer thickness, surface and interfacial roughness, composition and optical anisotropy. The technique is characterized by accuracy, non-destructivity and high reproducibility. Ellipsometry relies on the fact that the reflection at an interface depends on the polarization of the light, while the transmission of light through the layer changes the phase of the incoming wave depending on the refractive index of the material. By analyzing the change of both the amplitude and phase of a polarized light beam reflected from the sample surface, we can extract the sample surface properties (i.e., thickness and refractive index) with appropriate model calculation.

All ellipsometer arrangements contain a light source and a detector. The typical setup of a null ellipsometer is shown in Figure 4.3. The polarizer provides a state of polarization that can be varied from linearly polarized to elliptically polarized to circularly polarized light by changing the angle of the polarizer. The beam is reflected off the layer of interest and then analyzed.

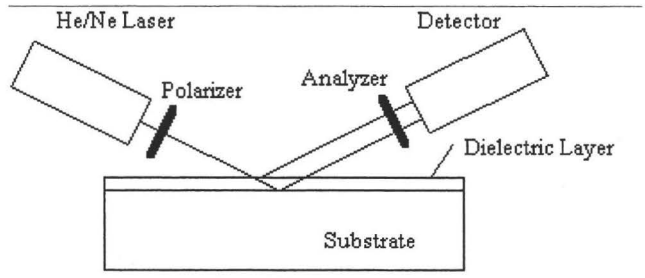

Figure 4.3 Schematic diagram of a typical null ellipsometer.

The angle of the polarizer and analyzer can be changed until a minimal signal is detected. This minimum signal is detected if the light reflected by the sample is linearly polarized, while the analyzer is set so that only light with a polarization that is perpendicular to the incoming polarization is allowed to pass. The angle of the analyzer is therefore related to the direction of polarization of the reflected light if the null condition is satisfied. In order to obtain linearly polarized light after reflection, the polarizer must provide an optical retardation between the two incoming polarizations that exactly compensates for the optical retardation caused by the polarization dependent reflections at each dielectric interface. Since the amplitude of both polarizations is set to be equal, the ratio of the amplitudes after reflection equals the tangent of the angle of the analyzer with respect to the normal.

The calculation of the expected angles of the polarizer and analyzer corresponding to the null condition starts with the Fresnel reflection coefficients at each of the dielectric interfaces for each polarization [75].

$$r_{01,TE} = \frac{n_0 \cos\phi_0 - n_1 \cos\phi_1}{n_0 \cos\phi_0 + n_1 \cos\phi_1} \tag{4.1}$$

$$r_{01,TM} = \frac{n_0 \cos\phi_1 - n_1 \cos\phi_0}{n_0 \cos\phi_1 + n_1 \cos\phi_0} \tag{4.2}$$

$$r_{12,TE} = \frac{n_1 \cos\phi_1 - n_2 \cos\phi_2}{n_1 \cos\phi_1 + n_2 \cos\phi_2} \tag{4.3}$$

$$r_{12,TM} = \frac{n_1 \cos\phi_2 - n_2 \cos\phi_1}{n_1 \cos\phi_2 + n_2 \cos\phi_1} \tag{4.4}$$

with $n_0 \sin\phi_0 = n_1 \sin\phi_1 = n_2 \sin\phi_2$, where the subscripts, 0, 1 and 2 refer to air, the thin layer and the substrate, and ϕ is the angle of the transmitted wave with respect to the normal to the interface as shown in Figure 4.4.

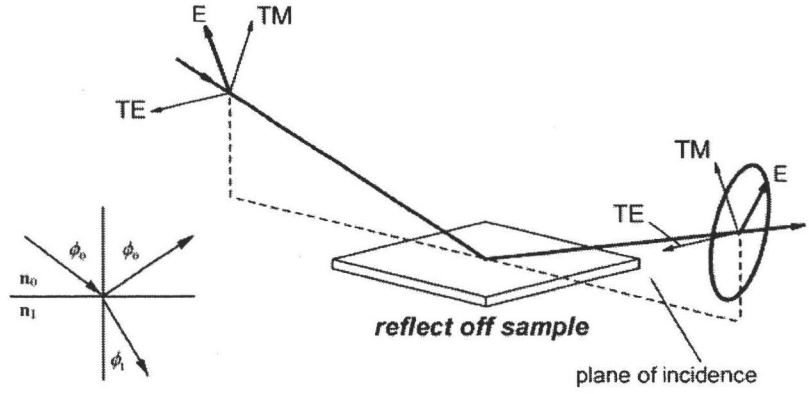

Figure 4.4 Geometry of an ellipsometric experiment, showing the TE and TM polarizations.

The two dielectric interfaces yield a combined reflection coefficient that can be obtained using the Fabry-Perot equations:

$$r_{TE} = \frac{r_{01,TE} + r_{12,TE} e^{-i\delta}}{1 + r_{01,TE} r_{12,TE} e^{-i\delta}} \tag{4.5}$$

$$r_{TM} = \frac{r_{01,TM} + r_{12,TM} e^{-i\delta}}{1 + r_{01,TM} r_{12,TM} e^{-i\delta}} \tag{4.6}$$

Where $\delta = \frac{4\pi n_1 d_1 \cos\phi_1}{\lambda}$.

Inserting equations (4.1, 4.2, 4.3 and 4.4) into equations (4.5 and 4.6) yields the expressions for r_{TE} and r_{TM}, that is the reflection coefficients of the dielectric stack for each polarization. The ratio of the two reflection coefficients can be split into an amplitude and phase factor, thereby defining the ellipsometric parameters Ψ and Δ:

$$\frac{r_{TM}}{r_{TE}} = \tan\psi \cdot e^{i\Delta} \tag{4.7}$$

The minimal signal is obtained when polarizations incident on the analyzer are in phase. This can be obtained for two different positions of the polarizer. In principle either one of them can be measured. In practice both values are measured to eliminate any possible misalignment of the instrument thereby yielding a more accurate result.

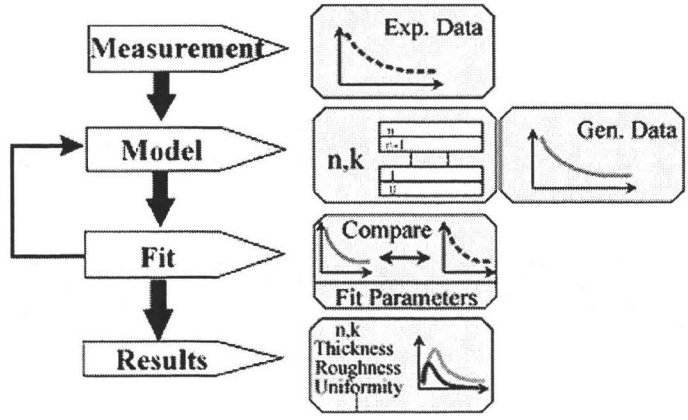

Figure 4.5 Flow chart of data analysis process in spectroscopic ellipsometry. [77]

Many samples may be characterized by ellipsometric measurements at a single wavelength, but spectroscopic ellipsometry measurements provide the ability to acquire data and therefore extract the sample properties in spectral regions of interest. Combined

with a variable angle of incidence, spectroscopic ellipsometry allows users to acquire large amounts of data from one given sample to optimize the determination of sample properties. Shown in Figure 4.5, the procedures for obtaining the sample parameters (thickness, refractive index, roughness, uniformity, etc) [77] are:

1. Acquiring data (Ψ and Δ) versus wavelength, and angle of incidence, if applicable.
2. Building an optical model that describes the sample structure. Since the samples are silicon oxide films of different oxygen contents, the commonly used model is the Cauchy dispersion model, i.e. the refractive index (the real part) is defined as:

$$n(\lambda) = A + \frac{B}{\lambda^2} + \frac{C}{\lambda^4} \tag{4.8}$$

The extinction coefficient (the imaginary part) is defined as:

$$k(\lambda) = \alpha \exp\left(\beta \cdot 12400 \cdot \left(\frac{1}{\lambda} - \frac{1}{\gamma}\right)\right) \tag{4.9}$$

The Cauchy dispersion model is one of the best models for the refractive index in transparent regions, since it offers all the flexibility needed. λ being the wavelength, there are six parameters, i.e., the coefficients A, B, C, amplitude α, exponent factor β and band edge γ to be fit. When building an optical model for a sample, it is important to account for all the layers in the sample. Sometimes it is highly recommended to even include roughness layers and intermixing layers for better rendition of the real structure to achieve a reasonably good fit.

3. Generating the theoretical data from the optical model that corresponds to the experimental data.

4. Comparing generated data to experimental data. Unknown parameters in the optical model, such as film thickness or optical constants or both, are varied to try and produce a "best fit" to experimental data. Regression algorithms are used to vary unknown parameters and minimize the difference between the generated and experimental data. Physical parameters of the sample such as film thickness, optical constants, composition and surface roughness are obtained once a good "fit" to the experimental data is achieved.

The same procedure applies to the in-situ spectroscopic ellipsometer. During deposition, the spectroscopic ellipsometer repeats these procedures in a designated time interval of typically 8 seconds. A growth rate is estimated to control the film thickness and stop the deposition immediately whenever the targeted thickness is achieved.

In practice, at the early stage of growth, the deposition process involves nucleation and networking steps, which causes the optical properties of the grown film to evolve. Therefore, the refractive index of the deposited material fitted by the in-situ spectroscopic ellipsometer is varying as the thickness increases until it stabilizes beyond a certain thickness. This certain thickness is considered as the threshold thickness for a precise in-situ spectroscopic ellipsometric measurement. The threshold thickness depends on the configuration and computation algorithm of the ellipsometer. It also varies for silicon oxides with different oxygen contents and 30 to 40 nm is a reasonable empirical estimation.

The advantage of a spectroscopic ellipsometer over a single wavelength ellipsometer is the huge amount of data collected over the entire wavelength range, which

allows a fit for a large number of unknown parameters. This is the essence of the in-situ spectroscopic ellipsometer for monitoring deposition of multi-layer structures. However, when the unknown parameters reach a large number, the collected data are not enough to give a reasonable fit with precision, because the number of unknown parameters, i.e., the thickness and refractive index of each layer to be fit is limited by the number of wavelengths where the Ψ and Δ values are collected. In practice, after 6 layers of SiO_x thin films are deposited on the substrate under the monitoring, the in-situ spectroscopic ellipsometer is no longer able to give a precise measurement of the refractive index and thickness of the seventh layer being deposited. Figures 4.6 and 4.7 show the fitting curves of Ψ and Δ of 6 and 7 layers. The calculated Ψ and Δ values of 6 layers fit well with the collected data, however, the deviation between the model calculation and collected data for 7 layers has caused the result of fitting no longer to be precise.

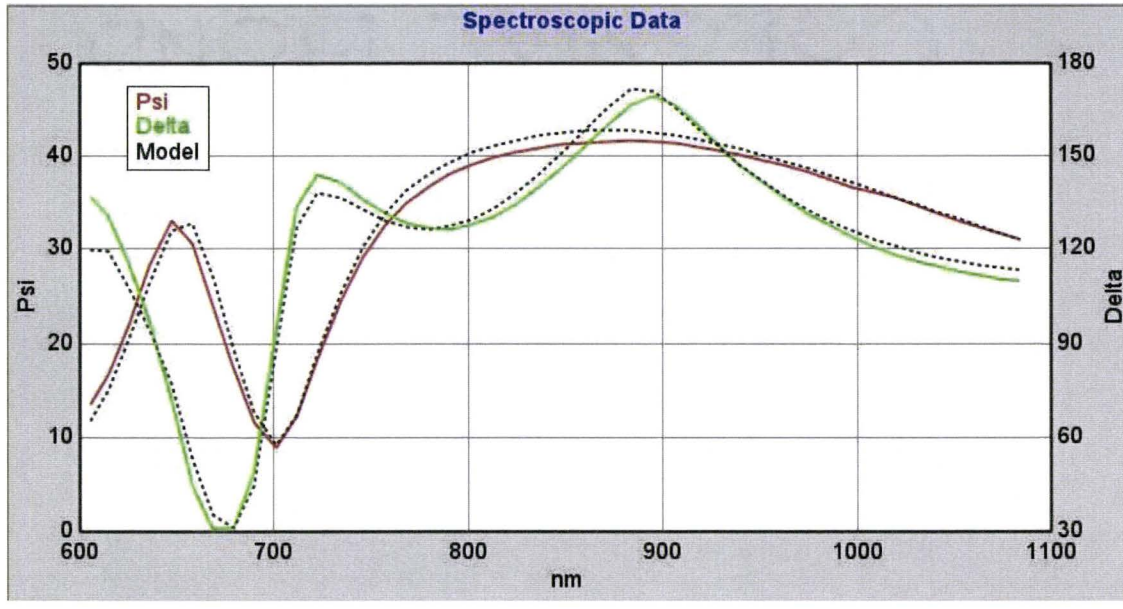

Figure 4.6 Ψ (Psi) and Δ (Delta) collected by the spectroscopic ellipsometer at different wavelengths, and the curve generated by model fitting the thickness and refractive index of 6 layers of thin SiO_x films.

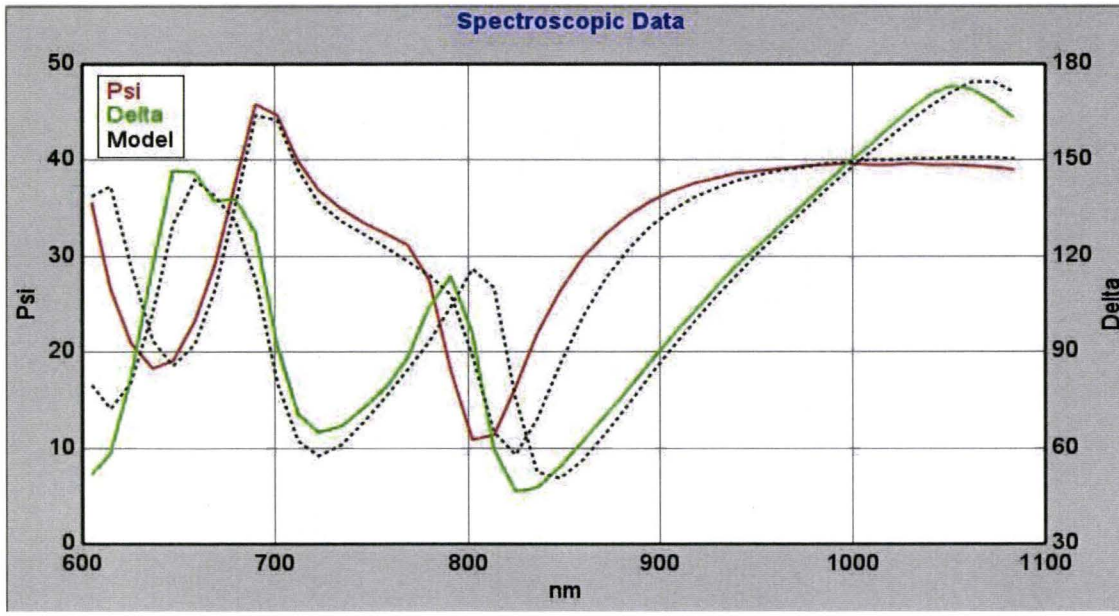

Figure 4.7 Ψ (Psi) and Δ (Delta) collected by the spectroscopic ellipsometer at different wavelengths, and the curve generated by model fitting the thickness and refractive index of 7 layers of thin SiO_x films.

4.4 The laser bar holder and its optimization

A laser bar holder was custom designed and fabricated to accommodate the laser bar during deposition. The laser bar is brittle. The area of the facet to be coated is usually about 150 μm × 7 mm and the cavity length of the laser is less than 1 mm. The laser bar holder has to be able to not only hold the bar tightly enough not to lose it during the loading-unloading procedure and rotation motion in deposition, but also not to break it after the holder is heated at certain temperatures, which causes thermal expansion.

Figure 4.8 is a picture of the laser bar holder. It is made of stainless steel which conducts the heat well and sustains little deformation after the heating cycles. On the surface a witness sample of a quarter of a 2-inch silicon wafer can be installed in the middle for monitoring of the refractive index and thickness. The rest of the space

accommodates three fixture modules, each of which can hold one laser bar. Figure 4.9 is the schematic diagram of the fixture module on the laser bar holder.

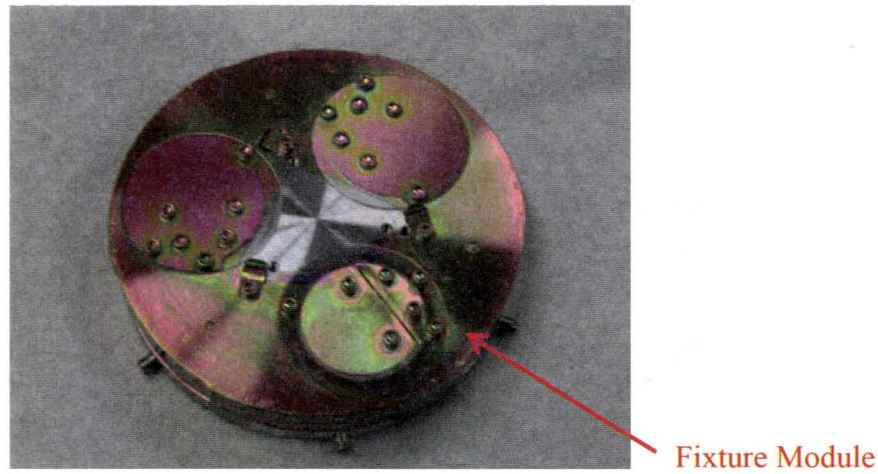

Figure 4.8 Laser bar holder.

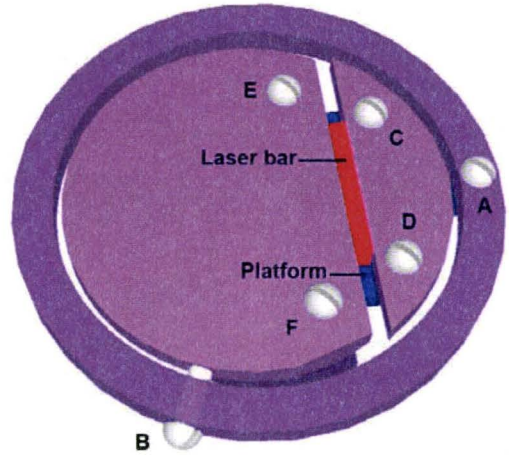

Figure 4.9 Schematic diagram of the fixture module.

The laser bar is placed on the platform, the height of which can be adjusted by screw A and the facet to be coated is facing up and obtruding just above the metal pieces that clamp the laser bar. The metal piece under screws C and D is fixed while the piece underneath E and F can be pushed closer or further by a spring loaded screw B. Screws E

and F can be loosened and fastened to align the edge of the metal piece underneath to be parallel to that of the laser bar for a stable and uniform grip.

Film uniformity is one of the most important properties of a practically useful coating. In order to have the possibility of obtaining uniform thickness of deposited films on a laser facet, the surface of the laser facet has to be placed at a position where a large area uniformity of deposition is achieved. This is determined by the fact that the plasma emerges from the patterned apertures and diffuses into the main chamber in a cone-like shape. Surface uniformity is usually defined as the standard deviation of the mean thickness of the deposited layer and expressed as:

$$Uniformity = \frac{\sqrt{\frac{1}{N-1}\sum_{i=1}^{N}\left(X_i - \overline{X}\right)^2}}{\overline{X}} \times 100\% \qquad (4.10)$$

where $\overline{X}$ is the mean thickness, X_i is the measured thickness at measuring point *i*, and N is the total number of measurements. In the ICP-CVD system, the thickness uniformity is subject to many factors, such as the substrate temperature, gas flow rates and ratios of O_2/SiH_4, RF power, the distance between the plasma source and the sample, and the aperture pattern [76]. Among these factors, the distance between the plasma source and the sample plays a crucial role in achieving uniform thickness. In the following example, silicon dioxide was grown twice with the same gas flow, plasma power, and substrate temperature but at different distances between the plasma source and the sample.

(a)

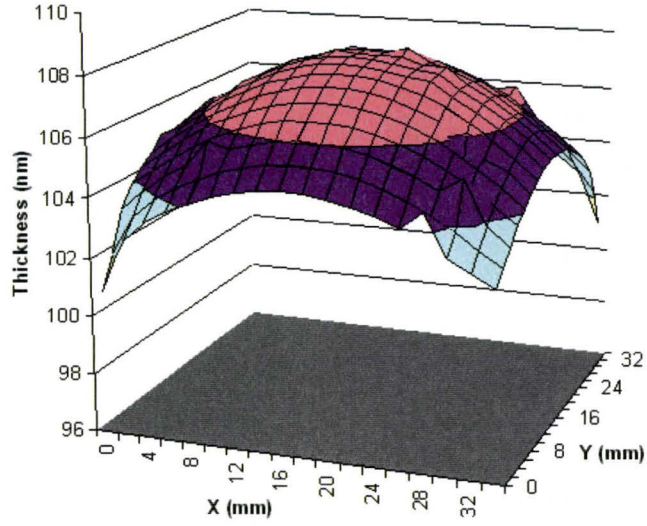

(b)

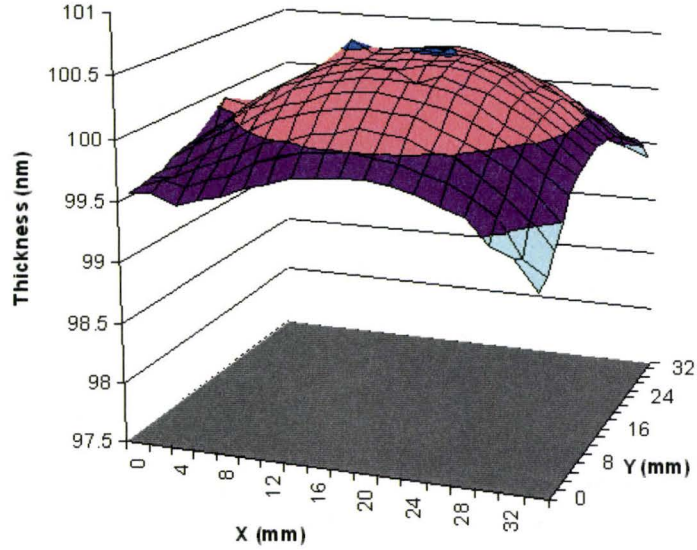

Figure 4.10 Raster scan of thickness of two SiO_2 samples grown under the same conditions but at different distances between plasma source and the sample: (a) 133mm (b) 235mm.

Figure 4.10 shows the raster scan of thickness in an area 34×34 mm^2 by the Philips PZ2000 laser ellipsometer. In (a) and (b), the distances from the source are 133 mm and 235 mm, respectively. Figure 4.10 (b) shows a much better thickness uniformity.

If one continues to increase the distance, however, a bowl-shaped depression will form in the middle, like a crater.

Even after the position where a good area uniformity of deposition is achieved has been found, uniform thickness of the deposited films on a laser facet is not necessarily obtained, as it can also be affected by the topological features of the laser bar holder. To carry out the experiment, a thin silicon wafer (~250 μm) was cleaved to obtain the specular facet and cut into small strips of 2 mm × 7 mm mimicking the size of a laser bar yet easier to handle for the ellipsometric measurement. After deposition of silicon oxide, a raster scan of thickness was made.

The so-called shadow effect is known as disadvantageous if the laser facet to be coated is placed below the level of the clamping metal pieces. Although the uniformity is not affected by how much the facet to be coated extends above the clamping metal pieces, it is preferred not to stick out the facet too much and expose most of both sides of the laser bar to the plasma, which causes the electrodes on the sides of the bar to be coated dielectrically. We try to keep the facet at the same level as the clamping metal pieces, and therefore the electrodes can be protected.

It was found that the height of the screws which fix the clamping metal piece has a substantial impact on the uniformity of thickness (see Figure 4.11), while the refractive index remains uniform. Figures 4.11, (a), (b) and (c) show the screw heads being ground down gradually; (d), (e) and (f) are the raster scans of the thickness of films deposited onto the silicon facet performed by the Philips PZ2000 laser ellipsometer after the adjustment was made.

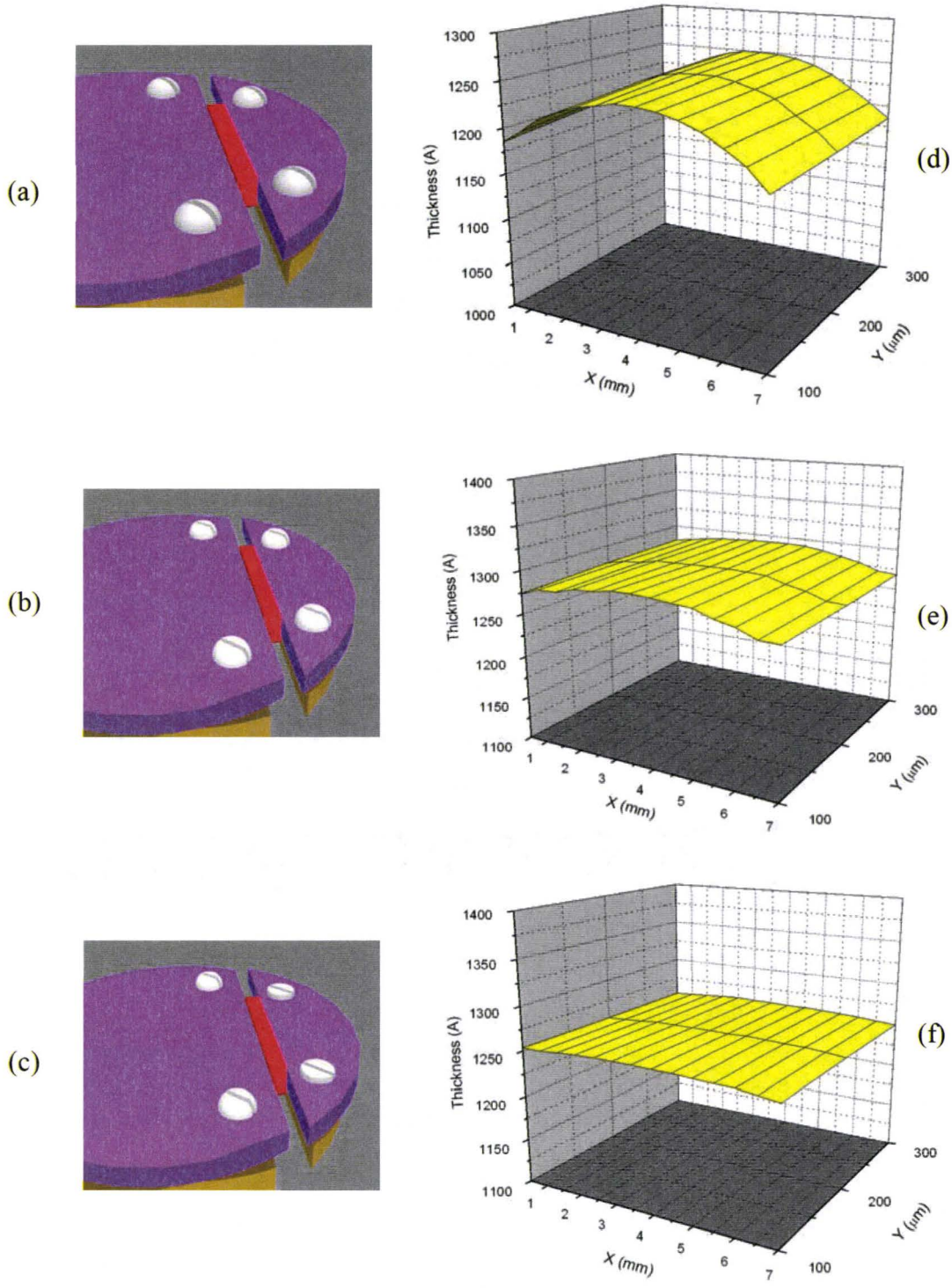

Figure 4.11 The height of the screws affects the uniformity of films deposited onto the silicon bars. (a), (b) and (c) show the screws being ground down gradually; (d), (e) and (f) are the raster scans of the corresponding deposition thicknesses.

The effect of these screws on the uniformity is estimated as follows: The electric field between the plasma and all surfaces in contact with the plasma, referred to as plasma sheath is generated by the fact that electrons have much higher thermal velocities than ions and are lost faster near objects. The electric field confines electrons and accelerates positive ions towards the object. If the surface of the object is flat, the electric field towards the object is uniformly distributed, producing an even growth rate across the surface. When the four screws around the bar extrude beyond a critical point, however, the change of the electric field distribution can cause uneven growth rates and affect the uniformity of thickness of the grown film.

4.5 Calibration of the laser bar holder

With the ability established of producing uniform films on a laser facet, one still needs to find the correlation between the deposited film on the bar and that on the witness sample, because the bar is so small that it is impossible to monitor the thickness and refractive index by the in-situ spectroscopic ellipsometric measurement which requires an area of at least 5 mm in radius to contain the beam spot. This is a crucial step to ensure a controllable growth of practically functioning coatings on the laser facet.

At the very beginning, it is natural to assume that the thickness and refractive index of the film on the laser bar should be roughly the same as that on the witness sample. A layer of silicon rich silicon oxide film was simultaneously deposited onto a scrap laser bar and a highly doped silicon wafer for the purpose of dissipating the charges during the subsequent scanning electron microscopy (SEM). Then the interface of the grown film and substrate was exposed for a high definition SEM investigation. Figure

4.12 shows the SEM images of the section of a silicon rich silicon oxide film on the silicon wafer and the laser bar. Note that the numbers on the images are generated by the SEM software which measures the distance of two given points on the image. In fact, with the resolution of around 10 nm, the SEM is by no means a precise measuring tool for the thickness we are interested in, but the reproducible results over a number of samples have convinced us that there is a substantial difference of the physical thickness between the film on the witness sample and that on the laser facet, and the former is thicker than the latter.

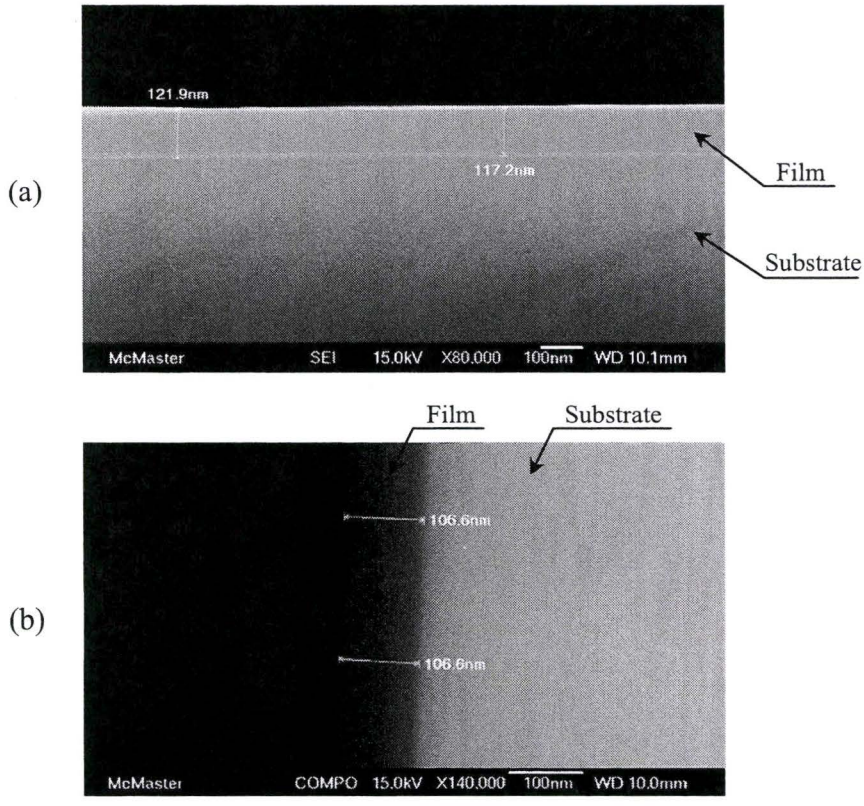

Figure 4.12 SEM images of the section of a silicon rich silicon oxide on (a) a highly doped silicon wafer and (b) a scrap laser bar. Thicknesses of the grown films are scaled. Scanning modes are different for the best visual effect.

In order to find the correlation between the deposited film on the bar and that on the witness sample, silicon oxides with different contents of silicon and various thicknesses were deposited. Again, a silicon wafer (~250 μm) was cleaved to get a specular facet and cut into small strips of 2 mm × 7 mm. After deposition, the refractive index and thickness of the film on the bar and witness sample were measured by the laser ellipsometer.

			SiO_x_140	SiO_x_180	SiO_x_240
Deposition pressure (mTorr)		(±1%)	2.7	1.8	2.4
Discharge power (W)		(±1%)	336	322	315
Reflected power (W)		(±1%)	36	22	15
Heating temperature (°C)		(±1%)	300	300	300
Sample temperature (°C)		(±1%)	120	120	120
Gas flow (sccm)	Ar	(±5%)	/	/	15
	O_2/Ar	(±5%)	30	10	1.2
	SiH_4	(±5%)	10	15	15

Table 4.1 Deposition conditions for the growth of silicon oxides SiO_x_140, SiO_x_180 and SiO_x_240.

Three silicon oxides with low, medium and high refractive indices were investigated. Table 4.1 shows the deposition condition for these three materials. As the thickness of the film on the witness sample measured by the Philips PZ2000 laser ellipsometer has been proved to be identical to that measured by the in-situ spectroscopic ellipsometer, we can now calibrate the in-situ measured thickness with the real grown thickness on the bar. It was found that the difference of the refractive index between the film on the witness sample and that on the bar was independent of thickness and usually around ±1% of the refractive index deposited.

(a)

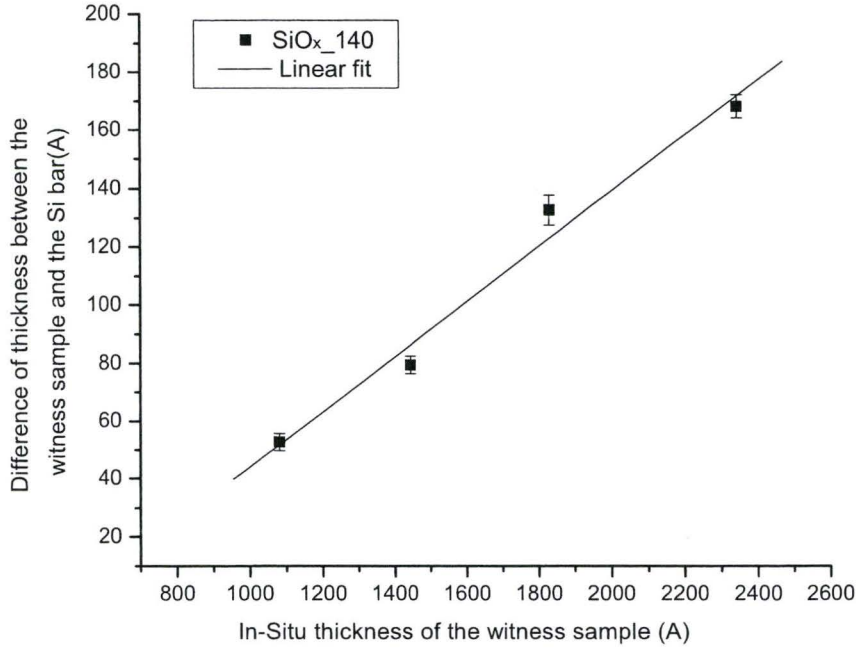
SiOx_140
Linear fit
Difference of thickness between the witness sample and the Si bar(A)
In-Situ thickness of the witness sample (A)
200
180
160
140
120
100
80
60
40
20
800
1000
1200
1400
1600
1800
2000
2200
2400
2600

(b)

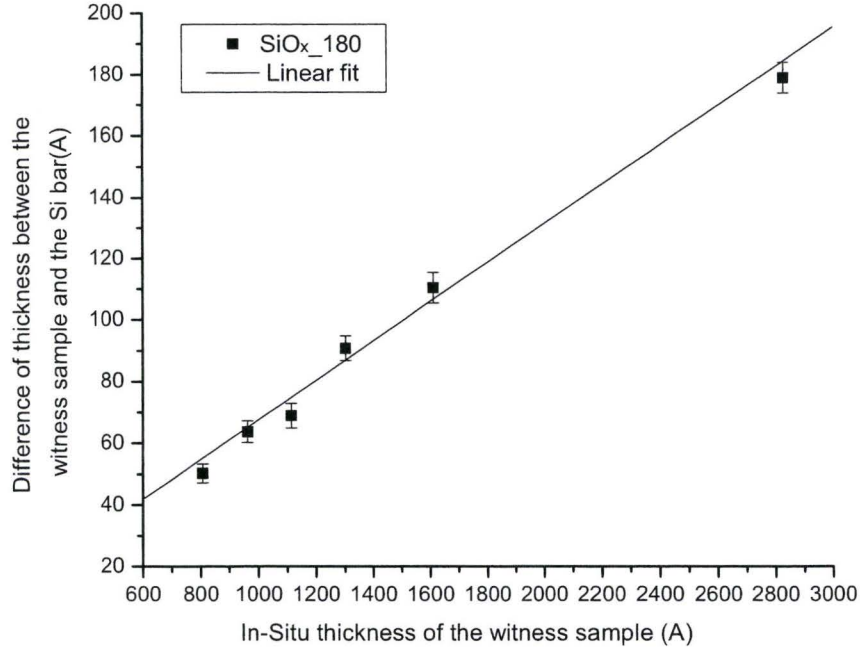
SiOx_180
Linear fit
Difference of thickness between the witness sample and the Si bar(A)
In-Situ thickness of the witness sample (A)
200
180
160
140
120
100
80
60
40
20
600
800
1000
1200
1400
1600
1800
2000
2200
2400
2600
2800
3000

(c)

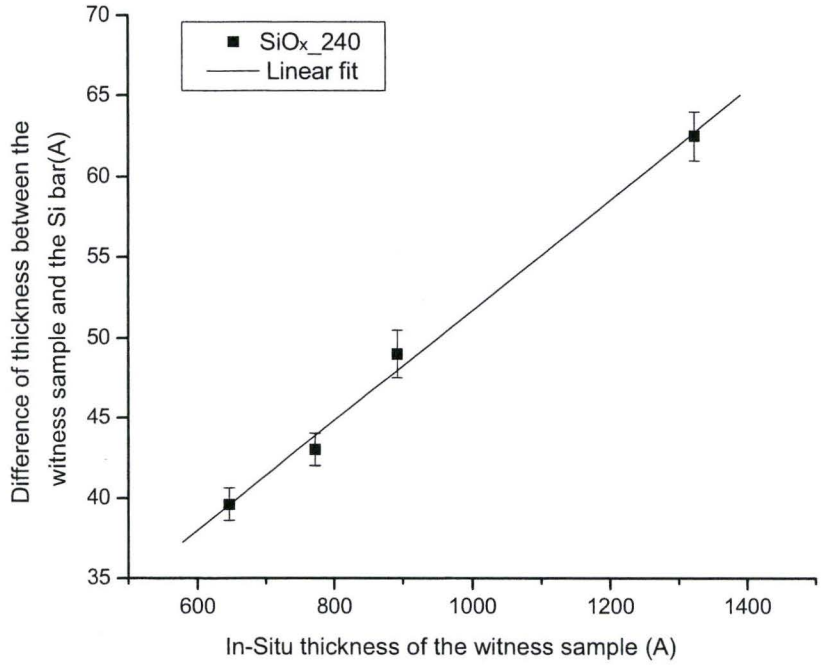

Figure 4.13 The difference of the thickness between the witness sample and the silicon bar for (a) SiO_x_140, (b) SiO_x_180 and (c) SiO_x_240 versus in-situ measured thickness of the witness sample and a linear fit.

Figures 4.13 (a), (b) and (c) show the difference of thickness between the witness sample and the silicon bar for SiO_x_140, SiO_x_180 and SiO_x_240 versus the in-situ measured thickness of the witness sample. As we can see, the thicker the grown film, the larger is the difference of thickness between the witness sample and the silicon bar. Based on the linear correlation, the real thickness of the film grown on the bar is extracted from the in-situ spectroscopic ellipsometric measurement.

Before using this information for the gain flattening coating, one ought to be aware that the calibration is done on many silicon bars. Actually, the calibration can only be performed on the silicon bar, because the laser beam spot of the ellipsometer is too large for the facet to be investigated and also the real laser bar is too small to handle

freely under the laser ellipsometer. There is also a possibility that the film grown on the silicon bar may be different from that grown on the InGaAsP based laser bar. To clarify the situation, a one-layer AR coating using the calibration result was designed and deposited on a laser.

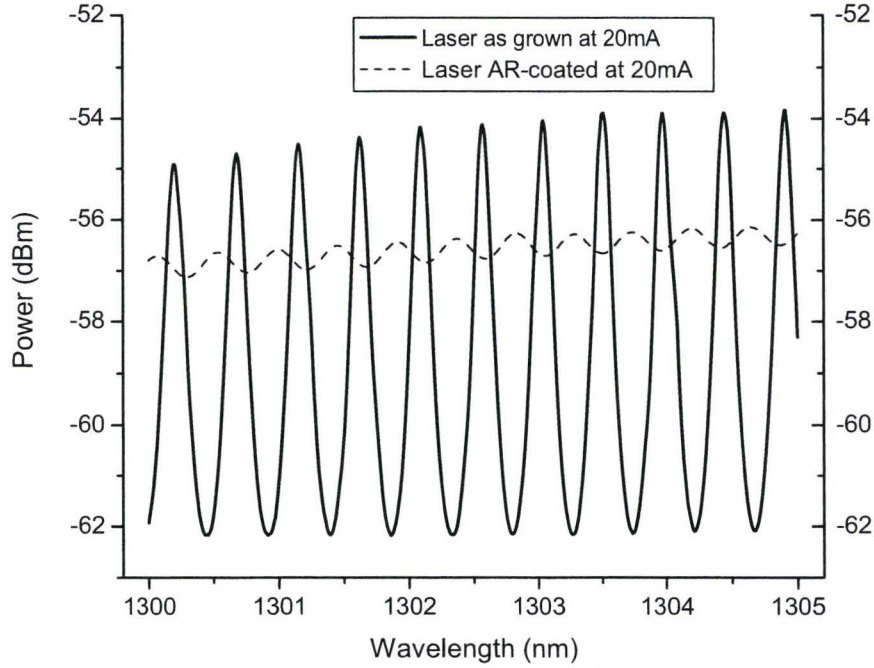

Figure 4.14 Power spectrum of an InGaAsP AMQW laser at a current of 20 mA as grown and after an AR coating was applied to one of the facets.

Figure 4.14 shows the power spectrum of an InGaAsP AMQW laser measured below threshold as grown and after an AR coating was applied to one of the facets. From the F-P mode oscillation, we can use the mode sum/min method mentioned in Chapter 2 to extract $RG_{uncoated}$ and RG_{coated} which are the RG products of the uncoated laser and AR coated laser. The RG product was defined in equation (2.7). Since the gain coefficient of the laser is the same for same current before and after the coating is deposited, we have:

$$\frac{RG_{coated}}{RG_{\text{uncoated}}} = \sqrt{\frac{R_{coated}}{R_{uncoated}}} \tag{4.11}$$

Because the reflection of the uncoated is known, we can calculate the achieved reflection of the coated facet through equation 4.11. Also, the theoretical reflectance was calculated from the thickness and refractive index from the in-situ spectroscopic ellipsometric measurement. Figure 4.15 shows the reflectance of the AR coated laser facet obtained from the *RG* product measurement and calculated theoretically from the deposited thickness and the refractive index. Note that the discrepancy between two curves is the result of errors between the film thickness actually grown and that expected. As they coincide, we conclude that the calibration of the bar holder is successful and the correlation is applicable to InGaAsP material, too.

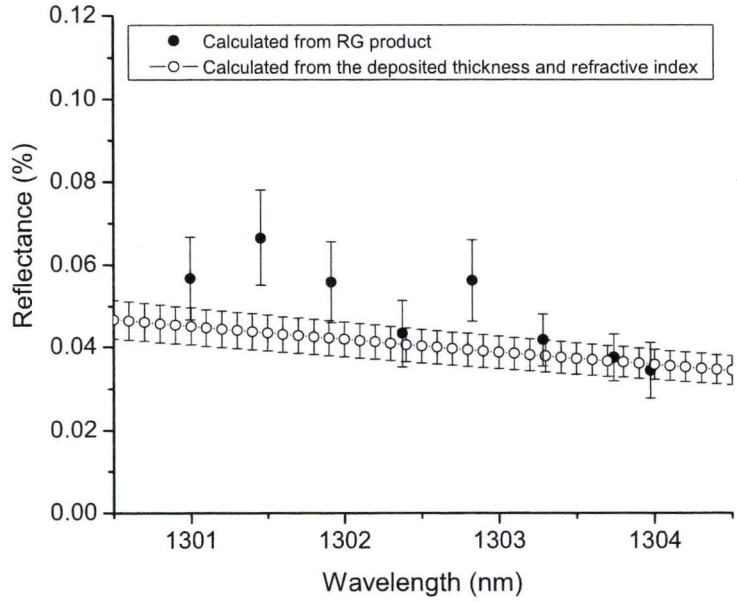

Figure 4.15 Reflectance of the AR coated laser facet calculated from the *RG* product and from deposited thickness and the refractive index.

4.6 Deposition of the gain flattening coating

Depositing an 18-layer coating to a laser facet is a challenging task. Since the laser bar is very small and inconvenient to handle, the chemical clean and drying should be kept to a minimum or totally avoided. It is always recommended to cleave the bar right before deposition. The facet should remain scratch free at all time, especially during the transportation. When installing the laser bar to the bar holder, an appropriate amount of clamping tension is needed for a snug hold. After the laser bar is installed, a gentle blow of pure nitrogen will remove any dust on the facet. Chemical solutions are only applied as the last resort for removing large particles followed by the blow dry of pure nitrogen. Every time the laser bar holder is taken out of the chamber for replacing the witness sample, extra care should be put into the handling.

When a deposition is initiated, the in-situ spectroscopic ellipsometer starts to fit for the refractive index and thickness. An estimated growth rate is instantly updated to closely monitor the deposition process. When the expected thickness is obtained, a shutter in front of the sample stage can stop the process immediately. From time to time the refractive index of the grown layer will not match expectations exactly, since it is the result of fitting from the ellipsometer data. In that case, the layer thickness needs to be adjusted accordingly, usually by keeping a constant optical thickness. After each layer is deposited, the achieved thickness and refractive index will be input to a program which will calculate and adjust the rest of layers to compensate the deviation occurred so far. This so called online re-optimization is useful to decrease the effect of accumulation of thickness errors which could cause a manufacture failure.

Chapter 5

Characterization

After deposition of the gain flattening coating onto the AMQW laser, several characterizations were carried out. The power spectra of the coated laser were obtained at various currents and the *RG* product was calculated accordingly, and then compared with those of the uncoated laser. The reflectance of the coated facet is thus extracted and compared with the designed reflectance. As one of the applications of the gain flattening coated AMQW laser, optical coherence tomography is discussed in this chapter. Measurement of the optical coherence length of the laser was set up based on a Michelson interferometer configuration and the interferogram was recorded and analyzed.

5.1 Power and *RG* spectrum with increasing currents of the coated laser

After the coating is deposited, the power spectra of the coated laser are obtained by coupling the laser light from one laser facet to a tapered single-mode fiber connected to an OSA. Figures 5.1 (a) and (b) show the power spectra of the laser before and after the application of the gain flattening coating for comparison. The measurements were both taken with increasing currents from 100 mA to 300 mA, in increments of 5 mA.

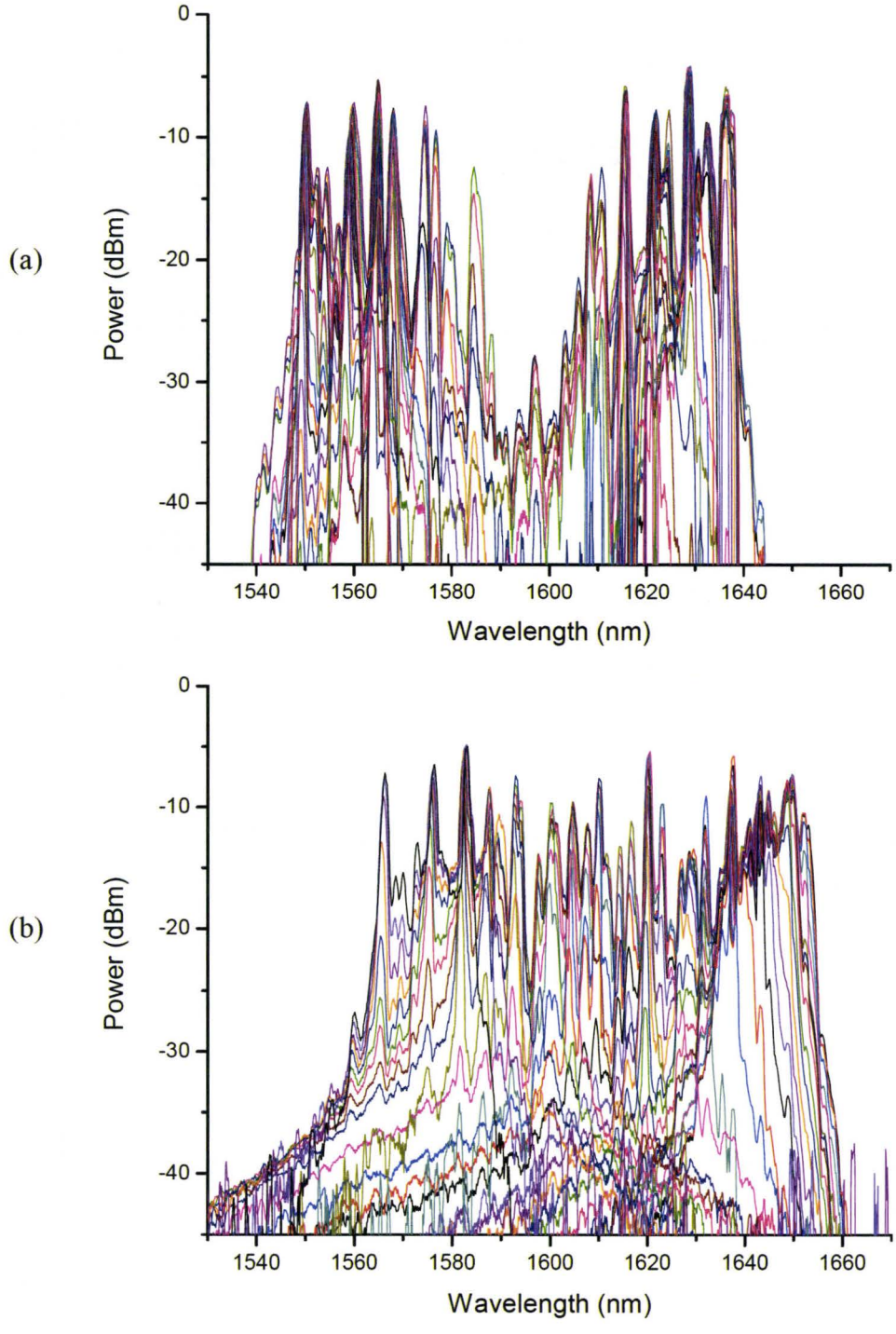

Figure 5.1 Power spectra of the AMQW laser (a) before and (b) after the gain flattening coating was deposited. The measurements were taken at currents increased from 100 mA to 300 mA with increments of 5 mA.

From Figure 5.1 (a), it is observed that there is a non-lasing gap of about 25 nm in the whole range of lasing wavelengths without any external feedback, as the uncoated laser gives a lasing range from 1545 nm to 1585 nm and from 1610 nm to 1640 nm, or about 70 nm in total. The reason for the observed behavior is that the long wavelength quantum well gets excited first and starts to contribute to the total gain beyond the threshold current; after reaching the transition current, the short wavelength quantum well starts to contribute to the total gain and to dominate gradually; the superposition of the gain curves from the long and short wavelength quantum well couldn't form a flat top in the middle of the whole lasing range.

In Figure 5.1(b), we notice that the lasing gap has disappeared. The lasing range is from 1565 nm to 1650 nm, or 85 nm in total. After the gain flattening coating is applied, the total lasing range has been increased by 15 nm along with the middle gap filled. It is believed that the wavelengths in the gap get enough feedback from the coated facet, and exceed the *RG* product of adjacent wavelengths to lase. Figure 5.2 shows the *RG* product curves of the coated laser at currents increased from 100 mA to 300 mA with increments of 5 mA. Note that the right most curve is from the 100 mA current and the left most one is from the current of 300 mA. Compared to Figure 2.5, as the current is increased little by little, the flat top of the *RG* curve shifts continuously from the longer wavelength to the shorter wavelength. It is also noticed that the lasing area is shifted towards longer wavelengths, which is characterized by the change of the reflectance after the gain flattening coating is deposited. After coating, the reflectance at the shorter wavelength has not been lifted as expected; however, the reflectance at the longer wavelength is

increased as designed. Appendix B reports the total number of samples grown and the achieved yield.

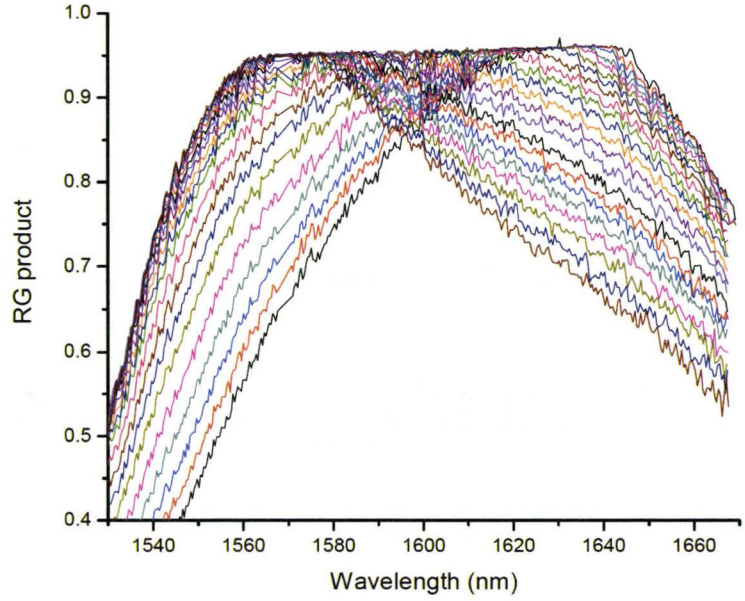

Figure 5.2 *RG* product spectra of the coated laser at currents increasing from 100 mA to 300 mA with increments of 5 mA.

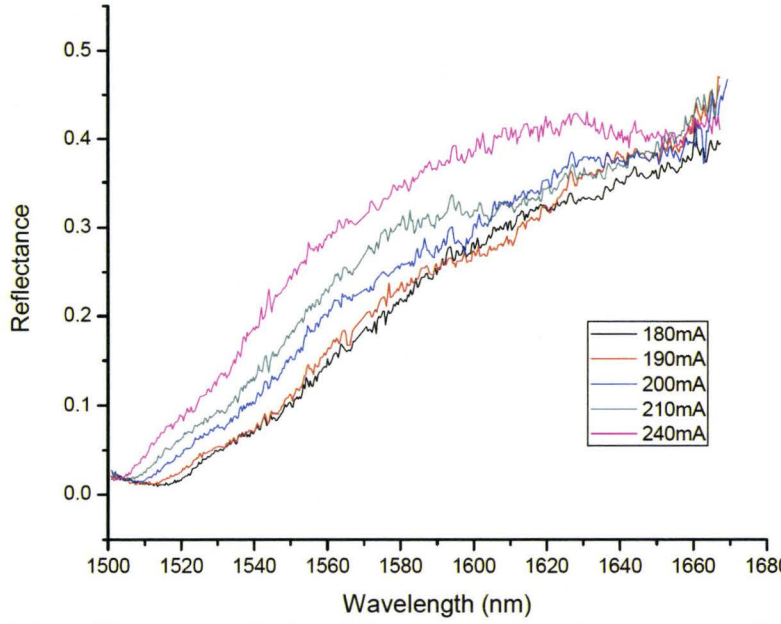

Figure 5.3 Reflectance calculated from the *RG* product spectra of the coated laser at different currents.

5.2 Reflectance of the coated facet

As mentioned before, the reflectance of the coated facet can be extracted from the *RG* product curve given the fact that the gain coefficient doesn't change for same current before and after the gain flattening coating is deposited. Figure 5.3 shows the reflectance calculated from the *RG* product spectra of the coated laser at various currents. As a function of the wavelength, the reflectance of the coated facet is constant no matter what current the measurement is taken at, and the differences of these curves should be the result of random error of the indirect measurement of *RG* product. The reflectance at the longer wavelengths is increased. Although the achieved reflectance at the shorter wavelengths starts to increase, it is not at the expected wavelength. Compared to Figure 3.15, we do find the difference between the reflectance of the deposited coating and that of the designed coating especially in the shorter wavelength edge, however, these two reflectance curve coincide well in the middle section.

The difference of the reflectance between the fabrication and theoretical design comes from several sources. First, the refractive index of the coating material fit by the spectroscopic ellipsometer varies from run to run, especially after a few layers are deposited. This variation is determined by the nature of the deposition. To produce SiO_x_240, a large ratio of the silane to the oxygen gas flow has to be used, and the small amount of oxygen magnifies the relative error of the mass flow control causing the refractive index to vary. Therefore, we cannot fix the refractive index of the coating material to only fit for the thickness, and the in-situ measurement has to monitor both.

Second, the wavelength range of the in-situ spectroscopic ellipsometer being used is from 600 nm to 1100 nm, which means that we have to extrapolate from that range to the wavelength of interest (~1600 nm) using the Cauchy dispersion model. When we are fitting to the collected data in the range of 600 to 1100 nm, we can only choose the best fitting which is decided by the mean square error (MSE) test. Smallest MSE means the best fitting. However, the extrapolation of the best fitting in range of 600 to 1100 nm to 1600 nm doesn't always reflect the actual values at 1600 nm. In an extreme case, such as that displayed in Figure 5.4, the two solid curves represents reality equally well in range of 600 to 1100 nm, but if we extrapolate them to 1600 nm, they will have much larger deviation, which could cause a problem. Unfortunately, we don't have complete control in this matter, since we can only utilize the result given by the in-situ measurement to start and stop a deposition. This can be improved by using an in-situ spectroscopic ellipsometer that operates around the wavelength of interest (~1600 nm).

Also, the refractive index of the substrate extracted from the waveguide structure may be slightly different from reality since several mechanisms can cause carrier recombination to happen slightly away from the quaternary bandgap, such as carrier-induced bandgap change, doping level, working temperature and strain. Among them, carrier-induced change is the major contribution to the change of the refractive index of InGaAsP [78-79]. In addition, when designing a coating for a laser, the modes of the laser are considered as plane waves, but in reality the modes are not plane waves, which could cause some difference of the reflectance between theoretical designs and experimental results.

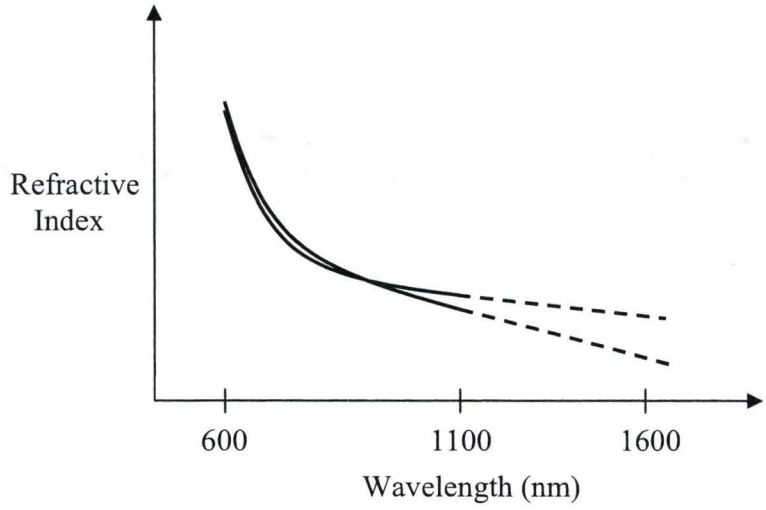

Figure 5.4 Schematic diagram of two Cauchy dispersions (solid) given by the spectroscopic ellipsometric measurement with equally good fit to the collected data in the range of 600-1100 nm. They are extrapolated (dash) to 1600 nm with a large deviation.

5.3 Application to optical coherence tomography

5.3.1 Optical coherence tomography

Since first used for *in vivo* high-resolution cross-sectional imaging of biological tissues [80] in 1991, optical coherence tomography (OCT) has been developed for imaging inner structures of biomedical tissues, based on the probe light being safe for living tissues in comparison with ionizing radiation such as X-rays and γ-rays. The traditional reflectometry technique detects a reflectance in the tissues from the intensity of reflected light. There are some difficulties to obtain a high dynamic range which is required to detect the light, because many biomedical tissues are highly scattering and the light intensity is usually weak even if near-infrared light is used. To overcome that, an OCT

imaging system mainly consists of a free-space or fiber-optics based interferometer along with a light source, a detector and low noise detection techniques.

Based on how the depth information is obtained, the OCT method is divided into two techniques: optical frequency domain reflectometry (OFDR) [81-82] and optical coherence domain reflectometry (OCDR) [83-85]. The interference fringes are encoded with the cross-sectional or depth information, and only observed when the optical path lengths of the reference and sample arms are matched within the coherence length of the light source.

OFDR, also known as Fourier domain OCT, uses a narrow band source that sweeps continuously over a wide optical frequency. The optical path difference in the interferometer is addressed in beat frequencies of the interference intensity. The power spectrum of the beat signal provides the reflectance distribution along the depth direction in the object. The depth information is acquired by taking a Fourier transform of the interferogram and the depth resolution is inversely proportional to the sweeping range. In this method of sweeping the optical frequency, however, it is difficult to obtain high depth resolution because of mode hopping and power variation of the laser source.

OCDR, also known as time domain OCT, extracts the depth information, whose position is balanced with the reference arm length in the interferometer, by utilizing a coherence gate of a broad bandwidth source such as super-luminescent diodes (SLD). However the depth resolution cannot be controlled, because the gate-width of the coherence function is determined by the bandwidth of the light source. In tomographic imaging it is important that the depth resolution can be adjusted to detect weak light with

high efficiency. Synthesis of the optical coherence function makes it possible to control the depth resolution. Several methods of synthesizing this function have been proposed [25-26, 86-87] to make the synthesized OCT (SOCT). Synthesis of an incoherent source from a coherent source was first applied to OCT in 1999 [26]. Instead of a low-coherence source, a tunable diode laser is utilized in SOCT. By rapidly tuning the laser wavelength over a broad spectral region and by appropriate averaging, the time-averaged optical coherence function decides the depth resolution in an imaging system. Compared to the OCT using an SLD as a source, the SOCT approach has the advantage of the controlled depth resolution, higher power in a small spectral interval and higher brightness which enables an easier coupling to optical fiber.

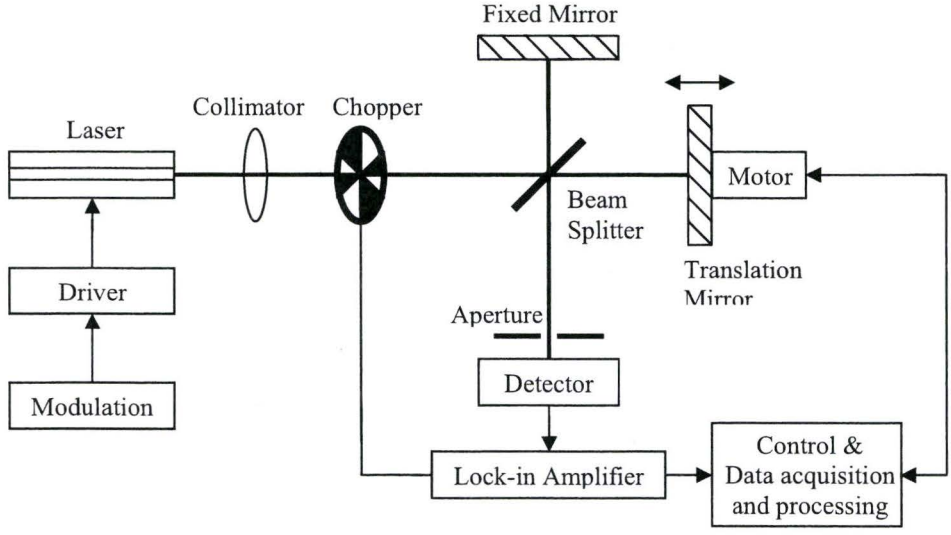

Figure 5.5 Schematic diagram of the synthesized OCT using a tunable AMQW diode laser with current modulation.

5.3.2 Measurement of the optical coherence length

In SOCT, the highest resolution of the depth information is proportional to the optical coherence length of the source. Therefore the light source is a critical element in

obtaining high depth resolution. The coherence length of the gain flattening coated laser is measured in the experimental setup displayed in Figure 5.5.

The gain flattening coated AMQW laser is operating on a Peltier cooler kept at a constant temperature of 18 °C. The laser driver is equipped with external modulation up to 100 kHz. An arbitrary waveform generator is used for external modulation. The light beam is modulated by a chopper which connects to a lock-in amplifier as a reference. The light beam reaches the beam splitter and divides into two beams. One of the beams is reflected from a fixed mirror while the other is reflected from a translated mirror controlled by a stepper motor. The moving mirror allows the difference of two optical paths to vary. The two beams are aligned to overlap forming an interference pattern in the opposite direction of the fixed mirror if the difference of two optical paths is within the coherence length. Because the synthesized coherence function is multi-peaked with a definite spacing, the secondary peaks in the coherence function may appear on the depth resolution, which is called the aliasing effect [88] and therefore, the measuring range must be limited. In the experiment, a confocal spatial filter, i.e. a collimating lens and an aperture in front of the detector are used to minimize the aliasing effect. When the optical path difference is varied by moving the translation mirror, the interference pattern is shifting between construction and deconstruction, and the detector records the interferogram which is the intensity of the fringes as a function of the path difference.

While the chopper shuts and opens the light path at a given frequency, the lock-in amplifier works as a low-pass filter to time-average the signal from the detector. When the time constant of the low-pass filter is to be longer than one period of the modulation

of the laser, the synthesis of a low-coherence function from a coherent source is achieved. In SOCT, to achieve a two dimensional image of the sample, both depth scanning of the reference mirror and the lateral scanning are required.

5.3.3 Modulation of the laser and interferogram

In SOCT, the time constant of the low-pass filter needs to be longer than one period of the modulation of the laser to achieve the synthesis of a low-coherence function from a coherent source. Therefore, how fast the laser can sweep through the wavelengths determines the speed of SOCT imaging, i.e., the faster the modulation of the laser, the higher is the speed of imaging.

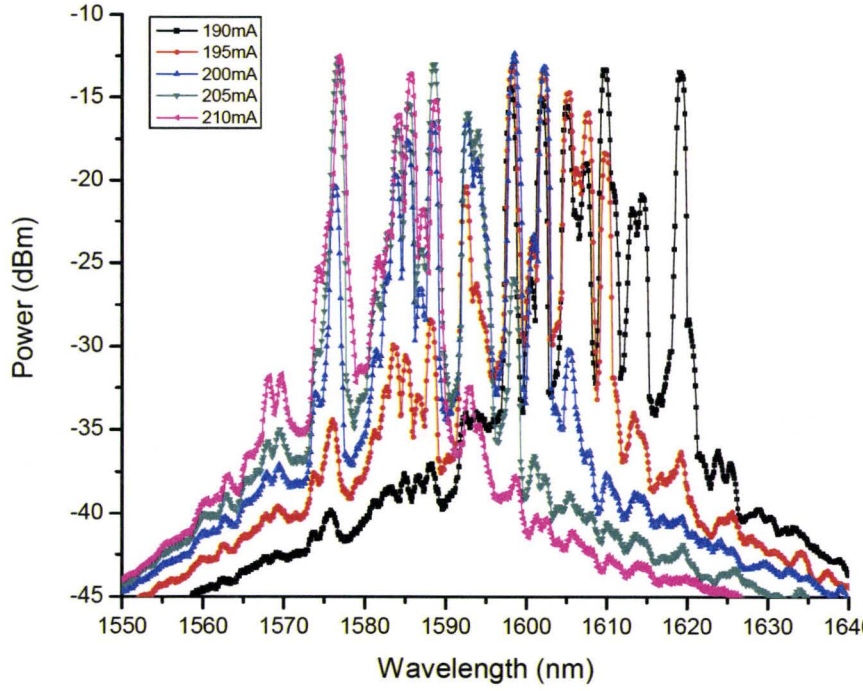

Figure 5.6 Power spectra of the coated AMQW laser at the currents where the transition of lasing wavelength is taking place.

Since the coated laser has the threshold current of 100 mA and saturates around 300 mA, 200 mA is set as the mid-point of the current modulation. We can also observe from Figure 5.6 that the wavelength of lasing is in transition from the longer wavelength to the shorter wavelength at currents of around 200 mA. It is noticed that by increasing the current by 20 mA from 190 mA to 210 mA, the laser has swept from 1620 nm to 1575 nm, while increasing the current by 90 mA from 210 mA to 300 mA is needed to achieve the longest lasing wavelength of 1650 nm and vice versa to achieve the shortest lasing wavelength of 1565 nm at around 100 mA. In other words, the change of currents is not linearly related to the wavelength that has swept through.

In order to have a more uniform intensity over the entire lasing range, it would be ideal to have such modulation that the current can stay longer between 190 mA to 210 mA in a period. However, the arbitrary waveform generators to which we have access are unable to produce the programmed waveform at a sufficiently high frequency. Among the standard waveforms, the triangle wave has been found to give a better result than the sine wave, as the sine wave has more time at the turning point current of 100 mA and 300 mA. Figure 5.7 shows the power spectra of the coated AMQW laser modulated with the triangle waveform at the frequency of 100 kHz synchronized by an OSA.

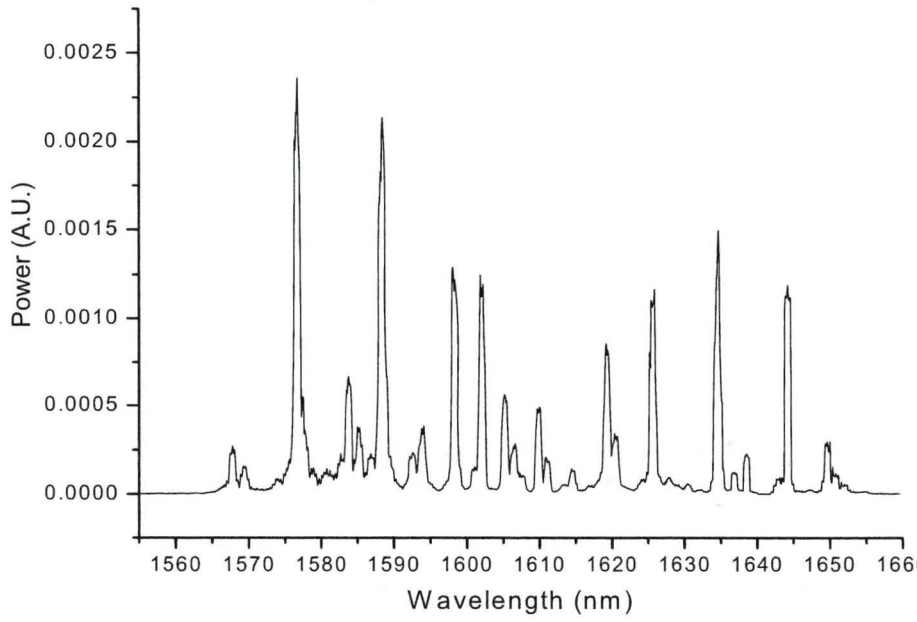

Figure 5.7 Power spectra of the coated AMQW laser modulated with the triangle waveform at the frequency of 100 kHz and OSA synchronized.

Once the laser is modulated, by moving the translation mirror, we vary the optical path difference between the two arms to shift the interference pattern, and the detector records the interferogram, which is the intensity of the fringes measured as a function of the path difference. Figure 5.8 shows the interferogram of the gain flattening coated AMQW laser modulated with the triangle waveform at a frequency of 100 kHz. The full width half maximum (FWHM) coherence length is measured as 40 μm. Since the OCT depth resolution equals the coherence length of the light source [89], the depth resolution we could achieve with this particular configuration of an AMQW laser is characterized as 40 μm compared to 13 μm [25] in an external cavity laser using a diffractive optical element for wavelength selection.

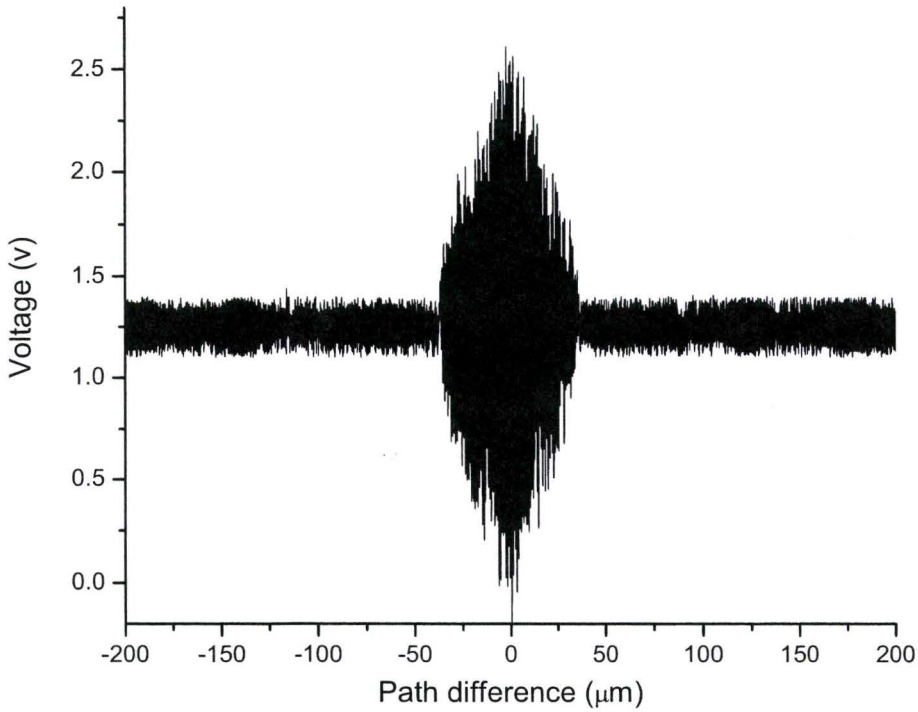

Figure 5.8 Interferogram of the gain flattening coated AMQW laser modulated with the triangle waveform at the frequency of 100 kHz.

5.3.4 Temporal coherence

To discuss how the interferogram forms, it is worth mentioning the distinction between two types of coherence, i.e., temporal and spatial coherence. Considering temporal coherence, we are concerned with the ability of a light beam to interfere with a delayed version of itself, while spatial coherence concerns the ability of a light beam to interfere with a spatially shifted version of itself. To describe the experiment mathematically, the notation from Ref. [90] is used.

Let $u(P,t)$ be the complex scalar representation of an optical disturbance at point P in space and instant t in time. Associated with $u(P,t)$ is a complex envelope $A(P,t)$. Since $u(P,t)$ has a finite bandwidth $\Delta\nu$, we expect the amplitude and phase of $A(P,t)$ to

be changing at a rate determined by $\Delta\nu$. If finite time duration τ is of interest, we expect $A(P,t)$ to remain relatively constant during the interval τ provided $\tau << 1/\Delta\nu$. In other words, the time functions $A(P,t)$ and $A(P,t+\tau)$ are highly correlated, or coherent, provided τ is much less than the coherence time $\tau_c = 1/\Delta\nu$.

In the Michelson interferometer configuration displayed in Figure 5.4, if the mirror is moved from the position required for equal path lengths in the two arms of the interferometer, a relative time delay is introduced between the two interfering beams. As the mirror moves, the light falling on the detector passes from a state of constructive interference to a state of destructive interference and back to constructive interference, with a mirror movement of $\overline{\lambda}/2$ between bright fringes. Superimposed on this rapid oscillation of intensity is a gradual tapering envelope of fringe modulation, caused by the finite bandwidth of the source and the gradual decorrelation of the complex envelope of the light as the path length difference increases.

The source of broad spectrum can be regarded as consisting of many monochromatic components. Each such component generates a perfectly periodic contribution to the interferogram, but with a period depending on its particular optical frequency. At zero path length difference $(h=0)$, all such components add in phase, producing a large central peak in the interferogram. As the mirror is displaced from the zero-delay position, each monochromatic fringe suffers a phase shift that depends on its particular temporal frequency. The result is a partially destructive addition of the elementary fringes and a consequent drop in the fringe depth on the interferogram. When

the relative delay grows large enough, the addition of elementary fringes is nearly totally destructive, and the interferogram remains at its constant average value.

Taking account of the relative time delay $2h/c$ experienced by the light in the arm with the movable mirror, the intensity incident on the detector can be written as:

$$I_D(h) = \left\langle \left| K_1 u(t) + K_2 u\left(t + \frac{2h}{c}\right) \right|^2 \right\rangle \tag{5.1}$$

where K_1 and K_2 are real numbers determined by the losses in the two paths and $u(t)$ is the analytic signal representation of the light emitted by the source. If we define $I_0 = \left\langle |u(t)|^2 \right\rangle = \left\langle \left| u\left(t + \frac{2h}{c}\right) \right|^2 \right\rangle$ and $\Gamma(\tau) = \langle u(t+\tau)u^*(t) \rangle$ which is the autocorrelation function of the analytic signal $u(t)$ and known as the self coherence function of the optical disturbance, we can expand equation 5.1 and obtain the following equations:

$$\begin{aligned} I_D(h) &= (K_1^2 + K_2^2) I_0 + K_1 K_2 \Gamma\left(\frac{2h}{c}\right) + K_1 K_2 \Gamma^*\left(\frac{2h}{c}\right) \\ &= (K_1^2 + K_2^2) I_0 + 2K_1 K_2 \,\mathrm{Re}\left\{\Gamma\left(\frac{2h}{c}\right)\right\} \end{aligned} \tag{5.2}$$

Noting that $I_0 = \Gamma(0)$, we choose to normalize by this quantity, giving $\gamma(\tau) = \frac{\Gamma(\tau)}{\Gamma(0)}$, which is the complex degree of coherence of the light. Therefore, equation 5.2 can be written as:

$$I_D(h) = (K_1^2 + K_2^2) I_0 \left[1 + \frac{2K_1 K_2}{K_1^2 + K_2^2} \mathrm{Re}\left\{\gamma\left(\frac{2h}{c}\right)\right\} \right] \tag{5.3}$$

In the vicinity of zero relative path length difference $(h \cong 0)$, we have $\gamma(2h/c) \cong 1$. Thus near the origin, the interferogram consists of a fully modulated cosine, with

intensity varying from $4K^2I_0$ to zero with the mean of $2K^2I_0$. As the path length difference h is increased, the amplitude modulation $\gamma(2h/c)$ falls from unity towards zero, and in addition the fringes may experience a phase modulation depending on the nature of the light source.

The depth of the fringes observed in the vicinity of any path length difference h can be described in precise terms using the concept of fringe visibility. The visibility of a sinusoidal fringe pattern is defined by:

$$V = \frac{I_{\max} - I_{\min}}{I_{\max} + I_{\min}} \tag{5.4}$$

where $I_{\max}$ and $I_{\min}$ are the intensities at the maximum and minimum of the fringe. In the near vicinity of mirror displacement h, the interferogram in equation 5.3 can be seen to have a visibility:

$$V(h) = \left|\gamma\left(\frac{2h}{c}\right)\right| = \gamma\left(\frac{2h}{c}\right) \tag{5.5}$$

when losses in the two arms are equal. For unequal losses, the visibility is:

$$V(h) = \frac{2K_1K_2}{K_1^2 + K_2^2}\gamma\left(\frac{2h}{c}\right) \tag{5.6}$$

As the path length difference $2h$ grows large, the visibility of the fringes drops, and the relative coherence of the two beams is considered diminished. When the visibility has fallen to approximately zero, we consider that the path length difference has exceeded the coherence length of the light.

As mentioned above, the character of the interferogram obtained from a Michelson interferometer is determined by the self coherence function $\Gamma(\tau)$ or equivalently by the complex degree of coherence $\gamma(\tau)$, of the light emitted by the source. We have the relationship between the correlation functions and the power spectral density of the source defined as

$$\Gamma(\tau) = \int_0^\infty 4P^{(r,r)}(\nu) e^{-i2\pi\nu\tau} d\nu \tag{5.7}$$

where $P^{(r,r)}(\nu)$ is the power spectral density of the real-valued optical disturbance $u^{(r)}(t)$. Therefore, the character of the interferogram observed with a Michelson interferometer can be completely determined if the power spectral density of the light is known. Also, by the measurement of the interferogram it is possible to determine the unknown power spectral density of the incident light, which is known as Fourier spectroscopy.

The general steps involved in obtaining a power spectrum are as follows. First, the interferogram is measured. The movable mirror travels from a region of large path length difference through the position of zero path length difference into the opposite region of large path length difference. The intensity of the light is measured as a function of the path difference of the interferometer arms during this process, and the resulting interferogram is digitized. A digital Fourier transformation, usually a fast Fourier transform (FFT), is used to yield a spectrum in the frequency domain. If an interferogram is represented as a function of $I(\delta)$ with $\delta = \frac{2h}{c}$, the power spectral density $P(\nu)$ is defined [91] as: $P(\nu) = (const.)\int_{-\infty}^{\infty} \left\{ \left[I(\delta) - \frac{1}{2} I(0) \right] \cos(2\pi\nu\delta) \right\} d\delta$.

In practice, several possible considerations need to be addressed. Since the interferogram is sensitive to any mechanical vibration of the environment, the experiment needs to be set up on stabilized optical table to minimize the low frequency noise coming from object movement such as people walking and door banging. Other low or high frequency noise can be digitally filtered away. Also, the mirror on the translation motor isn't necessarily exactly perpendicular to the axis by which the mirror moves in the experiment, say $\theta \neq 90$. This means that if the mirror moves a distance x along the axis, instead of being $2x$, the path length changed can be either $2x\sin\theta$ or $\frac{2x}{\sin\theta}$ depending on the setup. Also the position of the translation mirror recorded in the micrometer may also have errors and has to be corrected accordingly. We know that at zero pathlength difference the period of the fringes is $\frac{\bar{\lambda}}{2}$, where $\bar{\lambda}$ is the mean wavelength. Using the mean wavelength of the lasing range from the power spectrum with increasing current, the x-axis of the interferogram, which is the distance of mirror translation in micrometers can be corrected.

Figure 5.9 shows the power spectrum of the coated AMQW laser modulated in the triangle waveform of 100 kHz rendered from the interferogram displayed in Figure 5.8. It is observed that the intensity in the wavelengths where the tuning is very sensitive to the increasing current is much less than that in the shorter and longer wavelengths. It would be good to have the current increase slowly in the mid-point current in every period to achieve more uniform intensities over the entire lasing range. Custom programmed waveforms are needed to improve the performance.

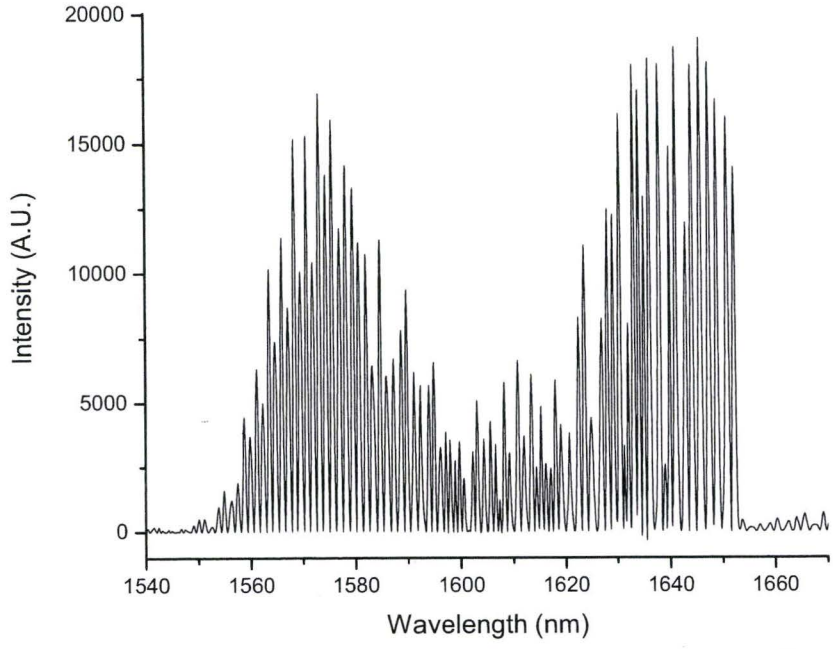

Figure 5.9 Spectral intensity of the coated AMQW laser modulated in triangle waveform of 100 kHz.

Chapter 6

Conclusions and future work

6.1 Conclusions

In this work, compositionally asymmetric multiple quantum well lasers were used for the demonstration of the gain flattening coating functionality. The gain spectra of the lasers were extracted using a non-linear least square fitting method. An optimum facet reflectance spectrum was calculated for the chosen current. However the coating having the exact reflectance required a number of layers and total thickness that was not manufacturable in the lab. A modified reflectance spectrum was proposed and assembled, in order to achieve operation over a wider spectral range without the 'difficult' gap which was a region in the middle of the tuning range where lasing was difficult or impossible to achieve.

The well known theoretical basis for the calculation of reflectance and transmittance from a given coating structure was summarized, along with the needle-like variation of refractive index method and a few merit function optimization methods for synthesizing a coating. Design strategies including choosing starting design, target selection, the procedure of gradual evolution and refining a design were discussed. For

the ICP-CVD system, we could grow stacks of silicon oxide films to the laser facet with the total thickness up to 4 μm without cracking after cooling down to room temperature or other optical deterioration during the laser operation. The total number of the layers was limited to 18 and it was preferred to have a layer no thinner than 40 nm, which served as the stopping criteria for a final design. Silicon oxides films with high, medium, and low refractive indices were chosen as the building blocks of the gain flattening coating. Effective index method was used to estimate the refractive index of the laser facet. The multi-layer coating to flatten the laser gain spectrum was designed by the insertion of needle-like refractive index variation with a few optimization methods applied to minimize the merit function.

The gain flattening coating was fabricated in the ICP-CVD system with an in-situ spectroscopic ellipsometric measurement. A laser bar holder was custom designed and fabricated to accommodate the laser bar during deposition with the ability to not only hold the bar tightly enough not to lose it during the loading-unloading procedure and rotation motion in deposition, but also not to break it after the holder was heated at certain temperatures, which caused thermal expansion.

In the ICP-CVD system, the thickness uniformity was subject to many factors and among these factors, the distance between the plasma source and the sample played a crucial role in achieving uniform thickness. The position where to achieve a large area uniformity of deposition was optimized, however uniform thickness of deposited films on a laser facet was not necessarily obtained. It was found that the height of the screws which fix the clamping metal piece had a substantial impact on the uniformity of

thickness. Experiments and modification on the laser bar holder were carried out to achieve a uniform film on the laser facet. Through the SEM and ellipsometric measurement, the film deposited on the laser facet was found significantly thinner than that on the witness sample, while the refractive indices of both were considered identical. The thicker was the grown film, the larger was the difference of thickness between the witness sample and the silicon bar. A linear correlation between the thickness of the film grown on the bar and witness sample was established. A one layer AR coating that was designed using the calibration result and deposited onto an InGaAsP based laser had confirmed the linear correlation. The 18-layer gain flattening coating was deposited to the laser facet with the witness sample changed twice during deposition. The in-situ spectroscopic ellipsometer monitored the growing layer with the refractive index and thickness of the film fitted from time to time compared to the design while an online re-optimization of the rest of the layers was used to decrease the possibility of manufacture failure.

After the deposition, the power spectrum of the coated laser was compared to that of an uncoated laser. It was observed that the non-lasing gap had disappeared after the gain flattening coating was applied. Without external feedback, the coated laser showed tuning over 85 nm, while the uncoated laser had a non-lasing gap of about 25 nm in the central region of the tuning range of 70 nm. The *RG* product curve of the coated laser showed that as the current was increased little by little, the flat top of the *RG* curve shifted continuously from the longer wavelength to the shorter wavelength, meaning

continuous tunability over the entire range. The reflectance of the coated facet was calculated and compared to the designed reflectance with the success and error discussed.

Finally, the depth resolution for SOCT using the gain flattening coated AMQW laser was measured by using Michelson interferometer. The highest depth resolution that could be achieved with this gain flattened laser was 40 μm as the current applied to the laser was modulated with a triangle waveform at a frequency of 100 kHz between 100 mA and 300 mA. The power intensity of the synthesized low coherence light source from the gain flattening coated AMQW laser was rendered from the interferogram using fast Fourier transform (FFT).

6.2 Future work

As a material for calibration and witness sample, the silicon wafer is an economical choice considering the amount of materials consumed. But it prevents us from using higher refractive index silicon oxides or amorphous silicon as a coating material since the silicon oxides with little or no oxygen is hard to be distinguished from the silicon substrate via ellipsometry. If other materials such as single side polished GaAs or quartz can be used, we could use higher refractive index silicon oxides or amorphous silicon as the coating material and the advantage would be the smaller total thickness and fewer layers required.

As mentioned the total thickness of the coating is determined by the complexity of the target reflectance spectrum. If in practice the function of the coating could be limited to just flatten the gain in the middle, the higher reflectance around the lasing range won't be needed and it will greatly decrease the complexity of the reflectance

spectrum. Therefore less demanding coatings can be designed and fabricated for possible applications.

In the SOCT, the modulation of laser decides the power spectrum of the synthesized low coherence light source. But since the tuning of the wavelength is sensitive to the current increment at the transition current, the intensity in the middle wavelengths is much less than that in the shorter and longer wavelengths. It would be good to have the current stay longer and increase slowly in the mid-point current in every period. A custom programmed waveform such as Figure 6.1 with a high modulation frequency is expected to increase the power intensity of the synthesized light source in the middle wavelengths.

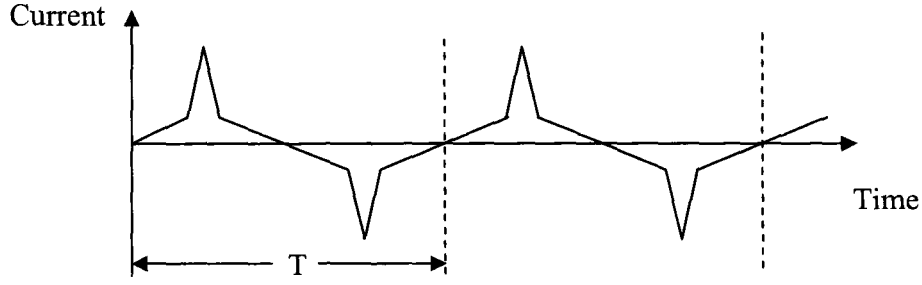

Figure 6.1 Waveform of modulation to increase the power intensity of the SOCT light source in the middle wavelengths.

Appendix A

Constant α

The field of the incident plane wave can be expressed as:

$$\breve{E} = \vec{E}_0 \exp\left(-i\vec{k}\vec{r} + i\omega t\right) \tag{A.1}$$

Where $\vec{E}_0$ is the field amplitude, $\vec{k}$ is the wave vector of the incident wave, and $\vec{r} = \{x, y, z\}$ is the coordinate vector. In a homogeneous isotropic medium of ε_a, $\vec{k}$ is equal to $k\sqrt{\varepsilon_a} \cdot \vec{l}$ where $\vec{l}$ is the unit directing vector. If we decompose the incident wave in the direction shown in Figure 3.1, the vector is: $\vec{l} = \{0, -\sin\gamma_a, -\cos\gamma_a\}$. Then the incident wave field can be written as:

$$\breve{E} = \vec{E}_0 \exp\left(ik\sqrt{\varepsilon_a}\left(y\sin\gamma_a + z\cos\gamma_a\right) + i\omega t\right) \tag{A.2}$$

Compared to $E_x(y,z) = u(z)\exp(ik\alpha y)$ defined in chapter 3.1, it is obtained:

$$\alpha = \sqrt{\varepsilon_a}\sin\gamma_a . \tag{A.3}$$

This equation actually represents the Snell law. α is the same in the substrate, outer space and all layers:

$$\alpha = \sqrt{\varepsilon_a}\sin\gamma_a = \sqrt{\varepsilon_s}\sin\gamma_s = \sqrt{\varepsilon_j}\sin\gamma_j \tag{A.4}$$

It is also valid when the medium is absorbing. In that case, a complex permittivity $\tilde{\varepsilon}$ is used in stead of ε.

Appendix B

Fabrication of gain flattening coatings and yield considerations

During the fabrication, approximately 30 batches of laser bars were treated with facet coatings to flatten the gain. Nine of them did not make it to the test of spectral output after the deposition. Some of them were destroyed by the force of the clamping metal piece when they were mounted to the laser bar holder, while others broke into pieces when they were taken off the sample holder. Among the 22 laser bars which were measured, six samples did not lase at all and two samples displayed little lasing at the longer wavelengths possibly due to them having scratched facets. Among the 14 bars which were lasing, 3 displayed output spectra similar to that shown in Fig. 5.1. The rest of the lasers displayed lasing but did not cover the entire range. Figs. A.1 and A.2 show the typical power spectra.

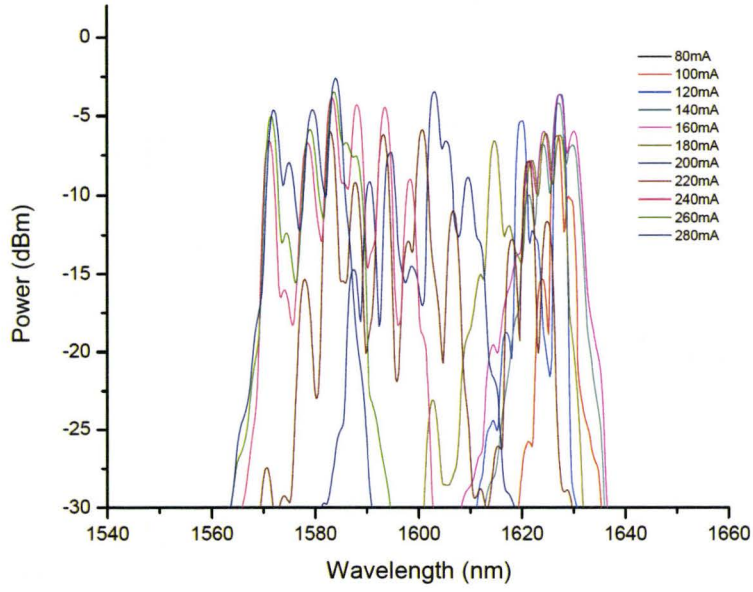

Figure A.1 Power spectra of an AMQW laser after the gain flattening coating was deposited. The measurements were taken at currents increased from 80 mA to 280 mA.

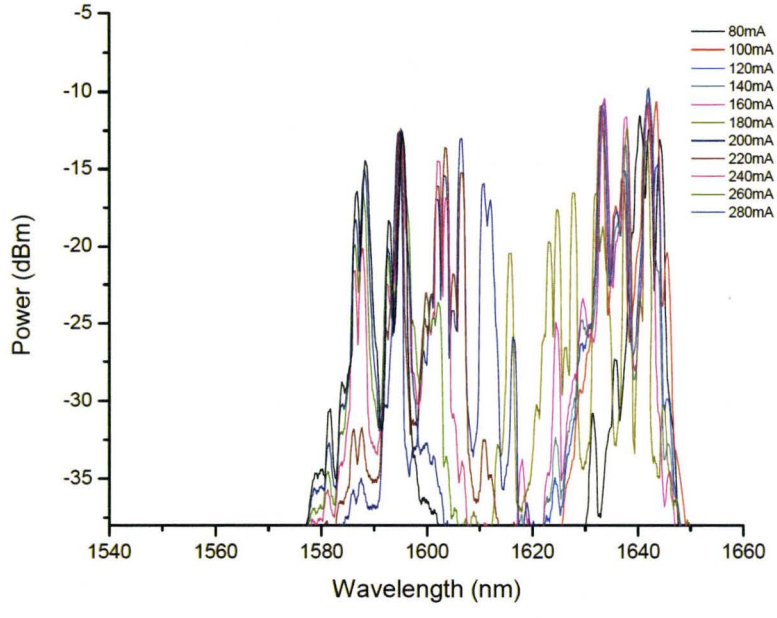

Figure A.2 Power spectra of an AMQW laser after the gain flattening coating was deposited. The measurements were taken at currents increased from 80 mA to 280 mA.

References

[1] R. N. Hall, G. E. Fenner, J. D. Kingsley, T. J. Soltys, and R. O. Carlson, "Coherent Light Emission From GaAs Junctions," *Phys. Rev. Lett.*, **9** (1962) 366–369

[2] Zh. I. Alferov, V. M. Andreev, D. Z. Garbuzov, and Yu. V. Zhilyaev, "Investigation of the influence of the AlAs-GaAs heterostructure parameters on the laser threshold current and the realization of continuous emission at room temperature," *Sov. Phys. Semicond.*, **4** (1971) 1573-1575

[3] I. Hayashi, M. B. Panish, P. W. Foy, and S. Sumski, "Junction lasers which operate continuously at room temperature," *Appl. Phys. Lett.*, **17** (1970) 109-111

[4] I. Ladany, M. Ettenberg, H. F. Lockwood, and H. Kressel, "Al_2O_3 half-wave films for long-life cw lasers," *Appl. Phys. Lett.*, **30** (1977) 87-88

[5] Y. Shima, N. Chinone, and R. Ito, "Effects of facet coatings on the degradation characteristics of GaAs-$Ga_{1-x}Al_xAs$ DH lasers," *Appl. Phys. Lett.*, **31** (1977) 625-627

[6] T. Yuasa, K. Endo, T. Torikai, and H. Yonezu, "Facet protection of (AlGa)As lasers using SiO_2 sputter deposition," *Appl. Phys. Lett.*, **34** (1979) 685-687

[7] I. P. Koutzarov, H. E. Ruda, C. H. Edirisinghe, L. Z. Jedral, Q. Liu, A. Moore, R. Henderson, M. G. Boudreau, M. Boumerzoug and P. Mascher, "Optical characterization of passivation for high power $Al_xGa_{1-x}As$ based lasers," *Society of Photo-Optical Instrumentation Engineers*, **2382** (1995) 42-48

[8] M. Ettenberg, "A new dielectric facet reflector for semiconductor lasers," *Appl. Phys. Lett.*, **32** (1978) 724-725

[9] T. Ohtoshi, T. Kawano, Y. Sasaki, T. Kajimura, N. Chinone, and M. Nakamura, "High-power visible GaAlAs lasers with self-aligned strip buried heterostructure," *J. Appl. Phys.*, **56** (1984) 2491-2496

[10] K. Hamada, M. Wada, H. Shimizu, M. Kume, F. Susa, T.Shibutani, N. Yoshikawa, K. Itoh, G. Kano, and I. Teramoto, "A 0.2 W CW laser with buried twin-ridge substrate structure," *IEEE J. Quantum. Electron.*, **21** (1985) 623-628

[11] R. Tkach and A. Chraplyvy, "Regimes of feedback effects in 1.5-μm distributed feedback lasers," *J. Lightwave Technol.*, **4** (1986) 1655-1661

[12] L. Thylen, "Amplified spontaneous emission and gain characteristics of Fabry-Perot and traveling wave type semiconductor laser amplifiers," *IEEE J. Quantum Electron.*, **24** (1988) 1532-1537

[13] L. Atternas and L. Thylen, "Single-layer antireflection coating of semiconductor lasers: Polarization properties and the influence of the laser structure," *J. Lightwave Technol.*, **7** (1989) 426-430

[14] G. Eisenstein and S. W. Stulz, "High quality antireflection coatings on laser facets by sputtered silicon nitride," *Appl. Opt.*, **23** (1984) 161-164

[15] I. F. Wu, I. Riant, J. M. Verdiell, and M. Dagenais, "Real-time in situ monitoring of antireflection coatings for semiconductor laser amplifiers by ellipsometry," *IEEE Photon. Technol. Lett.*, **4** (1992) 991-993

[16] T. Saitoh, T. Mukai, and O. Mikami, "Theoretical analysis and fabrication of antireflection coatings on laser diode facets," *J. Lightwave Technol.*, **3** (1985) 288-293

[17] M. C. Farries, J. Buus, and M. Kearley, "Design and fabrication of two layer antireflection coatings for semiconductor optical amplifiers," *Electron. Lett.*, **26** (1990) 1626-1628

[18] J. Lee, T. Tanaka, S. Uchiyama, M. Tsuchiya, and T. Kamiya, "Broadband double-layer antireflection coatings for semiconductor laser amplifiers," *Japan J. Appl. Phys.*, **36** (1997) 52-54

[19] D. M. Braun and R. L. Jungerman, "Broadband multilayer antireflection coating for semiconductor laser facets," *Opt. Lett.*, **20** (1995) 1154-1156

[20] K. Shigihara, T. Aoyagi, S. Kakimoto, M. Aiga, M. Ostubo, and K. Ikeda, "Antireflection coating for laser diodes," *Electron. Lett.*, **31** (1995) 1574-1576

[21] E. Marclay, D. J. Webb, P. Buchmann, and P. Vettiger, "Stepwise-graded-index multilayer broadband low-reflectivity coating for AlGaAs/GaAs power lasers," *Appl. Phys. Lett.*, **55** (1989) 942-944

[22] J. E. Fouquet, D. M. Braun, and G. R. Trott, "Wavelength-dependent optimum output coupling enhances performanceof external-cavity-tuned semiconductor lasers at 1.5 μm," *IEEE J. Quantum. Electron.*, **32** (1996) 1777-1781

[23] A.E. Siegman, *Lasers*, Mill Valley, CA: Univ. Sci. Books (1986) 473-481

[24] H. Hiratsuka, K. Morisaki and T. Yoshimura, "Optical Coherence Tomography System based on Synthesis of Optical Coherence Function With a Wavelength-Scanning Laser Source," *Optical Review*, **7** (2000) 442-447

[25] J. Wang and D. T. Cassidy, "Broadly tuneable, short external cavity diode laser for optical coherence tomography," *IET Optoelectronics*, **2** (2008) 46-54

[26] Z. He and K. Hotate, "Synthesized optical coherence tomography for imaging of scattering objects by use of a stepwise frequency-modulated tuneable laser diode," *Opt. Lett.*, **24** (1999) 1502-1504

[27] L. Ricci, M. Weidemuller, T. Esslinger, A. Hemmerich, C. Zimmermann, V. Vuletic, W. König and T. W. Hänsch, "A compact grating-stabilized diode laser system for atomic physics," *Optics Commun.*, **117** (1995) 541-549

[28] D. T. Cassidy and M. J. Hamp, "Diffractive optical element used in an external feedback configuration to tune the wavelength of uncoated Fabry-Perot diode lasers," *J. Mod. Opt.*, **46** (1999) 1071-1078

[29] J. P. Van der Ziel, R. Dingle, R. C. Miller, W. Wiegmann, and Jr. W. A. Nordland, "Laser oscillations from quantum states in very thin GaAs-$Al_{0.2}Ga_{0.8}As$ multilayer structures," *Appl. Phys. Lett.*, **26** (1975) 463-465

[30] R. W. H. Engelmann, C. Shieh, and C. Shu, "Multiquantum well lasers," in *Quantum Well Lasers*, edited by P.S. Zory Jr., San Diego: Academic Press, Inc. (1993) 180-182

[31] S. Ikeda, A. Shimizu and T. Hara, "Asymmetric dual quantum well laser --- wavelength switching controlled by current injection," *Appl. Phys. Lett.*, **55** (1989) 1155-1157

[32] V. K. Kononenko, I. S. Manak, S. V. Nalivko, V. Shevtsov, and D. Schulyaev, "Gain and luminescence spectra of broad emitters based on asymmetric quantumwell heterostructures," *J. Appl. Spectroscopy*, **64** (1997) 234-241

[33] H. S. Gingrich, D. R. Chummey, S. Z. Sun, S. D. Hersee, L. F. Lester, and S. R. J. Brueck, "Broadly tunable external cavity laser diodes with staggered thickness multiple quantum wells," *IEEE Photon. Technol. Lett.*, **9** (1997) 155-157

[34] S. C. Woodworth, D. T. Cassidy and M. J. Hamp, "Experimental Analysis of a Broadly Tunable InGaAsP Laser With Compositionally Varied Quantum Wells," *IEEE J. Quantum Electron*, **39** (2003) 426-430

[35] T. F. Krauss, G. Hondromitros, B. Vogele, and R. M. De La Rue, "Broad spectral bandwidth semiconductor lasers," *Electron. Lett.*, **33** (1997) 1142-1143

[36] C. Huang and C. Lin, "Dual-wavelength semiconductor laser with 191-nm mode spacing," in *Novel In-Plane Semiconductor Lasers III.* Edited by Gmachl, Claire F.; Bour, David P., *Proceedings of the SPIE*, **5365** (2004) 21-28

[37] C. Ellmers, A. Girndt, M. Hofmann, A. Knorr, W. W. Ruhle, F. Jahnke, S. W. Koch, C. Hanke, L. Korte, and C. Hoyler, "Measurement and calculation of gain spectra for (GaIn)As/(AlGa)As single quantum well lasers," *Appl. Phys. Lett.*, **72** (1998) 1647-1649

[38] B. W. Hakki and T. L. Paoli, "Gain spectra in GaAs double-Heterostructure injection lasers," *J. Appl. Phys.*, **46** (1975) 1299-1305

[39] D. T. Cassidy, "Technique for measurement of the gain spectra of semiconductor diode lasers," *J. Appl. Phys.*, **56** (1984) 3096-3099

[40] C. H. Henry, R. A. Logan and F. R. Merritt, "Measurement of gain and absorption spectra in AlGaAs buried heterostructure lasers," *J. Appl. Phys.*, **51** (1980) 3042-3050

[41] D. Hofstetter and J. Faist, "Measurement of semiconductor laser gain and dispersion curves utilizing Fourier transforms of the emission spectra," *IEEE Photon. Technol. Lett.*, **11** (1999) 1372-1374

[42] W. H. Guo, Q. Y. Lu, Y. X. Huang and L. J. Yu, "Fourier Series Expansion Method for Gain Measurement From Amplified Spontaneous Emission Spectra of Fabry-Pérot Semiconductor Lasers," *IEEE J. Quantum Electron.*, **40** (2004) 123-129

[43] W. H. Guo, Y. Z. Huang, C. L. Han, and L. J. Yu, "Measurement of gain for Fabry-Pérot semiconductor lasers by the fourier transform method with a deconvolution process," *IEEE J. Quantum Electron.*, **39** (2003) 716-721

[44] H. Wang and D. T. Cassidy, "Gain measurements of Fabry-Pérot semiconductor lasers using a nonlinear, least-squares fitting method," *IEEE J. Quantum Electron.*, **41** (2005) 532-540

[45] E. I. Gordon, "Optical Maser Oscillators and Noise," *Bell Syst. Tech. J.*, **43** (1964) 507-539

[46] P. R. Bevington and D. K. Robinson, *Data Reduction and Error Analysis Physical Sciences*, New York: McGraw-Hill (1992) 141-143

[47] A. Thelen, *Design of Optical Interference Coating*, McGraw-Hill (1989)

[48] S. Furman and A. V. Thikhonravov, *Basics of Optics of Multilayer Systems*, Editions Frontieres, Gif-sur-Yvette, France (1992)

[49] J. A. Dobrowolski, "Optical Properties of Films and Coatings", in *Handbook of Optics*, edited by M. Bass, McGraw-Hill (1995)

[50] H. A. MacLeod, *Thin-Film Optical Filters*, Institute of Physics Publishing (2001)

[51] A. V. Tikhonravov, M. K. Trubetskov, and G. W. DeBell, "Optical coating design approaches based on the needle optimization technique," *Applied Optics*, **46** (2007) 704-710

[52] A. V. Tikhonravov, "Synthesis of optical coatings using optimality conditions," Vestn. Mosk. Univ., Fiz, Astron. **23** (1982) 91-93

[53] A. V. Tikhonravov, M. K. Trubetskov, and G. DeBell, "Application of the needle optimization technique to the design of optical coatings," *Appl. Opt.*, **35** (1996) 5493-5508

[54] J.A. Nelder and R. Mead, "A Simplex Method for Function Minimization," *Computer J.*, **7** (1965) 308-313

[55] A. L. Bloom, "Refining and optimization in multilayers," *Appl. Opt.*, **20** (1981) 66-77

[56] P. Baumeister, "Design of Multilayer Filters by Successive Approximations," *J. Opt. Soc. Am.*, **48** (1958) 955-958

[57] W. J. Wild and H. Bukay, "Thin Film Multilayer Design Optimization Using a Monte Carlo Approach," *Opt. Lett.*, **11** (1986) 745-747

[58] J. R. Shewchuk, "*An Introduction to the Conjugate Gradient Method without the Agonizing Pain,*" Carnegie Mellon University, Pittsburgh (1994)

[59] J. A. Dobrowolski, "Comparison of the Fourier transform and flip-flop thin-film synthesis methods," *Appl. Opt.*, **33** (1986) 1966-1972

[60] A. V. Tikhonravov, M. K. Trubetskov, T. V. Amotchkina, and M. A. Kokarev, "Key role of the coating total optical thickness in solving design problems," *Proc. SPIE*, **5250** (2004) 312-321

[61] A. Tikhonravov, "Optimality of thin film optical coating design," *Proc. SPIE*, **1270** (1990) 28-35

[62] A. Tikhonravov, "Some theoretical aspects of thin-film optics and their applications," *Applied Optics*, **32** (1993) 5417-5426

[63] B. Broberg and S. Lindgren, "Refractive index of $In_{1-x}Ga_xAs_yP_{1-y}$ layers and InP in the trasparent wavelength region," *J. Appl. Phys.*, **55** (1984) 3376-3381

[64] S. L. Chuang, *Physics of Optoelectronic Devices*, John Wiley & Sons, Inc. (1995) 242-249

[65] W. Streifer, R. D. Burnham and D. R. Scifres, "Analysis of diode lasers with lateral spatial variations in thickness," *Appl. Phys. Lett.*, **37** (1980) 121-123

[66] J. Buus, "The effective index method and its application to semiconductor lasers," *IEEE J. Quantum Electron.*, **QE-18** (1982) 1083-1089

[67] D.R.Cote, S.V.Nguyen, A.K.Stamper, D.S.Armbrust, D.Tobben, R.A.Couti, and G.Y.Lee, "Plasma-assisted chemical vapor deposition of dielectric thin films for ULSI semiconductor circuits," *IBM J. Res. Develop.*, **43**, 1/2 (1999) 5-38

[68] A Dollet, J P Couderc and B Despax, "Analysis and numerical modelling of silicon nitride deposition in a plasma-enhanced chemical vapour deposition reactor. I. Bidimensional modeling," *Plasma Sources Sci. Technol.*, **4** (1995) 94-106

[69] G. Lucovsky, P. D. Richard, D. V. Tsu, S. Y. Lin, and R. J. Markunas, "Deposition of silicon dioxide and silicon nitride by remote plasma enhanced chemical vapor deposition," *J. Vac. Sci. Technol.*, **A 4** (1986) 681-688

[70] G. Turban, "Basic Phenomena in Reactive Low Pressure Plasmas Used for Deposition and Etching," *Pure & Appl. Chem.*, **56** (1984) 215-230

[71] P. A. Longeway, R. D. Estes, and H. A. Weakliem, "Decomposition Kinetics of a Static Direct Current Silane Glow Discharge," *J. Phys. Chem.*, **88** (1984) 73-77

[72] M. J. Kushner, "Plasma chemistry of $He/O_2/SiH_4$ and $He/N_2O/SiH_4$ mixtures for remote plasma-activated chemical-vapor deposition of silicon dioxide," *J. Appl. Phys.*, **74** (1993) 6538-6553

[73] K. H. Chew, J. Chen, R. C. Woods and J. L. Shohet, "Silicon oxide deposition in an electron cyclotron resonance plasma with microwave spectroscopic monitoring of SiO," *J. Vac. Sci. Technol.*, **A 13** (1995) 2483-2489

[74] S.M. Han and E.S. Aydil, "Study of surface reactions during plasma enhanced chemical vapor deposition of SiO_2 from SiH_4, O_2, and Ar plasma," *J. Vac. Sci. Technol.*, **A 14** (1996) 2062-2070

[75] H. G. Tompkins and W. A. McGahan, "*Spectroscopic ellipsometry and reflectometry,*", John Wiley & Sons, Inc., Toronto (1999)

[76] H. Zhang, "*Study of optimal deposition conditions for an inductively coupled plasma chemical vapour deposition (ICP-CVD) system,*" Thesis (M.A.Sc.), McMaster University (2005)

[77] "*Guide to using WVASE32®,*" J. A. Woollam Co., Inc. (2001) 7-15

[78] B. R. Bennett, R. A. Soref, and J. A. Del Alamo, "Carrier-induced change in refractive index of InP, GaAs and InGaAsP," *IEEE J. Quantum Electron.*, **26** (1990) 113-122

[79] D. Botteldooren and R. Baets, "Influence of band-gap shrinkage on the carrier-induced refractive index change in InGaAsP," *Appl. Phys. Lett.*, **54**, 1989 (1989) 1989-1991

[80] D. Huang, E. Swanson, C. P. Lin, J. S. Schuman, W. G. Stinson, W. Chang, M. R. Hec, T. Hotte, K. Gregory, C. A. Puliafito, and J. G. Fujimoto, "Optical coherence tomography," *Science*, **254** (1991) 1178-1181

[81] F. Lexer, C. K. Hitgenberger, A. F. Fercher and M. Kulhavy, "Wavelength-tuning interferometry of intraocular distances," *Appl. Opt.*, **36** (1997) 6548-6553

[82] H. Hiratsuka, E. Kido, and T. Yoshimura, "Simultaneous measurements of three-dimensional reflectivity distributions in scattering media based on optical frequency-domain reflectometry," *Opt. Lett.*, **23** (1998) 1420-1422

[83] A. GH. Podoleanue, G. H. Dobre, D. J. Webb and D. A. Jackson, "Simultaneous en-face imaging of two layers in the human retina by low-coherence reflectometry," *Opt. Lett.*, **22** (1997) 1039-1041

[84] E. Beaurepaire, A. C. Boccara, M. Lebec, L. Blanchot and H. S. Jalmec, "Full-field optical coherence microscopy," *Opt. Lett.*, **23** (1998) 244-246

[85] W. Drexler, U. Morgner, F. X. Kartner, C. Pitris, S. A. Boppert, X. D. Li, E. P. Ippen and J. G. Fujimoto, "*In vivo* ultrahigh-resolution optical coherence tomography," *Opt. Lett.*, **24** (1999) 1221-1223

[86] J. Rao, Y. N. Ning and D. A. Jacson, "Synthesized source for white-light sensing systems," *Opt. Lett.*, **18** (1993) 462-464

[87] K. Hotate, and O. Kamatani, "Optical coherence domain reflectometry by synthesis of coherence function," *J. Lightwave Technol.*, **11** (1993) 1701-1710

[88] M. A. A. Neil, R. Juskaitis, T. Wilson, and Z. J. Laczik, "Optimized pupil-plane filters for confocal microscope point-spread function engineering," *Opt. Lett.*, **25** (2000) 245-247

[89] B. E. Bouma and G. J. Tearney, *Handbook of Optical Coherence Tomography*, Marcel Dekker, Inc. (2002) 361

[90] J. W. Goodman, *Statistical optics*, John Wiley & Sons, Inc. (1985)

[91] R. J. Bell, *Introductory Fourier Transform Spectroscopy*, Academic Press, Inc. (1972) 38